LA-12722-T
Thesis

Instability Heating of Solid-Fiber Z Pinches

Los Alamos
NATIONAL LABORATORY

Los Alamos National Laboratory is operated by the University of California for the United States Department of Energy under contract W-7405-ENG-36.

DISTRIBUTION OF THIS DOCUMENT IS UNLIMITED

This thesis was accepted by the Department of Physics, University of California – San Diego, La Jolla, California, in partial fulfillment of the requirements for the degree of Doctor of Philosphy. The text and illustrations are the independent work of the author and only the front matter has been edited by the IS-1 staff to conform with Department of Energy and Los Alamos National Laboratory publication policies.

This work was supported by the US Department of Energy, Office of Energy Research.

An Affirmative Action/Equal Opportunity Employer

This report was prepared as an account of work sponsored by an agency of the United States Government. Neither The Regents of the University of California, the United States Government nor any agency thereof, nor any of their employees, makes any warranty, express or implied, or assumes any legal liability or responsibility for the accuracy, completeness, or usefulness of any information, apparatus, product, or process disclosed, or represents that its use would not infringe privately owned rights. Reference herein to any specific commercial product, process, or service by trade name, trademark, manufacturer, or otherwise, does not necessarily constitute or imply its endorsement, recommendation, or favoring by The Regents of the University of California, the United States Government, or any agency thereof. The views and opinions of authors expressed herein do not necessarily state or reflect those of The Regents of the University of California, the United States Government, or any agency thereof.

LA-12722-T
Thesis

UC-426
Issued: February 1994

Instability Heating of Solid-Fiber Z Pinches

Ronald Alan Riley, Jr.*

*Graduate Research Assistant at Los Alamos Group P-1.

DISTRIBUTION OF THIS DOCUMENT IS UNLIMITED

Los Alamos
NATIONAL LABORATORY
Los Alamos, New Mexico 87545

MASTER

Acknowledgments

This research was performed on the High Density Z-Pinch II facility at Los Alamos National Laboratory and was supported by the U.S. Department of Energy. I would like to thank the late Dr. Jay Hammel, who created the HDZP-II facility, Dr. Harry Dreicer, Dr. Larry Jones, and all of the others who managed to keep the project funded long enough to complete this research. I would like to thank Dr. Jack Shlachter, my local advisor and committee member, and Dr. David Scudder for building and running the experiment. I would like to thank Dalio J. Rodriguez, Otoniel "Freddy" Garcia, and Terry D. Langham for keeping the machine running and for all of their help building new diagnostics.

I would like to thank by advisor, Dr. Ralph H. Lovberg, for accepting me as a graduate research assistant on the experiment at Los Alamos National Laboratory. He proposed the turbulent heating mechanism that this research is based on and wrote the initial code of the 0-D simulation. He also did much of the designing of the optical and x-ray diagnostics. He has been very generous with his time and very patient.

I would like to thank Dr. Robert Chrien for fielding and calibrating the neutron diagnostics. I would like to thank Dr. Peter R. Forman and his student, Jaime Hernandez-Cortez, for their work on the multiframe circular-schlieren diagnostic.

I would like to thank Dr. David Scudder, Dr. Jack Shlachter, and Dr. Larry Jones for taking out at least an hour each week during the writing of this document for extended discussions of its content.

I would like to thank Nancy Riley for aiding me in fulfilling lab safety requirements, for assisting with repairs, and for editing this document.

Table of Contents

List of Symbols

a	The radius of the rigid return conductor in m.
a_0	The Bohr radius = $\epsilon_0 h^2/\pi m_e e^2 \approx 5.29\times10^{-11}$ m.
a_{Max}	The inter-atomic spacing $\equiv (\Sigma n_i)^{-1/3}$ (m).
A	The area in m^2.
A_i	The atomic mass number of an isotope.
A_{Br}	Bremsstrahlung attenuation. coeff. $\equiv C_{Br} h^2 c^2 e^{-7/2} \approx 5\times10^{-47} eV^{7/2}\bullet m^5$.
$\vec{B}$, B_θ	The magnetic field in teslas.
B_{rm}	The bremsstrahlung power coefficient $\approx 1.5\times10^{-38}$ $W\bullet m^3/eV^{1/2}$.
c	The speed of light in vacuum $\approx 2.9979\times10^8$ m/s.
c_p, c_v	The specific heats at constant pressure, and at constant volume.
C_{Br}	The bremsstrahlung emissivity coefficient $\approx 4\times10^{-63}$ $J^{3/2}\bullet m^3$.
C_{line}	The line-radiation power coefficient $\approx 3.49\times10^{-31}$ $W\bullet m^3\bullet eV^{1/2}$.
CD_2	Deuterated polyethylene.
d	The diameter in m.
$2d$	The crystal plane spacing, = 26.6 Å for KAP crystals.
D, D_2	The hydrogen isotope deuterium with $A_i = 2$.
e	The electronic charge $\approx 1.6022\times10^{-19}$ C.
δE_i	The continuum-lowering reduction of the ith ionization potential.
ΔE	The difference in energy in eV.
E_z	The applied electric field in V/m.
E_ω	The photon energy = $\hbar\omega/e$ (eV).
ΔE_ω	The photon energy bandwidth = $\hbar\Delta\omega/e$ (eV).
f	The integer number of degrees of freedom.
$g_{i,k}$	The statistical weight of ionization state i at excitation state k.
g_{Br}	The bremsstrahlung Gaunt factor $\approx$ 1.4.
$\hbar$, h	Planck's constant $\hbar = h/2\pi \approx 1.0546\times10^{-34}$ J•s.

HDZP-II	The High Density Z-Pinch II facility.
i	The mathematical constant $\sqrt{-1}$.
i,j,k	The quantum number of a bound state.
I	The pinch current in A and radiant intensity in W•s/m^2•sr.
I_0, I_1	Modified Bessel functions of the first kind of order 0 and 1.
I_{BB}	Blackbody intensity $=e^3E_\omega{}^3/\{2\pi h^2c^2[exp(E_\omega/T_e)-1]\}$ (W•s/m^2•sr).
I_p	The peak current in amperes.
I_{PB}	The Pease-Braginskii current $\approx 2.2\times10^5\ \sqrt{\ln\Lambda}\ (1+Z)/Z$ (A) .
IR	Infrared.
j	The radiant volumetric emissivity in W•s/m^3•sr.
$jaxis_i$	The column position of the plasma axis.
jl_i, jr_i	The column positions of the left and right edges.
$\vec{J}$	The current density vector in A•m^{-2}.
K_{ab}	The calibration ratio of detectors a/b at 1 keV, ~0.5.
KAP	Potassium acid-phthalate organic crystal.
ℓ	The length of the pinch = 0.05 m.
L	The inductance in henrys.
LTE	Local Thermodynamic Equilibrium.
$ln\Lambda$	The Coulomb logarithm.
$m=0,1,...$	The integer label of an instability mode.
m_e, m_d, m_c	The mass of an electron, a deuteron, and a carbon ion in kg.
M	The mass of the entire pinch plasma in kg.
MHD	Magnetohydrodynamic.
n_0	Ion density for solid, $n_d = 5\times10^{28}$ m^{-3}, $n_{CD2} = 3.8\times10^{28}$ m^{-3}.
n_{crit}	The cutoff electron density $= 4\times10^{27}$ m^{-3} for $\lambda=532$ nm.
n_e, n_i, n_p	The particle density of electrons, ions, total particles in m^{-3}.
N_e, N_i, N_p	The particle line-density of electrons, ions, total $\equiv\int dx\ \int dy\ n$ (m^{-1}).
$NRow$	The number of rows in the image.

p	The plasma kinetic pressure in Pa.
P_{BB}	The blackbody radiative cooling power = $A\ \sigma_{SB}\ T_e^4$ (W).
P_{Cy}	The cyclotron radiative cooling power $\approx 5\times10^{-44}\, dV\sqrt{T_e}\, n_e^2$ (W).
P_{Brem}	The bremsstrahlung cooling power $\approx dV g_{Br} B_{rm} \sqrt{T_e}\, n_e \Sigma Z_i^2\, n_i$ (W).
$P_{i,k}$	The free-bound cooling power $\approx 4.2\times10^{-37}\, dV\, T_e^{-1/2}\, n_e\, n_i\, Z_i^4 / k^3$ (W).
P_{Ionz}	The cooling power required to increase ionization, in watts.
P_{Joule}	The Joule resistive heating power in watts.
P_{Rad}	The total radiative cooling power in watts.
P_{Turb}	The turbulent heating power in watts.
PIN	P-layer/Intrinsic-layer/N-layer photodiode.
r	The cylindrical radius of the plasma in m.
r_0	The solid-fiber radius in meters.
r_1	The initial plasma radius input to the simulation.
r_e	The classical electron radius $\equiv e^2 / 4\pi\epsilon_0 m_e c^2 \approx 2.82\times10^{-15}$ m.
R_{12}	The ratio of PIN detector signals = W_1/W_2.
R_m	The magnetic Reynolds number = $\mu_0 r v_A / \eta$.
R_{mp}	The integrated crystal reflectivity in radians.
R_{Turb}	The effective resistance due to turbulence in Ω.
R_y	The Rydberg constant $\equiv e^4\, m_e / 8\ \epsilon_0^2\, h^2 \approx 13.6$ eV.
Res	The height,width of an image pixel in meters.
s	The path length in m.
S	The PIN diode detector sensitivity ~0.276 A/W.
t	The time in s, primarily relative to the start of the main current.
t_1	The starting time of the simulation in seconds.
T	The hydrogen isotope tritium with A_i=3.
T, T_e, T_d, T_c	The temperatures of the plasma, electrons, and ions in eV.
T_{ab}	The T_{ab} computed from the ratio of detectors a/b in eV.
T_{PB}	The plasma temperature at the Pease-Braginskii current in eV.

T_r	The transmission of the x-ray filters for a given photon energy.
U_e, U_d, U_c	The energy densities of the electrons, ions in eV/m^3.
v_1	The initial radial velocity input to the simulation in m/s.
v_A	The Alfvén velocity = $B_\theta / \sqrt{\mu_0 \rho} = \sqrt{\mu_0 / \rho}\ I/2\pi r$ (m/s) .
v_r	The radial velocity in m/s.
v_T	The thermal velocity = $\sqrt{eT/m}$ (m/s) .
V	The volume in m^3.
$w(T_e)$	The PIN signal factor independent of photon energy in V/eV.
W	The PIN diode detector signal in volts.
z_i	The partition function for excitation level i.
Z, Z_i	The charge of an ion in units of e.
Z_A	The atomic number equaling the charge of the nucleus.
Z_C	The average carbon ionization = $\Sigma Z_i n_i$ / Σn_i.
$\overline{Z \ln\Lambda}$	The density weighted average = $\Sigma Z_i^2 ln\Lambda_i n_i$ / n_e.
α	The absorption coefficient = j / I_{BB} (m^{-1}).
β	The thermal / magnetic energy ratio.
γ	The adiabatic expansion coefficient = c_p/c_v = (f+2)/f ≈ 5/3.
δ	The current skin depth of the current in m.
$\nabla_\perp x$	The differential operator ≡ $\lvert\hat{s}\times(\vec{\nabla}x)\rvert$.
∇_l, ∇_r	The strength of the gradients at the left and right edges.
$\delta\theta$	The full-width half-max of the integrated reflectivity in radians.
ϵ_0	The permittivity of free space ≈ 8.8542× 10^{-12} F/m.
ϵ_{Si}	The dielectric constant for silicon 11.7.
η, η_{Spitz}	The plasma resistivity, for Spitzer ≈ $10^{-4}\,\overline{Z\ln\Lambda}\,T_e^{-3/2}$ (Ωm).
κ	The spatial frequency ≡ $2\pi/\lambda$ (m^{-1}).
λ	The diagnostic laser wavelength = 532 nm.

λ_D	The Debye length = $\sqrt{\epsilon_0 T_e / n_e e}$ (m) .
μ_0	The permeability of free space = $4\pi \times 10^{-7}$ H/m.
μ_r	The plasma refractive index $\approx 1 - 2\pi r_e c^2 n_e / \omega^2$.
ξ	The complex perturbation of radius in m.
ρ	The plasma mass density in kg/m^3.
σ	The collision cross section in m^2.
σ_{SB}	The Stefan-Boltzmann constant $\equiv \pi^2 e^4 / 60 \hbar^3 c^2 \approx 10^9$ W•m^{-2}•eV^{-4}.
τ	The optical thickness $\equiv \int \alpha \, ds$.
$\tau_{cd}, \tau_{ce}, \tau_{de}$	The inter-particle-species thermal-equilibration times in s.
τ_{HH}	The Haines-Hammel curve time scale in s.
τ_L	The Lawson time for fusion energy breakeven in s.
$\tau_{m=0}$	The $m=0$ instability "e folding" growth time in s.
ϕ	The phase advance due to traveling through plasma $\approx \lambda r_e \int dx \, n_e$.
$\psi_{cd}, \psi_{ce}, \psi_{de}$	The inter particle species thermal equilibration coeffs. in m^{-3}s^{-1}.
ω	The angular frequency in rad/s.
$\Delta\omega_{D\,1/2}$	The doppler line-width = $\sqrt{2\,ln2}\, v_T / c$ (rad/s).
$\Delta\omega_{S\,1/2}$	The Stark line-width in rad/s.
ω_p	The plasma frequency $\equiv e\sqrt{n_e/\epsilon_0 m_e} \approx 56.4\sqrt{n_e}$ (rad/s).
Ω_c	The ion cyclotron frequency in = eB/m_i (rad/s).

List of Figures

List of Tables

INSTABILITY HEATING OF SOLID-FIBER Z PINCHES

by

Ronald Alan Riley, Jr.

ABSTRACT

The Los Alamos High Density Z Pinch-II (HDZP-II) facility is used to study the dynamics of z-pinch plasmas generated from solid fibers of deuterated polyethylene CD_2 with a range in radii of 3-60 μm. HDZP-II is a pulsed-power generator that delivers a current that rises to 700 kA in 100 ns through an inductive load. A multiframe circular schlieren records the evolution of the shape and size of the plasma on seven images taken at 10-ns intervals. These circular-schlieren images show very strong *m=0* instability at the onset of current and a rapid radial expansion of the plasma. No higher-order instabilities are observed. An interferometer is used to infer the electron density and electron line density, giving a measure of the fraction of plasma contained within the outline of the circular-schlieren image at one time during the multiframe sequence. A three-channel x-ray crystal-reflection spectrometer provides the time-resolved, spatially-averaged electron temperature. The magnitude of the x-ray emission at these energies also gives qualitative information about the electron temperature and density at late times. A lower bound on the ion temperature is inferred from the particle pressure needed to balance the magnetic field pressure. The ion temperature rose above that of the electrons, strongly suggesting an additional heating term that puts energy directly into the ions. An ion heating term is proposed to explain the observed rapid radial expansion and elevated ion temperatures. This heating term is based on the assumption that the observed *m=0* instabilities reconnect, enclosing magnetic flux which degenerates into turbulence in the plasma. A 0-D simulation is developed to investigate the relevance of different physical models to the data presented.

I INTRODUCTION

This chapter presents a brief history of z-pinch fusion research and discusses basic z-pinch physics including stability theory. All equations are expressed in mks units, except energies and temperatures, which are in eV.

1.1. Z-Pinch Concept

The primary goal of fusion research is to provide a useful power source. To achieve this goal, a plasma must be heated to high temperatures (≥ 10 keV) and must maintain a high density long enough for fusion to take place, in an economical fashion. The Lawson criterion[1] for deuterium-tritium (D-T) plasmas,

$$\tau_L \geq 10^{20} / n_i \quad (s) \quad , \tag{1.1}$$

gives the constraint on the energy confinement time τ_L in terms of the ion density n_i in m^{-3} required for fusion break-even, by balancing the fusion output energy with heating less the radiative losses. For example, a solid density ($n \approx 5 \times 10^{28}$ m^{-3}) D-T plasma must be confined for $\tau_L \approx 2$ ns for this definition of break-even.

To achieve high temperatures, the plasma must be thermally isolated from its surroundings. Magnetic confinement is a common way of attempting to do this.

The z-pinch geometry, as shown in Fig. 1.1, is the simplest for magnetic confinement of a plasma, requiring no external field coils. A z pinch consists of a column of plasma with a large current flowing along its longitudinal axis. This current generates a magnetic field that confines the plasma by the "pinch effect."

The pinch effect was the first concept used to magnetically confine a conducting fluid. A pinch is compressed by the Lorentz force ($\vec{J} \times \vec{B}$) of the magnetic field acting on the charge carriers of the current that generates it. The same forces that compress a z pinch will also drive magnetohydrodynamic (MHD)

instabilities, as discussed in Section 1.4, which will cause the column to expand. The inductance[2] of a z pinch of length ℓ and radius r with rigid return-conductor radius a,

$$L = \frac{\ell \mu_0}{2\pi} \ln\frac{a}{r} \ (H) \ , \qquad (1.2)$$

increases as its radius decreases.

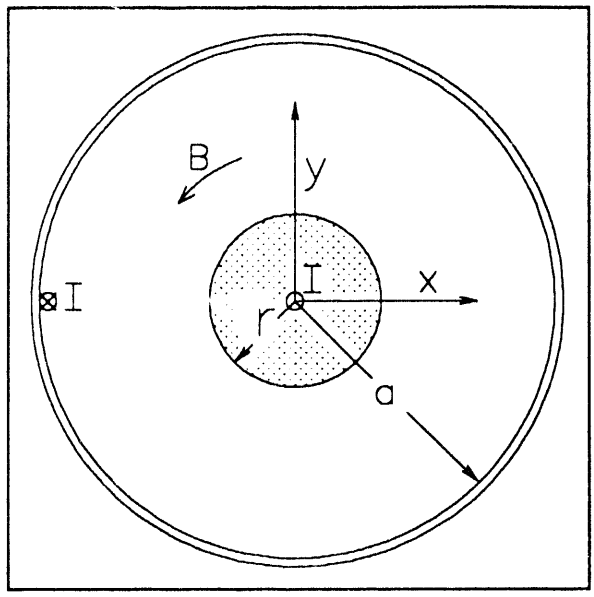

Fig. 1.1 Z-pinch geometry.
A plasma column of radius r within a return conductor of radius a and with current I.

Bennett[3] first described this pinch effect as "self focusing streams" in his definitive paper in 1934. When the radial velocity of a z pinch is much less than the ion sound speed, its thermal and magnetic pressures are considered in balance, approximately satisfying the Bennett relation:

$$N_e e T_e + \sum N_i e T_i = \frac{1}{2\mu_0} \int dx \int dy \, B_\theta^2 = \frac{\mu_0 I^2}{8\pi} \ (J/m) \ , \qquad (1.3)$$

where N_e and N_i are the electron and ion line densities ($N \equiv \int dx \int dy \, n$) in m^{-1}, T_e and T_i are the electron and ion temperatures in eV, and the magnetic field produced by a wire carrying current I in A is[4]

$$B_\theta = \frac{\mu_0 I}{2\pi r} \ (T) \ . \qquad (1.4)$$

The magnetic field energy density outside the z pinch falls off as r^{-2}, which makes efficient use of this energy by concentrating it at the surface of the plasma.

1.2. Z-Pinch History

Shortly after 1950, several groups began working on pinch experiments for magnetically confined fusion. Beyond the advantages given above, the first pinch experiments were easy to construct and operate. The simplicity of these pinch apparatuses provided many scientists with an early familiarization with plasma physics and an excellent testbed for developing plasma diagnostics.

1.2.1. Shock-Heated Pinch

The early z-pinch experiments used cylinders of low density gas for the plasma source material. What has been described so far is a pinch in equilibrium; however, laboratory pinches are generally dynamic. Early pinches were generally created in the laboratory by applying a large voltage, usually from a capacitive or inductive energy store, to electrodes at the ends of an insulated cylinder filled with hydrogen isotopes. The gas breaks down at the wall of the insulating cylinder enclosing the gas; the current rapidly rises, compressing the plasma into a thin channel at the pinch axis.

The plasma is heated by the shock of the radial collapse and by electrical resistance. If the pinch current rises fast enough, the current flows primarily on the surface of the plasma in a thin current sheath. This sheath sweeps the plasma in like a fast piston during the pinch's collapse. The ions acquire the radial velocity of this sheath until the converging plasma stagnates on the axis. Under this "snowplow" model, the resulting ion thermal speed approximates the radial speed of the collapse. When the collapse stagnates, the hot ions begin to thermalize with the cool electrons, halving the ion temperature (for a hydrogen plasma). Sheath trajectories have been observed in several experiments. Shock heating gives all charged particles in the plasma a change in velocity, which

directly heats the ions. The ions receive much more kinetic energy than the electrons, because of their larger masses.

The voltage required to produce a deuterium plasma with a temperature of ~ 10 keV can be estimated as follows[5]. The magnetic pressure at the surface of the pinch must supply the momentum delivered to the gas of density ρ (in kg/m^3) swept up by the snowplow. The surface sweeps up the mass of the plasma at the rate of $2\pi r \ell \rho v_r$ (kg/s). This requires the magnetic field to supply a kinetic energy per unit volume of

$$\rho\, v_r^2 = B_\theta^2 / (2\,\mu_0) \quad (Pa) \ . \tag{1.5}$$

Treating the plasma as a perfect conductor, having no electric field parallel to its surface in its rest-frame, in the lab-frame

$$E_z = v_r B_\theta = v_r^2 \sqrt{2\,\mu_0\,\rho} \quad (V/m) \ , \tag{1.6}$$

where Eq. (1.5) was used to substitute for the magnetic field. Deuterons at temperatures of ~ 10 keV will require a speed of ~ 10^6 m/s. A density greater than 10^{-6} kg/m^3 is required for experimentally reproducible results. These conditions require the applied voltage greater than 1.6 MV/m.

During the 1950s, the best attempts at high-voltage pinches[6,7] were only able to achieve a little over 10^5 V/m and in both experiments the insulating tube wall seems to have "flashed over." ("Flashing over" refers to a surface becoming ionized by a high voltage allowing current to arc along tracks.) This reduced the current flowing in the deuterium column and contaminated it with higher-Z_A elements from the wall, increasing the radiative cooling. Such results discouraged further research in shock-heated fusion experiments. A later experiment[8] succeeded in operating at greater than 10^5 V/m without wall breakdown, reaching temperatures just below 1 keV. This experiment used an inductive energy store

that allowed quick removal of the voltage after the pinch collapsed to avoid flashing over the insulator after the collapse.

Anderson *et al.*[9] used a z pinch formed in a cylinder of deuterium (D_2) gas to study thermonuclear reaction rates and neutron production. The plasma sheath was observed to collapse toward the axis, then expand and neck off into $m=0$ "sausage" instabilities, which are described in Section 1.4. The neutrons were not emitted isotropically, leading to the conclusion that they were produced by the instabilities rather than by thermal collisions.

1.2.2. Resistively Heated Pinch

The resistance of the plasma to the pinch current provides another way of heating the plasma. This resistance is due to the electrons carrying the current being slowed by collisions with ions. The heated electrons then warm the ions. Unfortunately, as discussed in Section 1.3, the resistance of the plasma is proportional to $T^{-3/2}$ and so will become a less effective heating mechanism at higher temperatures and currents. The simple pinch is also MHD unstable, as discussed in Section 1.4. These problems make it very difficult to resistively heat a plasma to high temperatures long enough for fusion to take place.

Shortly after MHD instabilities were observed experimentally[10], many researchers independently suggested including an axial magnetic field as a remedy. Experimentally, this stabilizing field is created by an external coil driven by a slow capacitor bank, which is started before the pinch current. When the pinch current forms a conducting sheath of plasma at the outer radius of the gas, it traps the externally-imposed, axial magnetic field inside.

Experiments have suppressed $m=0$ "sausage" instabilities with a very small axial field[11]. A larger stabilizing field eliminated gross $m=1$ "kink" instabilities, but "fluttering" in the magnetic field at the surface persisted[12]. ("Fluttering" refers

to fast oscillations in the local magnetic field strength.) Magnetic-probe mapping data for this experiment showed that although the overall pinch met the stability requirements, the Suydam criterion for stability was violated at the surface of the plasma, resulting in local instability.

1.2.3. Gas-Embedded Z Pinch

Alfvén *et al.*[13] suggested that the contamination of the plasma by impurities from the wall could be avoided by initiating a narrow column inside a larger volume of neutral gas. He suggested that for strong magnetic fields, the radial thermal conduction might be lower than for a current-sheath pinch. Further, kink instabilities would be suppressed by inertially coupling the pinch with a surrounding ionized corona.

Experiments by Smars[14] on a spark channel in hydrogen between plane electrodes in which the current rose to 100 kA in one micro-second showed a channel that expanded monotonically, reached a temperature of 14 eV, and developed kink modes. Several other experiments created the initial channel with intense laser beams or electron beams. These experiments achieved current rise rates of less than 10^{12} A/s and produced expanding channels with temperatures of less than 100 eV.

Shlachter[15] found that the column expansion was driven by an accretion of the neutral gas surrounding the pinch, which increased the pinch line density and cooled the plasma. Haines and Hammel suggested that a much larger current rise rate could overcome this expansion, as discussed in detail in Section 1.3.

1.3. Z-Pinch Scaling

Pease[16] and Braginskii[17] independently identified the unique current for a pure-hydrogen-plasma z pinch in Bennett equilibrium and in power balance. This power balance is between bremsstrahlung radiative cooling and joule heating.

For the remainder of this chapter it will be assumed that the ions and electrons have a common temperature $T = T_i = T_e$, that the densities of the electrons and of the various ion species are uniform within the volume of the pinch plasma, and so

$$N \equiv \int dx \int dy\, n = \pi r^2 n \quad (m^{-1}) \quad , \tag{1.7}$$

and that the radius and line densities (N) are constant along the length of the column. Solving the Bennett relation, Eq. (1.3), for the common temperature in terms of the current and the line densities

$$eT = 5\times10^{-8} I^2 / N_p \quad (J) \quad , \tag{1.8}$$

where

$$N_p \equiv N_e + \Sigma N_i \quad (m^{-1}) \tag{1.9}$$

is the total charged-particle line density.

The bremsstrahlung radiative power, discussed in Section 2.2.1, emitted by an optically thin cylinder of plasma of volume $\pi r^2 \ell$ is[18],

$$P_{Brem} = \ell\, g_{Br} B_{rm} \sqrt{T_e}\, N_e \sum Z_i^2\, n_i \quad (W) \quad , \tag{1.10}$$

where $B_{rm} \approx 1.5 \times 10^{-38}$ W•m^3/eV$^{1/2}$ is the bremsstrahlung coefficient, $g_{Br} \approx 1.4$ is the bremsstrahlung Gaunt factor, and the summation is over the ionization states of all ions in the plasma.

The joule heating power is

$$P_{Joule} = I^2 \frac{\ell}{\pi r^2} \eta \approx I^2 \frac{\ell}{\pi r^2}\, 10^{-4}\, \overline{Z \ln\Lambda}\, T_e^{-3/2} \quad (W) \quad , \tag{1.11}$$

assuming Spitzer resistivity for a magnetized plasma[19,20],

$$\eta_{Spitz} \approx \frac{\overline{Z\ln\Lambda}}{6\,\varepsilon_0^2}\sqrt{\frac{e\,m_e}{2\pi^3 T_e^3}} \approx 1.03\times10^{-4}\,\overline{Z\ln\Lambda}\,T_e^{-3/2} \quad (\Omega\bullet m)\,, \tag{1.12}$$

where

$$\overline{Z\ln\Lambda} \equiv \sum Z_i^2 \ln\Lambda_i\, n_i / n_e \tag{1.13}$$

and the Coulomb logarithm is defined as[21],

$$\ln\Lambda_i = \begin{cases} \ln\left[\dfrac{\sqrt{\dfrac{\epsilon_o T_e}{e\,n_e}}}{\dfrac{Z_i\,e}{4\pi\epsilon_o T_e}}\right] \approx 29.3 + \dfrac{1}{2}\ln\left[\dfrac{T_e^3}{n_e Z_i^2}\right] & for \quad T_e \le 27.2\,Z_i^2 \\ \dfrac{1}{2}\ln\left[\dfrac{\epsilon_o T_e^2 m_e}{n_e\,\hbar^2}\right] \approx 30.9 + \dfrac{1}{2}\ln\left[\dfrac{T_e^2}{n_e}\right] & for \quad T_e \ge 27.2\,Z_i^2 \end{cases} \tag{1.14}$$

The Coulomb logarithm typically ranges from 1 to 10 for plasmas created in the Los Alamos High-Density Z-Pinch II (HDZP-II) facility.

See Appendix A for a derivation of Spitzer resistivity for multiple ion species. Spitzer resistivity is valid if $ln\Lambda_i > 1$. The resistivity given in Eq. (1.12) assumes that the plasma is strongly magnetized. This assumption is justified if the electron cyclotron frequency is larger than the collision frequency

$$\frac{I\,r\,T_e^{3/2}}{N_e\,\overline{Z\ln\Lambda}} > \frac{2}{3\,\mu_0\varepsilon_0^2}\sqrt{\frac{m_e\,e^3}{2\,\pi}} \approx 1.6\times10^{-16}\,, \tag{1.15}$$

This condition is always met for experiments on HDZP-II. When this condition is not met, the resistivity is reduced by roughly a factor of 2 for $Z_A = 1$.

Equating the heating and cooling powers, and using Eq. (1.8) to substitute for the temperature, the Pease-Braginskii current is

$$I_{PB} = 2.2\times10^{5}\sqrt{\frac{\overline{Z\ln\Lambda}}{N_e\sum Z_i^2 N_i}}\,N_p \quad (A) \quad . \tag{1.16}$$

Again, the summation is over the ionization states of all ions in the plasma. The Pease-Braginskii current is only weakly dependent on the electron temperature and density through the Coulomb logarithm. The corresponding temperature from the Bennett relation is

$$T_{PB} = 1.5\times10^{22}\,\frac{N_p\,\overline{Z\ln\Lambda}}{N_e\sum Z_i^2 N_i} \approx 1.5\times10^{22}\,\frac{1+Z_A}{Z_A^2 N_e}\ln\Lambda \quad (eV) \; . \tag{1.17}$$

For a fully ionized plasma with only one ion species, $Z_A\Sigma n_i = \Sigma Z_i n_i = n_e$, the Pease-Braginskii current simplifies to

$$I_{PB} = 2.2\times10^{5}\,\sqrt{\ln\Lambda}\;(1+Z_A)/Z_A \quad (A) \; . \tag{1.18}$$

For a pure-hydrogen plasma ($Z_A = 1$), this current is a little over one megampere, and for a temperature of 10 keV, the line density required by this current is

$$N_e \approx \frac{Z_A}{Z_A+1}N_P \approx 1.5\times10^{21}\,\frac{\ln\Lambda}{T}\,\frac{Z_A+1}{Z_A} \approx 3.1\times10^{19} \quad m^{-1} \tag{1.19}$$

corresponding to a solid hydrogen fiber ($n = 5\times10^{28}$ m^{-3}) of radius 14 μm.

Haines[22] and Hammel[23] independently derived the current as a function of time required to heat a pure-hydrogen z-pinch plasma to these asymptotic values while maintaining Bennett equilibrium (i.e. constant radius). They assumed quasi-neutrality for a pure-hydrogen plasma ($n = n_i = n_e = n_p/2$). From an initial zero-temperature plasma, the excess of the joule heating over the bremsstrahlung loss raises the temperature as

$$3\,N\,e\,\frac{dT}{dt} = \frac{10^{-4}\,I^2\ln\Lambda}{\pi r^2\,T^{3/2}} - \frac{g_{Br}\,B_{rm}\,N^2\sqrt{T}}{\pi r^2} \quad (W/m) \quad . \tag{1.20}$$

Again using the Bennett temperature, Eq. (1.8),

$$\frac{dI}{dt} = 10^4\, n \sqrt{\frac{N}{90e}} \left[1.6\times 10^{11}\, \frac{e^2}{I^2}\, \ln\Lambda - g_{Br} B_{rm} \right] \equiv \left[\frac{I_{PB}^2}{I^2} - 1 \right] \frac{I_{PB}}{\tau_{HH}} \quad , \tag{1.21}$$

where

$$\tau_{HH} \equiv \frac{120}{n} \sqrt{\frac{10\,\ln\Lambda}{N} \left(\frac{e}{g_{Br}\, B_{rm}} \right)^3} \approx \frac{2.4\times 10^{31}}{n\,\sqrt{N}} \quad (s) \tag{1.22}$$

is the Haines-Hammel time-scale. The solution of this equation,

$$\frac{t}{\tau_{HH}} = \frac{1}{2} \ln\left(\frac{I_{PB}+I}{I_{PB}-I} \right) - \frac{I}{I_{PB}} \approx \frac{I^3}{3I_{PB}^3} + \cdots \quad for \quad I<I_{PB} \quad , \tag{1.23}$$

is called the Haines-Hammel curve. The current then varies at early times as $I \approx I_{PB}(3t/\tau_{HH})^{1/3}$, requiring an infinite initial rise-rate

$$\lim_{t\to 0} \dot{I} \approx I_{PB} (9\,\tau_{HH})^{-1/3} \lim_{t\to 0} t^{-2/3} = \infty \quad . \tag{1.24}$$

At late times, the current asymptotically approaches the Pease-Braginskii current ($I \to I_{PB}$). Fig. 1.2 displays the Haines-Hammel curve with its current and time scales normalized to the Pease-Braginskii current and Haines-Hammel time respectively.

Using Eq. (1.22), the Haines-Hammel time for a solid hydrogen fiber of radius 14 μm is $\tau_{HH} \approx 88$ ns.

For high densities and higher Z_A source materials, the plasma will radiate as a blackbody surface rather than as a bremsstrahlung volume source until the plasma has been heated above some threshold temperature. The initial current rise rate may be more accurately given by a current vs. time curve which assumes blackbody radiative cooling rather than bremsstrahlung as given in Appendix B.

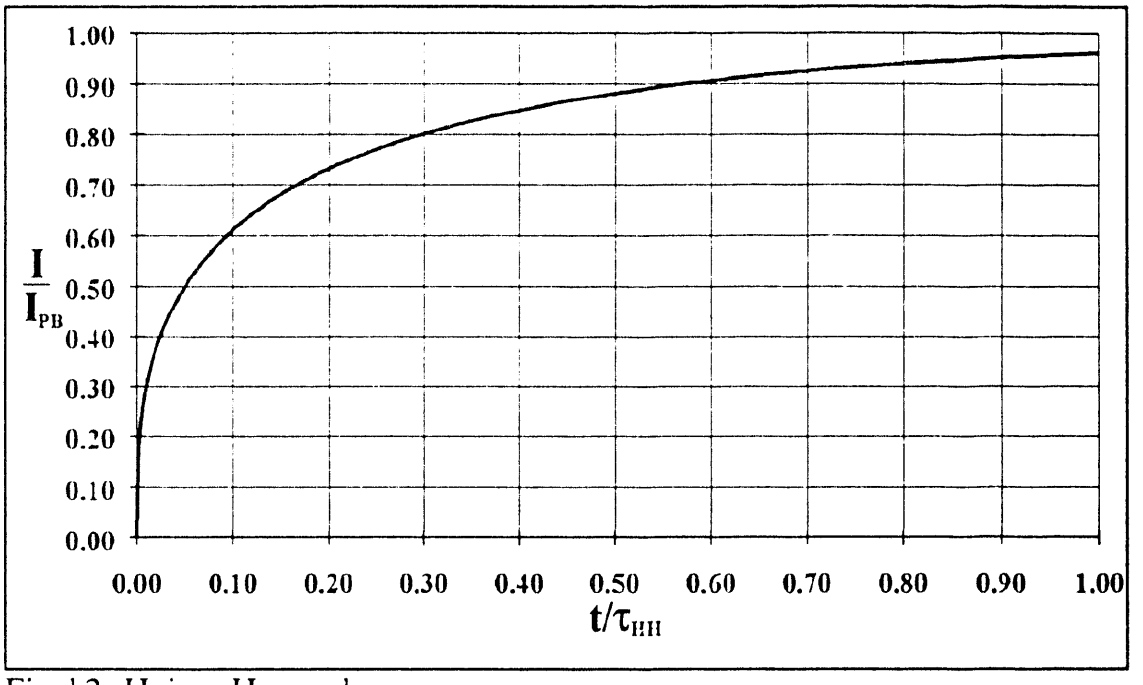

Fig. 1.2 Haines-Hammel curve.
The Haines-Hammel current is plotted in units of the Pease-Braginskii current (I_{PB}) vs. time in units of the Haines-Hammel time (τ_{HH}).

1.4. Z-Pinch Stability

A small, axially uniform change in the radius of a cylindrical z pinch in Bennett equilibrium will not grow into a larger change in radius if the ratio of pressure and volume specific heats (γ) of the plasma is greater than 1. If a pinch satisfying the Bennett relation, Eq. (1.3), is compressed during a time short enough for the current to be taken as constant, the temperature will increase due to PdV work, and the plasma will no longer be in pressure balance. For $\gamma > 1$, the change in temperature will cause the pinch to re-expand toward its original size until pressure balance is reestablished. This has the form of a restoring force against changes in radius.

Unfortunately, there are perturbations to the shape of the pinch that do not change the volume significantly but yield a lower energy state for the magnetic

field. By maintaining the same volume, there will be no net PdV work to change the kinetic pressure of the plasma if the shape changes slowly enough for the pressure to remain uniform within the volume of the plasma. The magnetic forces produced by the current in the plasma will reshape the plasma to achieve its highest inductance. Just as a pinch of smaller radius has a higher inductance, a pinch with a sinusoidal variation of radius as a function of position along the axis will have a higher inductance than a straight column of the same volume. A pinch whose radius varies with axial position as

$$r_{m=0} = r_0 + \xi_\kappa \sin(\kappa z) \quad (m) \quad , \tag{I.25}$$

where $\kappa \equiv 2\pi i/\ell$ (rad/m), for an integer i, has the same volume as a straight column of radius

$$r_s = \sqrt{r_0^2 + \xi_\kappa^2} \quad (m) \quad . \tag{I.26}$$

The difference of the inductances of the perturbed and straight columns is

$$L_{m=0} - L_s = \frac{\mu_0 \ell}{4\pi} \ln\left[\frac{4\left(r_0^2 + \xi_\kappa^2\right)}{2r_0^2 - \xi_\kappa^2 + 2r_0\sqrt{r_0^2 - \xi_\kappa^2}}\right] \approx \frac{3\mu_0 \ell}{8\pi}\left(\frac{\xi_\kappa}{r_0}\right)^2 \quad (H) \quad , \tag{I.27}$$

assuming $\xi_\kappa < r_0$ and a thin current skin depth. This deformation is often called a "sausage" instability due to its shape as shown in Fig. I.3, and is labeled $m=0$ for reasons given below.

Theoretical analyses of pinch stabilization were published in the late 1950s for the case of a thin current sheath[24,25] and for plasma and current distributions that are continuous over the radius of the pinch[26]. These analyses used a Fourier decomposition of the perturbation in the pinch shape as

$$\delta r \equiv \xi = \sum_{m,\kappa} \xi_{m,\kappa}(r)\, e^{i(m\theta + \kappa z)} \quad (m) \quad , \tag{I.28}$$

where m is the mode number and κ is the axial wave number. Pinch stability is described in terms of these modes. This is the origin of the labeling of distortions

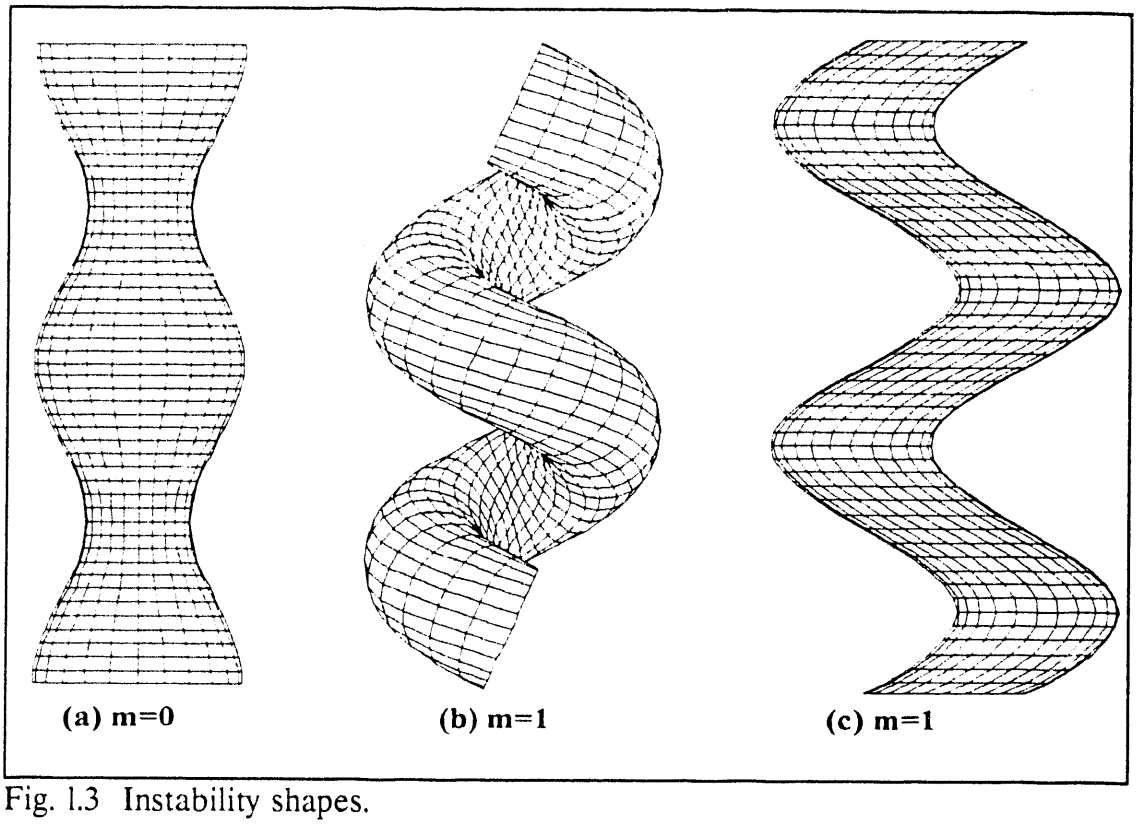

Fig. 1.3 Instability shapes.
(a) $m=0$ "sausage," (b) $m=1$ "helix," and (c) $m=1$ "kink".

by the integer $m=0,1,....$ The wire plots in Fig. 1.3 show the shapes of the modes seen most often in experiments, the $m=0$ "sausage" mode and the $m=1$ "helix" and "kink" modes.

Kadomtsev[27,28] showed that for a z pinch to be $m=0$ stable without an external B_z the plasma kinetic pressure p must satisfy the condition

$$-\frac{r}{p}\frac{dp}{dr} < \frac{4\gamma}{2+\gamma\beta} \approx \frac{20}{11} \quad , \tag{1.29}$$

where $\beta = p(2\mu_0/B) \approx 1$ is the local thermal to magnetic pressure ratio and γ is the ratio of pressure and volume specific heats[29],

$$\gamma \equiv c_p / c_v = (f+2)/f \approx 5/3 \quad , \tag{1.30}$$

where f is the number of degrees of freedom of particles, which equals 3 for an ideal gas. When the magnetic field does not compress the plasma within the ion thermal isotropy time, the compression can be taken to have three degrees of freedom, otherwise it will have two[30]. It will be assumed that $f=3$ for the 0-D simulation described in the next chapter.

1.5. Z-Pinch Instability Growth Rate

This section gives a scaling argument for the growth rate of the $m=0$ instability. The growth rates of higher modes are not discussed because they have not been observed on HDZP-II. A growth rate is one over the "*e* folding" time, $\tau_{m=0}$, at which perturbations grow ($\delta r = \delta r_0 \, e^{(t-t0)/\tau}$). The $m=0$ growth rate is used in the derivation of the turbulent heating term in the next chapter.

Under the assumption that the skin depth of the current is small compared to the radius and treating the plasma as an incompressible fluid, Kadomtsev[31] derived the $m=0$ growth rate to be

$$\frac{1}{\tau_{m=0}} = \frac{v_A}{r} \sqrt{\frac{\kappa r I_1(\kappa r)}{2\pi I_0(\kappa r)}} \le 1/\sqrt{4\pi} \, \frac{v_A}{r} \approx 0.3 \, \frac{v_A}{r} \quad (s^{-1}) \, , \tag{1.31}$$

where I_0 and I_1 are modified Bessel functions of the first kind of order 0 and 1, and the Alfvén speed is defined as

$$v_A = \frac{B_\theta}{\sqrt{\mu_0 \rho}} = \sqrt{\frac{\mu_0}{\rho} \frac{I}{2\pi r}} \quad (m/s) \, . \tag{1.32}$$

where the magnetic field is that of a current through a wire.

The current skin depth[32] of plasmas created in HDZP-II is

$$\delta = \sqrt{\frac{t\,\eta_{Spitz}}{\pi\,\mu}} \approx 5.11\,\sqrt{t\,\overline{Z\ln\Lambda}\;T_e^{-3/2}} \approx 100\;\mu m\;, \tag{1.33}$$

where η_{Spitz} is the Spitzer resistivity, at t = 20 ns into the current, at an electron temperature of T_e = 100 eV, and $\overline{Z\ln\Lambda}$ = 25. At 20 ns into the main current, the radius is typically measured to be 600 μm. The ratio of calculated skin depth to measured radius decreases after this time. The assumption of thin current skin depth seems a little marginal at early times, but at these times the Joule heating based on Spitzer resistivity with uniform current density is greater than the turbulent heating based on the assumption of thin current skin depth.

This growth rate is based on linearized, ideal MHD theory and so describes the growth of the perturbations while they are still small enough to be considered linear effects.

The assumption of incompressibility seems reasonable during the initial growth of the instability. While the perturbation remains small, the pinch is in near pressure balance and so the Alfvén speed is approximately equal to the thermal speed. Initially the plasma temperature and kinetic pressure can equilibrate by axial flow of thermal energy and particles. For constant density within the plasma, the Alfvén velocity at the surface of the plasma is proportional to the inverse of the local pinch radius. If one axial section of the pinch expands and another section, of the same length, each contracts at their local Alfvén speeds, there is no change in the volume of the plasma.

The instability will quickly grow to the point where the assumption of incompressibility no longer holds. When the plasma has contracted to a fraction of its unperturbed radius, its Alfvén speed will become much larger than the original ion thermal speed. The plasma density and temperature will begin to build up at the snowplow shock front, decreasing the contraction speed, and eventually the shock front will stagnate on the axis.

It will be assumed in the turbulent heating model, described in the next chapter, that the time required for an $m=0$ instability to reach this stagnation point scales as the Kadomtsev instability growth rate

$$\tau \propto r / v_A \quad (s) \,. \tag{I.34}$$

The Alfvén speed used assumes a thin skin-depth of the current and constant density within the plasma-vacuum boundary. Uniform density becomes a weak assumption when the Alfvén speed, calculated for the rate of convergence of the neck of the $m=0$ instability toward the axis, greatly exceeds the ion thermal speed.

II THEORY

The theory presented in this chapter includes discussion of the additional complexities due to using deuterated-polyethylene CD_2 fibers instead of pure hydrogen isotopes for the source material of the z-pinch plasma. A zero-dimensional model of a z pinch will be presented. A method of calculating instability heating power is also developed. The equations are in mks units except energies and temperatures, which are in eV.

2.1. Plasma Ionization

All the radiation mechanisms discussed in this chapter depend on the degree of ionization of the plasma. The Spitzer resistivity, the plasma pressure, and the plasma internal energy are also dependent on the plasma ionization. It will be assumed that the ionization is described by Saha equilibrium based on the plasma being in local thermodynamic equilibrium, as described below.

2.1.1. Local Thermodynamic Equilibrium

Local thermodynamic equilibrium (LTE) requires that the densities of excited states and ionization states be in thermal equilibrium with the free electrons. (Excitation state refers to the state of an electron bound to an ion, and ionization state refers to the level of ionization of ions within the plasma.) Electron collisions with ions maintain the populations of these states. LTE does not require the radiation to be thermal (i.e., blackbody), nor does it require the ion and electron temperatures to be the same.

The HDZP-II plasma stays sufficient dense[33]

$$n_e > 10^{19} \sqrt{T_e}\,(\Delta E)^3 \qquad (m^{-3}) \ , \tag{2.1}$$

where ΔE is the energy difference in eV between states, to be considered in LTE, until the carbon is ionized to the helium-like C^{+4} level (Fig. 2.1). The ionization

TABLE I. Carbon ionization potentials $\Delta E_{i,\infty}$ and first two excitation energies from the ground state $\Delta E_{i,1}$, $\Delta E_{i,2}$ for ionization states 0-5.

	C^{+0}	C^{+1}	C^{+2}	C^{+3}	C^{+4}	C^{+5}
$\Delta E_{i,\infty}$ (eV)	11.260	24.384	47.888	64.494	392.09	490.00
$\Delta E_{i,2}$ (eV)	2.684	9.291	12.690	38.400	354.00	435.00
$\Delta E_{i,1}$ (eV)	1.264	5.334	6.486	8.008	304.40	367.54

potential at this ionization level is more than five times as large as at the lithium-like C^{+3} level, as shown in TABLE I[34]. For energy differences that exceed the condition given in Eq. (2.1), the electron-collision rate will drop below that required for the density of excited states to be in thermal equilibrium with the free electrons.

It will be assumed that the pinch plasma remains in LTE. This may underestimate the line-radiation cooling power, described later in this chapter, by overestimating how quickly the carbon ions in the plasma become fully stripped. The plasma is highly ionized at the time that LTE becomes a weak assumption. Under these conditions, the excitation levels can be thought of as being in detailed balance with the next ionization level. The change in energy between an excited state and the continuum is less than the excitation energy from the ground state. When the plasma generated by HDZP-II reaches these conditions, the radiated power becomes small compared to the Joule heating. The weakness of the assumption of LTE at this time only introduces small corrections to the radiated power as it is becoming insignificant for a short time before the plasma becomes fully ionized.

2.1.2. Saha Equilibrium

Particle densities of ions at the various ionization states in a plasma in LTE can be expressed in terms of the Saha equation[35]

$$\frac{n_{i+1}}{n_i} = \frac{z_{i+1}}{z_i}\frac{2}{n_e}\left[\frac{m_e e T_e}{2\pi\hbar^2}\right]^{3/2} e^{-\frac{\Delta E_i}{T_e}} \approx \frac{6.04\times10^{27}}{n_e}\frac{z_{i+1}}{z_i} T_e^{3/2} e^{-\frac{\Delta E_i}{T_e}} \qquad (2.2)$$

where ΔE_i is the ionization potential in eV of an ion in its ith ionization state, and the partition function for the ith ionization state is[36]

$$z_i = g_{i,0} + \sum_{k=1}^{n} g_{i,k}\, e^{-\Delta E_{i,k}/T_e} \quad , \qquad (2.3)$$

where k is the index over excitation states and $g_{i,k}$ are the statistical weights of the excitation states. A nondegenerate state has $g=1$ and a free electron has $g=2$ due to its spin degeneracy. The summation over the partition functions is terminated at the second excitation state for the calculations reported in this document. This truncates the series at a lower limit than is required by continuum lower, which is described in the next section; however, the higher order terms not included are small corrections to the partition function.

2.1.3. Continuum Lowering

An electron excited to a state whose radius is comparable to the interatomic spacing $a_{Max} \equiv (\Sigma_i)^{-1/3}$ can move freely from ion to ion. The summations of the partition functions over excitation states must be terminated when the radius of the state becomes comparable to the interatomic spacing. This is referred to as "continuum lowering" because electrons excited above this limit are in a continuum of states within the plasma. Plasmas created in HDZP-II are dense enough for continuum lowering to be a noticeable effect only for the first 10 ns.

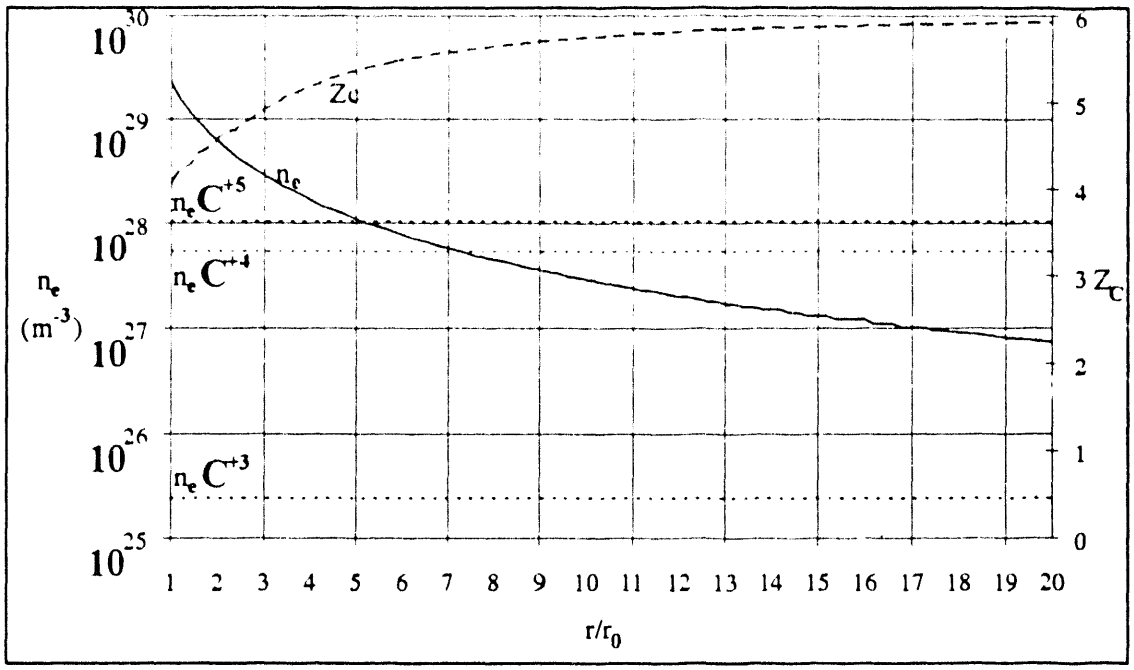

Fig. 2.1 Calculated n_e and Z_c vs. r/r_0 of CD_2 plasma at T_e = 80 eV.
The electron densities required for LTE to be valid for the ionization transitions from lithium-like C^{+3} ($n_e > 2.5\times10^{25}$ m^{-3}), helium-like C^{+4} ($n_e > 5.4\times10^{27}$ m^{-3}), and hydrogen-like C^{+5} ($n_e > 10^{28}$ m^{-3}) are also drawn as horizontal lines. The average carbon ionization $Z_c = \Sigma Z_{ic} n_{ic} / \Sigma n_{ic}$ is plotted relative to a linear scale.

Less energy is required to excite an electron from a bound state to the plasma continuum than to remove the electron from the ion in free space. The effective reduction of the ionization potential, including Debye shielding, is[37]

$$\delta E_i = T_e \frac{\left\{\min\left[1, (a_{Max}/\lambda_D)^3\right] + 1\right\}^{2/3} - 1}{2(Z_i + 1)} \quad (eV) \quad . \tag{2.4}$$

where the Debye length is

$$\lambda_D = \sqrt{\epsilon_0 T_e / n_e e} \quad (m) \quad . \tag{2.5}$$

If $\lambda_D < a_{Max}$, the ratio is replaced by 1. in Eq. (2.4) to insure that there is more than one electron in the effective Debye sphere. Continuum lowering does not

affect the difference in energy between excitation states; it only lowers the energy required to remove an electron from a bound state to the plasma continuum.

The plots in Fig. 2.1 show the calculated electron density and average carbon ionization (Z_c) of a CD_2 plasma at an electron temperature of 80 eV as a function of expansion radius assuming a uniform expansion from a solid-fiber radius of r_0 = 20 μm. The electron temperature of 80 eV was chosen because it is comparable to the experimentally measured values. The calculations are based on Saha equilibrium with continuum lowering and assume the plasma is in LTE.

When the plasma has expanded in radius by a factor of seven, the calculated electron density drops below that required for LTE with the ionization of carbon from helium-like C^{+4} to hydrogen-like C^{+5}. The density drops below that required for LTE with the ionization from hydrogen-like C^{+5} to fully ionized when the radius has expanded by a factor of five.

2.2. Plasma Electromagnetic Radiation

The electromagnetic radiation emitted by the pinch plasma is used as a diagnostic of the electron temperature, and radiative cooling has a strong effect on the dynamics of the plasma. This section discusses the different radiation mechanisms and their relative importance in the parameter regime relevant to HDZP-II plasmas.

2.2.1. Bremsstrahlung Radiation

Bremsstrahlung radiation is produced by free-free electron collisions with ions. Bremsstrahlung becomes the strongest radiation mechanism when the plasma achieves full ionization and is similar in form to the free-bound radiation mechanism described in the next section. The bremsstrahlung spectral power per unit volume emitted into 4π steradians has the form

$$4\pi j_{Br}(\omega) = \frac{C_{Br} g_{Br}}{\sqrt{eT_e}} e^{-\frac{E_\omega}{T_e}} n_e \Sigma Z_i^2 n_i \qquad \left(\frac{J}{m^3}\right) , \tag{2.6}$$

where

$$C_{Br} = \sqrt{\frac{8\pi}{27}} \left(\frac{2\hbar^2}{a_0 c m_e^{3/2}}\right)^3 \approx 4\times 10^{-63} \quad J^{3/2} \bullet m^3 , \tag{2.7}$$

is the bremsstrahlung emission coefficient, $E_\omega \equiv \hbar\omega/e$ is the photon energy in eV, and $g_{Br} \approx 1.4$ is the bremsstrahlung Gaunt factor, a quantum-mechanical correction to the classical derivation of the bremsstrahlung power.

The quantum-mechanical nature of the emitted photons becomes important for $\hbar\omega > eT_e$. A full quantum treatment has been performed by Sommerfeld[38], resulting in Gaunt factors expressed in terms of hypergeometric functions. The thermal averages of these Gaunt factors have been computed numerically by Karzas and Latter[39]. The bremsstrahlung Gaunt factor will be approximated as $g_{Br} = 1.4$, which is averaged over the whole bremsstrahlung spectrum for electron temperatures on the order of $Z_i^2 R_y$.

Integrating over all frequencies, the bremsstrahlung power emitted by a volume element dV is

$$P_{Br} \approx dV\, g_{Br}\, B_{rm} \sqrt{T_e}\, n_e \Sigma Z_i^2 n_i \quad (W) , \tag{2.8}$$

where $B_{rm} \approx 1.5\times 10^{-38}$ W•m^3/eV$^{1/2}$ is the bremsstrahlung power coefficient.

For a $\beta = 1$ plasma, in which magnetic pressure balances kinetic pressure, the power due to cyclotron radiation is

$$P_{Cy} \approx 5\times 10^{-44}\, dV \sqrt{T_e}\, n_e^2 \quad (W) , \tag{2.9}$$

which is clearly negligible compared with bremsstrahlung emission.

2.2.2. Recombination Radiation

Recombination radiation is produced when an ion captures a free electron and emits a photon with energy equal to that of the free electron plus the ionization energy of the bound state. Because the free electrons are in a thermal distribution, the emission spectrum is a continuum above a cutoff energy equal to this ionization potential. TABLE I gives the ionization potentials for carbon. Kramers[40] estimated the semiclassical cross section for bound-free absorption of radiation from the correspondence principle. The quantum corrections are again expressed in terms of a Gaunt factor G_k. Karzas and Latter[38] have computed these Gaunt factors, and they remain within 20% of 1.0 for $\hbar\omega < 10\, Z_i^2 eR_y/k^2$, where k is the quantum number of the capture bound state. These recombination Gaunt factors will be assumed to be one in all calculations presented.

The free-bound radiant volumetric emissivity[41] is very similar to that of bremsstrahlung,

$$4\pi j_{i,k}(\omega) = \frac{C_{Br} n_e Z_i^2 n_i}{\sqrt{e\, T_e}} \left[\frac{Z_i^2 R_y}{T_e} \frac{2G_k}{k^3} e^{\frac{Z_i^2 R_y/k^2 - E_\omega}{T_e}} \right] \left(\frac{J}{m^3} \right), \qquad (2.10)$$

except that $j_{i,k}(\hbar\omega < Z_i^2 eR_y/k^2) = 0$. The integrated power for this free-bound transition is then

$$P_{i,k} \approx 4.2 \times 10^{-37}\, dV\, T_e^{-1/2}\, n_e\, n_i\, Z_i^4/k^3 \quad (W)\ . \qquad (2.11)$$

The recombination emission is brighter than bremsstrahlung for $g_{Br} T_e \le 2Z_i^2 R_y/k^3$ at photon energies above $Z_i^2 R_y/k^3$. Bremsstrahlung will dominate in a hydrogen plasma for electron temperatures $T_e \ge 20$ eV, but recombination radiation will continue to dominate until ~700 eV in a plasma with a large fraction of carbon ions.

The sum of bremsstrahlung and all of the free-bound emissivities is then[42]

$$4\pi j(\omega) = \frac{C_{Br}}{\sqrt{e T_e}} e^{-\frac{E_\omega}{T_e}} n_e \sum_i \left[Z_i^2 n_i \left(g_{Br} + \frac{Z_i^2 R_y}{T_e} \sum_k \frac{2G_k}{k^3} e^{\frac{Z_i^2 R_y}{k^2 T_e}} \right) \right] \left(\frac{J}{m^3} \right), \quad (2.12)$$

with the inner sum limited by $j_{i,k}(\hbar\omega < Z_i^2 eR_y/k^2) = 0$. The ionization potentials should be reduced, and the summation over k should be truncated due to continuum lowering, as described earlier in this chapter.

2.2.3. Radiant Absorption and Blackbody Radiation

Each radiative process has an inverse, absorption process. This has the effect of limiting the total power radiated by a volume of plasma at an angular frequency ω to less than or equal that of a "blackbody" emitter. The intensity radiated per steradian, per unit angular frequency, at angular frequency $\omega > \omega_p$ traveling through a plasma changes as[43]

$$\frac{dI}{ds} = j(\omega) - I\alpha(\omega) \quad \left(\frac{J}{m^3 \bullet sr} \right), \quad (2.13)$$

where ds is the increment in path length, j is the radiant volumetric emissivity, and α is the absorption coefficient. For $d/ds\ (j/\alpha) = 0$, this equation has the solution

$$I_{out} = I_{inp}\, e^{-\tau} + \frac{j(\omega)}{\alpha(\omega)} \left[1 - e^{-\tau} \right] \quad \left(\frac{J}{m^2 \bullet sr} \right), \quad (2.14)$$

where $\tau(\omega) \equiv \int \alpha(\omega)\, ds$ is the "optical thickness." A plasma is called optically "thick" for $\tau > 1$ and "thin" for $\tau < 1$.

A blackbody is optically thick over all frequencies ($\tau \to \infty$) and has the spectrum

$$I_{BB} = \frac{j(\omega)}{\alpha(\omega)} = \frac{e^3}{8\pi^3\hbar^2c^2} \frac{E_\omega^3}{e^{E_\omega/T_e} - 1} \left(\frac{J}{m^2 \bullet sr}\right) , \tag{2.15}$$

which is an expression of Kirchhoff's law. The total power emitted into 2π steradians from a blackbody surface of area A has the familiar form

$$P_{BB} = A\ \sigma_{SB}\ T_e^4 \qquad (W) , \tag{2.16}$$

where $\sigma_{SB} \equiv \pi^2 e^4/60\hbar^3c^2 \approx 1.03 \times 10^9$ W/m^2•eV^4 is the Stefan-Boltzmann constant.

The absorption coefficient for bremsstrahlung and free-bound processes is then

$$\alpha(\omega) = A_{Br} \frac{1 - e^{-\frac{E_\omega}{T_e}}}{E_\omega^3 \sqrt{T_e}} n_e \sum_i \left[Z_i^2 n_i \left(g_{Br} + \frac{Z_i^2 R_y}{T_e} \sum_k \frac{2G_k}{k^3} e^{\frac{Z_i^2 R_y}{k^2 T_e}} \right) \right] (m^{-1}) , \tag{2.17}$$

where $A_{Br} \equiv C_{Br} h^2 c^2 e^{-7/2}/2 \approx 5 \times 10^{-47}$.

2.2.4. Line Radiation

Line (bound-bound) radiation is emitted when a bound electron undergoes a transition to a lower energy state of the same ion. Bound electrons in an LTE plasma are excited to higher states primarily by collisions with free electrons. In HDZP-II, line radiation is unimportant for a pure hydrogen plasma because it will be fully ionized before the electron temperature reaches $R_y \approx 13.6$ eV. However, carbon ions in a plasma will not be fully ionized for $T_e \approx 80$ eV until the plasma has expanded radially by a factor of at least ten, as shown in Fig. 2.1. The line radiative cooling power from ions in the ith ionization state can be approximated by that of its ground-state resonance line[44]

$$P_i \approx C_{line}\, dV\, n_e\, n_i\, e^{-\Delta E_{i1}/T_e} \ (W) , \tag{2.18}$$

where

$$C_{line} = 4\alpha c a_0^2 e\sqrt{\pi R_y^3} \approx 3.49\times10^{-31} \quad W\bullet m^3\bullet eV^{1/2} , \tag{2.19}$$

with the sum of the products of line strength and density of excited states approximated by half the density of ions at the *i*th ionization state. Line radiation power will be greater than the sum of bremsstrahlung and recombination powers for optically-thin plasmas.

Bound-bound radiation is referred to as "line radiation" because the power is usually emitted into narrow bands of optical frequencies, and is more optically thick than the continuous spectrum of bremsstrahlung and free-bound radiation. The doppler line-width is

$$\frac{\Delta\omega_{D1/2}}{\omega} \approx \frac{v_T}{c}\sqrt{2\ln(2)} \approx 3.86\times10^{-5}\sqrt{T_i/A_i} , \tag{2.20}$$

where A_i is the atomic mass number. However, the plasmas produced by HDZP-II are dominated by Stark broadening because of the high ion densities. A code written by Lee[45] calculated the full-width half-max of the Stark-broadened Lα line of hydrogen-like carbon to be $\hbar\Delta\omega_{S\,1/2} \approx 4$ eV at a temperature of 100 eV and a density corresponding to a radial expansion of ~5. The line width is increased by a factor of <2 by "opacity broadening", in which photons emitted as line radiation have inelastic collisions with free electrons, and escape the plasma in the wings of the line.

Due to "blackbody clipping", described in the next section, even lines of this width do not contribute a large fraction of the total power emitted by the HDZP-II, as shown in Fig. 2.2. At early times (< 10 ns), the plasma is optically thick based on bremsstrahlung and recombination processes alone. The plasma only becomes optically thin to theses processes when the plasma is almost fully ionized. The small contribution of line radiation to the total radiated power is negligible and is not included in the 0-D simulation.

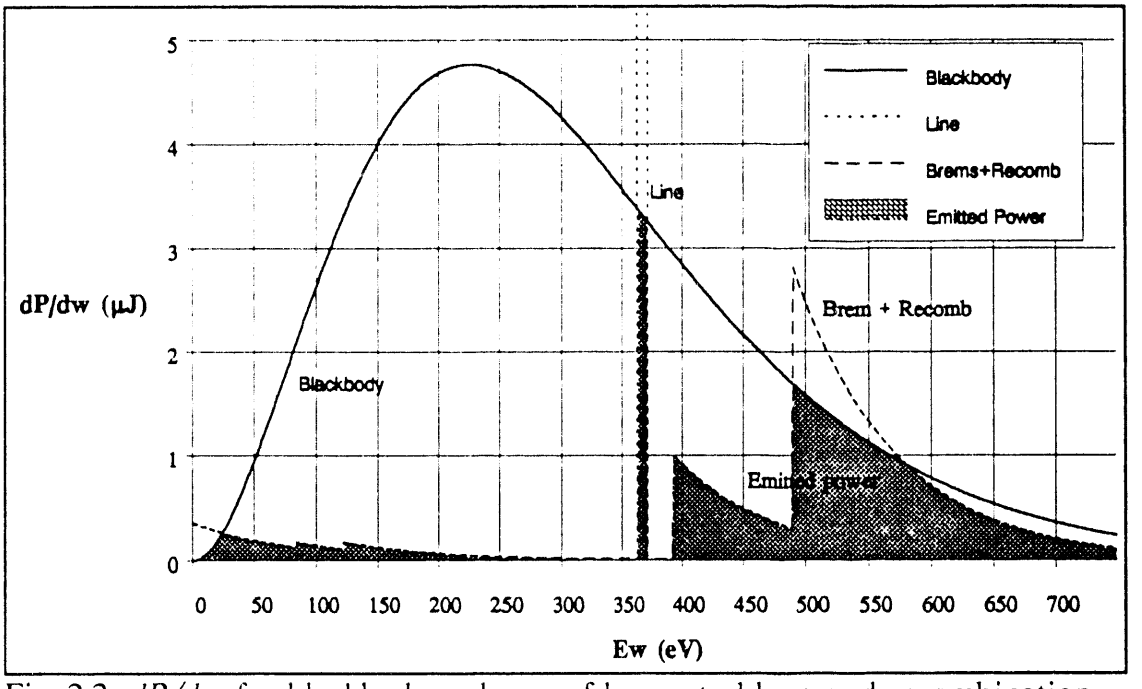

Fig. 2.2 $dP/d\omega$ for blackbody and sum of bremsstrahlung and recombination. Plots of power per unit angular frequency of blackbody and the sum of bremsstrahlung, recombination, and line radiation emitted from a 5-cm long cylinder of plasma vs. photon energy. The electron temperature is 80 eV and the plasma radius has uniformly expanded from solid-fiber radius $r_0 = 20\ \mu$m to $r = 200\ \mu$m.

2.2.5. Total Power Radiated from a Plasma Cylinder

The total radiative power is the sum of the bremsstrahlung and recombination emissivities integrated over the volume of the plasma and integrated over angular frequency. The volume range of this integral is limited by the reabsorption of the plasma. For an optically thick plasma contained in a cylinder of radius r and length ℓ, the radiated power that escapes the cylinder at an angular frequency ω is emitted by the outer shell that has an optical thickness of one at this angular frequency. Light emitted at a smaller radius, within the outer shell, would be reabsorbed by the shell. The power radiated in this case is further approximated by setting it equal to the power radiated by a blackbody

spectrum from the surface of the cylinder, with area $A = 2\pi r\ell$, into 2π steradians. If the geometric thickness of the shell exceeds the radius of the cylinder, the plasma can be taken to be optically thin at this angular frequency and the whole volume emits into 4π steradians.

The total power radiated by a cylinder of plasma is then

$$P_{Rad} = 4\pi^2 r\ell \int_0^\infty d\omega \; Max\{I_{BB}(\omega), r[j_{Brem}(\omega) + j_{Rec}(\omega)]\} \; (W) \; . \tag{2.21}$$

The plots in Fig. 2.2 show the blackbody spectrum and the sum of the bremsstrahlung and recombination spectra. The shaded region shows the bremsstrahlung-recombination power that has been "clipped" to the blackbody threshold. The spectra were calculated for an electron temperature of 80 eV, a solid-fiber radius of 20 μm, and a radial expansion of ten.

The plots in Fig. 2.3 show the total radiated power computed based on these assumptions divided by the blackbody radiative power over a range of radial expansions, for electron temperatures 30, 100, and 300 eV. These plots can be thought of as the optical thickness of the cylinder averaged over all photon energies. The sudden drops in this averaged optical thickness are due to the carbon ions becoming fully ionized. The 30 eV curve has an additional drop due to the ions reaching a helium-like ionization.

2.3. Zero-Dimensional Simulation

A simple 0-D simulation was used to model the relevant physics. The source code is given in Appendix C. This simulation will be used, in chapter 5, to compare a number of physical models with the data presented in chapter 4. This simulation assumes that the pinch is quasi-neutral ($n_e = \Sigma Z_i n_i$) within a straight cylinder of length $\ell = 5$ cm and variable radius r. The temperature and

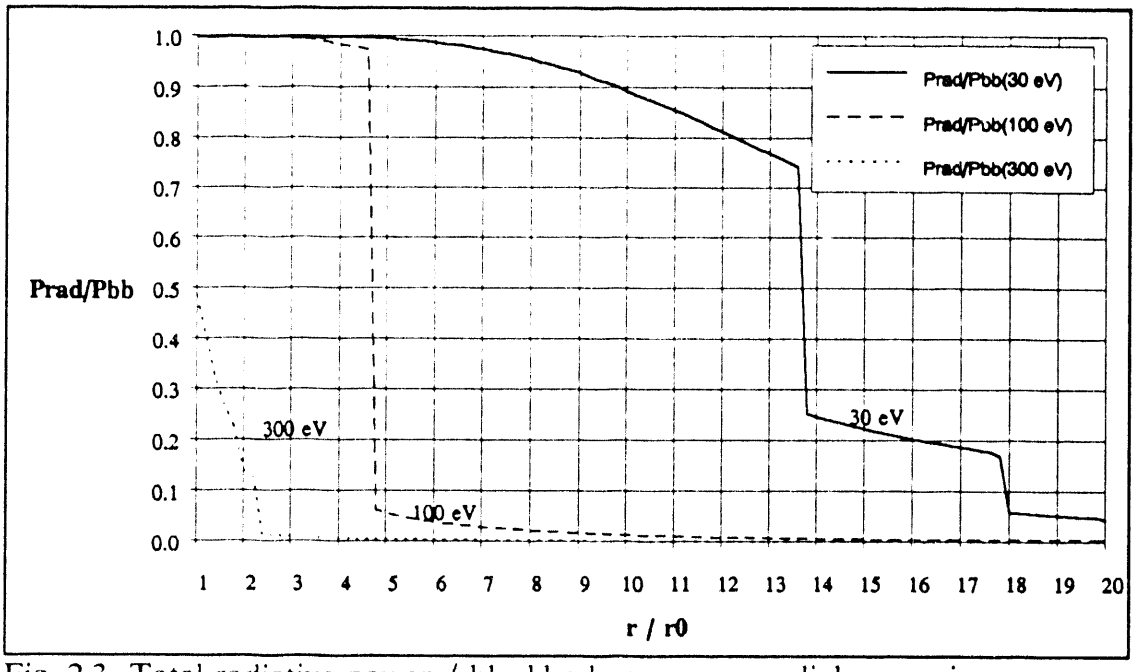

Fig. 2.3 Total radiative power / blackbody power vs. radial expansion.
Plots of the calculated total radiated power divided by the blackbody power vs. radial expansion from a solid-fiber radius of 20 μm. The curves were calculated for electron temperatures of 30, 100, and 300 eV.

density of each particle species is assumed to be uniform within the volume of this cylinder. The Joule-heating term assumes that the current density is uniform throughout the volume of the cylinder.

The electron density will be shown to be sharply peaked on the pinch axis and the shape of the plasma will be shown to different form a cylinder in chapter 4. The assumption of uniform particle density within a straight cylinder will underestimate the radiative cooling power and the neutron yield slightly. A uniform current density would require a particle density which falls off as r^{-2} to be in pressure balance; a uniform particle density would require the current to flow on the surface. A uniform current density gives the minimum resistance and is inconsistent with the thin current skin depth assumed by the turbulent heating term.

2.3.1. Dependent Variables

The 0-D simulation integrates a system of ordinary differential equations (ODEs) over time to solve them for a set dependent variables that are relevant to the evolution of the pinch plasma. The radius and radial velocity of the cylinder are required to describe the plasma dynamics. Since the particle densities are assumed uniform within the cylinder, the densities of the ions are specified by the radius and the solid-fiber radius, and are not dependent variables in the ODEs. To simplify the equations, the thermal energy densities, U_e, U_d, and U_c, for each particle species (electron, deuterons, and carbon ions) are solved for rather than the corresponding temperatures. The energy density of each particle species is computed separately because each species develops a different temperature during the simulation. The total neutron production from thermonuclear D-D fusion reactions is also computed.

2.3.2. Differential Equations

The set of coupled ODE's given below are integrated over time from initial conditions by the Bulirsch-Stoer method with Richardson rational extrapolation[46]. The Bulirsch-Stoer method requires input functions to be continuous to the first derivative. The input pinch current data was fitted by the Akima cubic spline which minimizes second derivatives of the fit, and is continuous to the first derivative. This integration method is very fast and accurate for non-stiff systems of ODE's, as long as the solution does not come too close to numerical singularities. Assuming that the system of equations are non-stiff requires the integration to proceed at the time step of the equation that varies most rapidly. Using a non-stiff integration method may be slower for a stiff set of equations, but the accuracy of the result should not be affected.

A repulsive force was added to prevent radial collapse, avoiding a singularity at $r = 0$; this force only becomes significant when the radius falls below one micron. The integration step size was limited to prevent the variables from obtaining nonphysical values, such as negative energy densities.

The following set of six equations constitute the 0-D simulation:

$$\frac{dr}{dt} = v_r \quad (m/s) \; ; \tag{2.22}$$

$$\frac{dv_r}{dt} = \frac{3\pi r \ell}{M}\left[\frac{2e}{3}\sum U - \frac{\mu_0 I^2}{8\pi^2 r^2}\right] - \frac{v_r}{5\times10^{-9}} + \frac{10^5}{(r-10^{-7})^4} \; (m/s^2), \tag{2.23}$$

where $M = \ell \Sigma N_i m_i$ (kg) is the mass of the pinch. This equation assumes that the particle densities remain uniform as the radius changes, giving a reduced column mass of $(2/3)M$. The first term is the radial acceleration due to the imbalance of particle and magnetic pressures. The second term dampens oscillations in the radial velocity with a 5 ns decay time, to reduce "ringing" in the radius time history. The last term prevents radial collapse. The thermonuclear neutron yield is calculated as

$$\frac{dn_{neut}}{dt} = \ell \pi r^2 n_d^2 \, \overline{\sigma v}_{DD} \approx 2.33\times10^{-18} \, \ell \, \frac{N_d n_d}{T_d^{2/3}} \, e^{-\frac{187.6}{T_d^{1/3}}} \; (s^{-1}) \; , \tag{2.24}$$

where n_d is the deuteron particle density in m^{-3} and the temperature of deuterons (and each particle species) is related to its energy density as $U_d = (3/2)\, T_d\, n_d$. The energy density, in eV/m^3, of each particle species changes as

$$\frac{dU_c}{dt} = \psi_{ce}(T_e - T_c) + \psi_{cd}(T_d - T_c) - \frac{2\gamma v_r}{r} U_c + \frac{m_c}{m_c + 2m_d} \frac{P_{Turb}}{V} \left(\frac{eV}{m^3 \bullet s}\right), \tag{2.25}$$

$$\frac{dU_d}{dt} = \psi_{de}(T_e - T_d) + \psi_{cd}(T_c - T_d) - \frac{2\gamma v_r}{r} U_d + \frac{2m_d}{m_c + 2m_d} \frac{P_{Turb}}{V} \left(\frac{eV}{m^3 \bullet s} \right), \quad (2.26)$$

and

$$\frac{dU_e}{dt} = \psi_{de}(T_d - T_e) + \psi_{ce}(T_c - T_e) - \frac{2\gamma v_r}{r} U_e + \frac{P_{Joule} - P_{Rad} - P_{Ionz}}{V} \left(\frac{eV}{m^3 \bullet s} \right), \quad (2.27)$$

where m_c, m_d, and m_e are the particle masses and the adiabatic expansion coefficient is set to $\gamma = 5/3$ (the value given by Eq. (1.30) for a gas with three degrees of freedom.) P_{Turb} is the turbulent-heating power described at the end of this chapter. P_{Joule} is defined by Eq. (1.11) as the power input to the electrons by Joule-heating with Spitzer-resistivity. P_{Rad} is defined in Section 2.2 as the total radiative power. P_{Ionz} (described below) is the power that is required to increase the plasma ionization.

The inter-particle thermalization coefficients are

$$\psi_{dc} = \psi_{cd} = \frac{3n_d}{2\tau_{dc}} = \frac{8.5 \times 10^{-27} \sqrt{m_c m_d}}{(m_c T_c + m_d T_d)^{3/2}} n_d \Sigma n_{ci} Z_{ci}^2 \ln\Lambda_{d,ci} \left(\frac{m^{-3}}{s} \right), \quad (2.28)$$

$$\psi_{ec} = \psi_{ce} = \frac{3n_e}{2\tau_{ec}} = \frac{8.5 \times 10^{-27} \sqrt{m_c m_e}}{(m_c T_c + m_e T_e)^{3/2}} n_e \Sigma n_{ci} Z_{ci}^2 \ln\Lambda_{e,ci} \left(\frac{m^{-3}}{s} \right), \quad (2.29)$$

and

$$\psi_{de} = \psi_{ed} = \frac{3n_d}{2\tau_{de}} = \frac{8.5 \times 10^{-27} \sqrt{m_e m_d}}{(m_e T_e + m_d T_d)^{3/2}} n_d n_e \ln\Lambda_{d,e} \left(\frac{m^{-3}}{s} \right), \quad (2.30)$$

where the summations are over the carbon ionization states and τ_{cd}, τ_{ce}, and τ_{de} are the inter particle species thermal equilibration times in seconds.

The ionization and the rate of change of ionization are computed at every major time-step (1 ns) based on Saha equilibrium. This process cools electrons which free bound electrons by inelastic collisions. The ionization power is computed by calculating the change in the Saha ionization state projected 1 ps into the future. The integration time step is typically much larger than 1 ps. The power is the amount of energy required to achieve this change in ionization divided by the 1 ps time. Subtracting this power from the projected change in electron temperature changes the projected ionization. This calculation is iterated until the projected change in the electron temperature is consistent with the projected change in ionization. This is assumed to be strictly an electron cooling process; if the ionization decreases, the ionization power is set to zero.

2.3.3. Initial Conditions

The 0-D simulation was run using the measured the current waveforms and solid-fiber radii for shots on the HDZP-II experiment. The starting radius was chosen from a sequence of radii measured at 10-ns intervals by the multiframe circular-schlieren diagnostic, which is described in the next chapter. The starting radius (r_1) was selected at a time when Spitzer resistivity is valid.

To avoid the complex ablation and ionization process of the solid fiber, the simulation assumes that the fiber is fully vaporized (no solid core) and that the plasma temperature is high enough for Spitzer resistivity to be valid, $ln\Lambda > 0.1$. The simulation is started no earlier than 15 ns before the start of the main current, after the current has risen above 10 kA.

The starting time of the simulation relative to the current waveform (t_1) is the time at which the starting radius was measured. The initial velocity is taken as the difference from the previous measured radius divided by 10 ns:

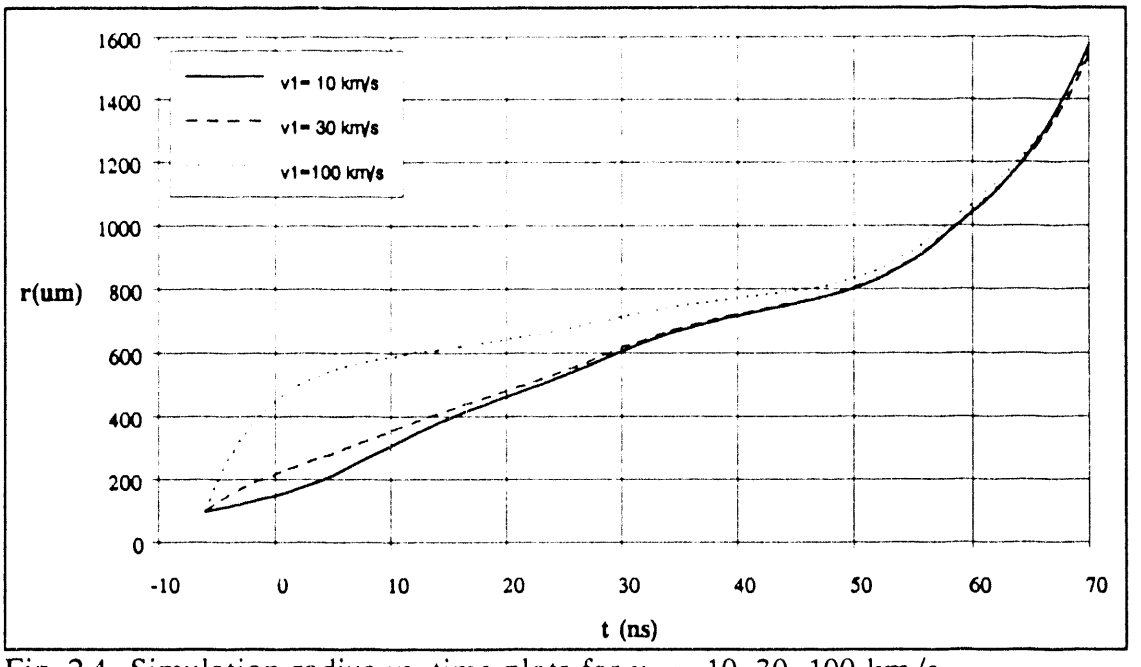

Fig. 2.4 Simulation radius vs. time plots for v_1 = 10, 30, 100 km/s. Experimentally measured starting velocities are typically in the range of 3-10 km/s. An increase of almost a factor of ten in the starting velocity is required to produce noticeable different results.

$$v_1 = [r_1 - r(t_1 - 10ns)] / 10ns \quad (m/s) \; . \tag{2.31}$$

The plots in Fig. 2.4 show the simulation of the turbulently heated model run for initial velocities of 10, 30, and 100 km/s. A plot for v_1 = 3 km/s is not included because it is indistinguishable from the plot for an initial velocity of 10 km/s. The initial velocity must be increased by a factor of almost ten to have a noticeable effect; this shows that the simulation is insensitive to the choice of initial velocity.

The initial temperature, assumed equal for all species at early times, was set to the Bennett temperature based on the solid-fiber radius and the current at the starting time. The initial temperature must exceed ~1 eV to be consistent with Spitzer resistivity. If the initial Bennett temperature is less than 1 eV, the simulation is started later into the main current. The Bennett temperature is a

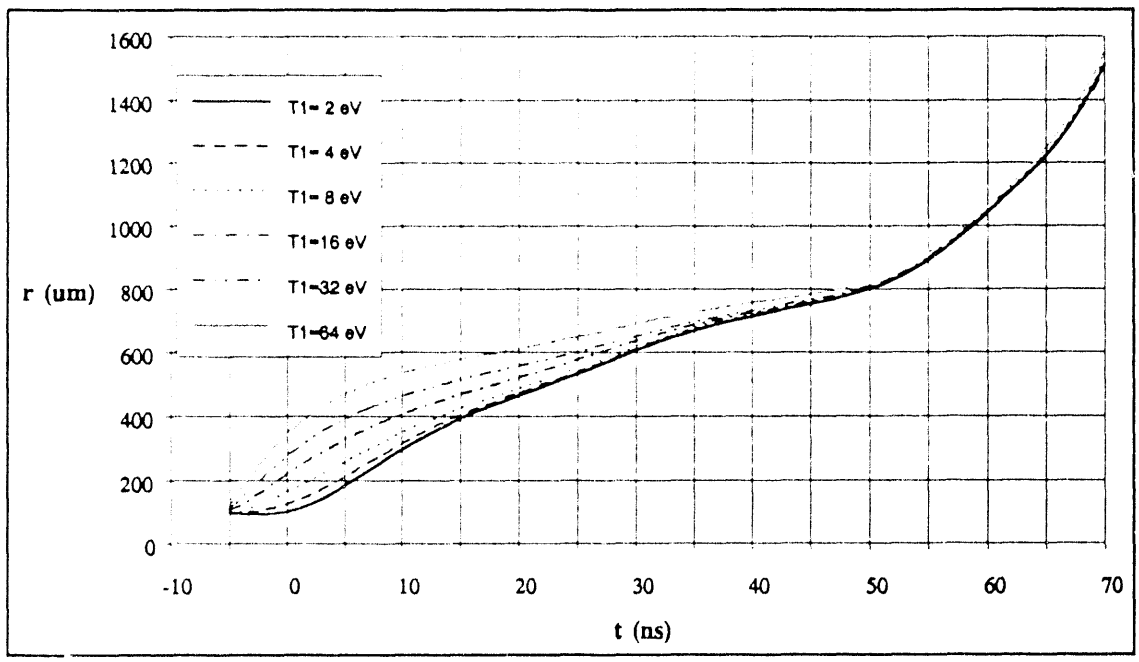

Fig. 2.5 Simulation radius vs. time plots for T_1 = 2, 4, 8, 16, and 32 eV. The starting Bennett temperature is typically T_B = 4 eV.

lower bound on the initial temperature if the column is expanding due to thermal pressure.

The plots in Fig. 2.5 show the simulated radius vs. time plots for a range of initial temperatures. The starting Bennett temperature is typically ~4 eV. The early (t < 30 ns) behavior is more sensitive to the initial temperature than to the initial velocity. The late time (t > 30 ns) behavior of the plasma does not appear to be affected by the choice of initial temperatures in this range, for the turbulently heated model.

2.3.4. Simulation Code Verification

The major components of the code used to implement this simulation were tested separately, and the entire code was tested against the Haines-Hammel curve. The Saha ionization subroutine was consistent with a code previously

developed by Dr. John Benage at Los Alamos National Laboratory over a range of densities and electron temperatures. The Bulirsch-Stoer subroutine numerically integrated simple differential equations and generated results identical to the analytic solutions.

The total simulation was run on the Haines-Hammel current waveform for a pure deuterium plasma, without turbulent heating. The input Haines-Hammel current assumed a Coulomb logarithm of 10. The radius of the plasma changed until the Coulomb logarithm of the plasma matched the value used in computing the input current.

2.4. Turbulent Heating

This section describes a turbulent heating term originated by Lovberg *et al.*[47] and independently arrived at by Rosenbluth[48]. This heating term was proposed to explain experimental observations which were not consistent with the simpler theory described to this point; this simple theory does not take into account the effects of the MHD instabilities. The experimentally observed radial expansion of the pinch is much faster than predicted by the "stable" theory. This suggested the need for an additional heating term. The stable theory assumes that the magnetic field and plasma thermal pressures are balanced in Bennett equilibrium, while the plasma is heated by Joule heating with bremsstrahlung radiative loss. For CD_2, this predicts a slight radial expansion followed by a recompression for the currents measured on HDZP-II. This prediction conflicts with the measured expansion shown in Section 4.2.

The stable theory does not include MHD instabilities that are observed at the onset of the current and continue throughout the experiment. An initial $m=0$ perturbation, as described in Section 1.4, grows at roughly the Alfvén speed v_A.

It has been assumed that the plasma current reconnects at the outer radius of the gap created when an instability "necks off."

This reconnection creates a toroid of magnetic flux trapped within the plasma that is converted into turbulent motion of the plasma, increasing the kinetic energy of particles in proportion to their mass. Turbulence delivers energy via a piston-like change in local bulk velocity. A change in average speed translates into a change in energy proportional to the mass of the particle. It is assumed that the magnetic flux toroid is converted to turbulent plasma energy in a time short compared to the time needed to create the toroid.

The magnetic Reynolds number

$$R_m = \mu_0 r v_A / \eta \approx \textit{Fluid Work / Resistive Loss} \qquad (2.32)$$

remains large enough ($\sim 10^9$,) for the plasma created in HDZP-II, to insure that the majority of the trapped magnetic energy is converted into turbulent heating rather than resistive heating.

This additional heating term is expressed in terms of a resistance as

$$P_{Turb} \equiv I\frac{d}{dt}(LI) \approx I^2\frac{d}{dt}L = I^2 R_{Turb} \quad (W) \quad , \qquad (2.33)$$

where L is the inductance of a pinch of length ℓ;

$$R_{Turb} \equiv \frac{d}{dt}L = \frac{d}{dt}\frac{\mu_0 \ell}{2\pi}\ln\left(\frac{R}{r}\right) = -\frac{\mu_0 \ell}{2\pi}\frac{v_r}{r} = \frac{\mu_0^{3/2}\ell I}{4\pi^2 r^2\sqrt{\rho}} \quad (\Omega) \; . \qquad (2.34)$$

This is based on the assumption that the instability contracts toward the axis at the local Alfvén speed and that the expansion at other axial positions associated with the instability growth is negligible. The Alfvén speed and the radius are

approximated as those of the unperturbed pinch for computing the turbulent heating power in the simulation.

III EXPERIMENT

This chapter describes the apparatus used to produce the fiber z pinch and to observe the resulting plasma. The current generator, vacuum load chamber and diagnostics will be described.

3.1. HDZP-II Current Generator

The High Density Z-Pinch II (HDZP-II) current generator, as shown in Fig. 3.1, can deliver a peak current of ~700 kA with a rise time of 100 ns through an inductive load. The major components of the experiment are the Marx capacitor bank, the pulse compression network, and the load chamber. The pulse compression network includes the intermediate store, the gas switch, the vertical line and the water switch. The Marx bank and the gas switch were copied from

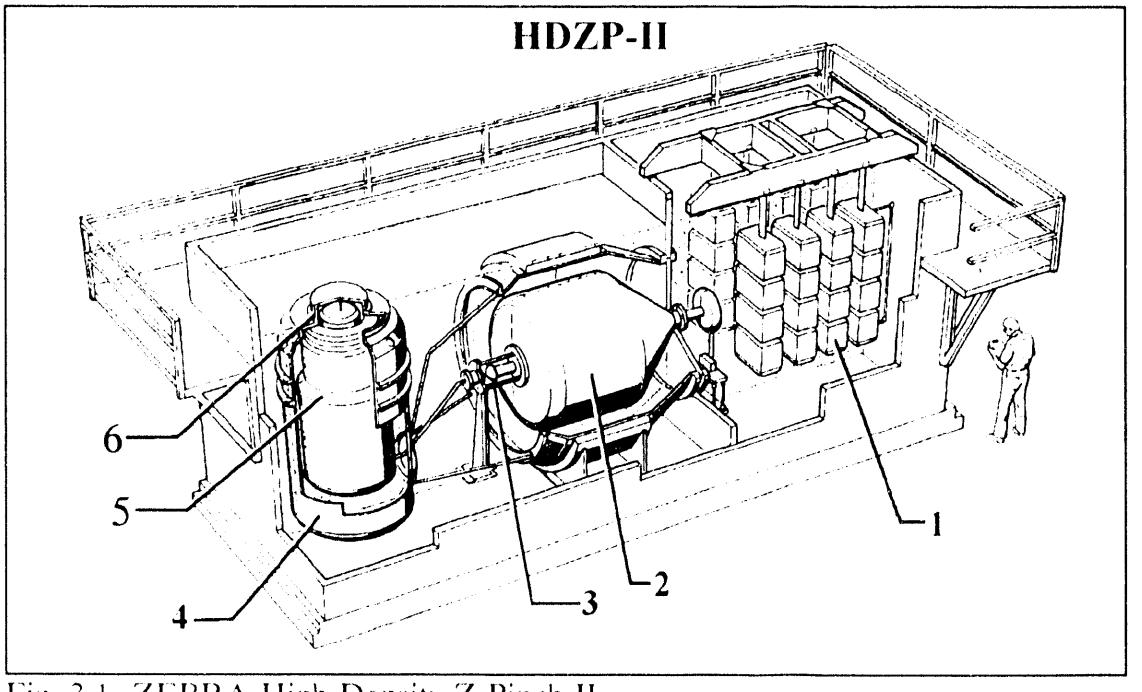

Fig. 3.1 ZEBRA High Density Z-Pinch II.

Major components: (1) Marx capacitor bank in oil, (2) intermediate energy store in water bath, (3) SF_6 gas switch, (4) vertical water transmission line, (5) water switch, and (6) vacuum load chamber.

the SATURN experiment at Sandia National Laboratory. Sandia was also helpful in the design of the rest of the pulsed power system.

The Marx Bank consists of thirty-two 1.3 μF capacitors in an oil tank. The bank can be charged to a maximum voltage of 100 kV, resulting in a bank energy of 200 kJ. This bank is charged in parallel for approximately one minute. When the bank is triggered, the capacitors discharge in series through spark-gap switches into the intermediate store transfer line in ~1 μs, applying a voltage of up to 3.2 MV across the transfer line.

The first section of the pulse compression network, the transfer line, is a water dielectric capacitor in a bath of deionized water. A rimfire SF_6 gas switch self-closes when the voltage in the transfer line reaches a limit set by the pressure of the SF_6 gas in the switch. The energy is then transferred into a vertical water transmission line in ~250 ns. When the voltage in the vertical line reaches a limit, the water self-switch closes and the energy is delivered to the vacuum load chamber, completing the pulse compression.

The water switch consists of a set of eight pairs of pins in a circular array. When the voltage across the switch is high enough, current will arc across the pairs of pins. The separation of the pins is set to determine the closing time of the switch. A plate was inserted into the switch, with suitable cutouts at the pin pairs, to reduce current prepulses due to capacitive-feedthrough.

A graded insulator stack of alternating Teflon and stainless-steel rings insulates the inner and outer conductors at the vacuum-water interface. The metal rings serve to smooth out the electric field near the load chamber.

The voltage is applied to a solid fiber within the load chamber. The voltage breaks down the fiber providing a channel for the current that rises to ~700 kA with a rise time of ~100 ns.

3.2. Load Chamber

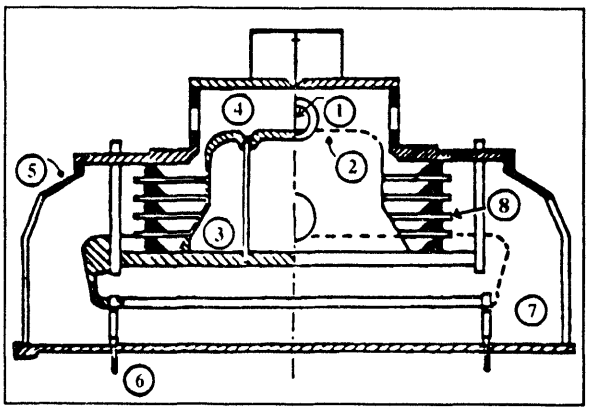

Fig. 3.2 Load chamber.
(1) fiber, (2) cathode, (3) inner conductor, (4) vacuum, (5) outer conductor, (6) water-switch pin, (7) water, and (8) vacuum insulator.

The load chamber, as shown in Fig. 3.2, is located on top of the vertical transmission line. This facilitates loading fibers vertically. The fiber loads are too flexible to be inserted horizontally. The solid fibers are composed of deuterated polyethylene, CD_2. The threads were drawn from a solution of CD_2 in xylene. After they were dry, these threads were cut into fibers of the proper length. Each fiber was mounted on a screw with a small weight to keep it straight. The weight was lowered through holes in the electrodes and left dangling below the surface of the cathode. The screw was secured within the vacuum chamber above the anode. The vacuum within the chamber was typically on the order of 10^{-6} torr at the time of the shots.

3.3. Diagnostics

The diagnostics on this experiment include the voltage and current probes required for monitoring the electrical power delivered to the load. The plasma is optically imaged by two cameras when illuminated by a single laser. Narrow bands of the plasma's x-ray spectrum are collected by a three-channel spectrometer to find the volume-averaged electron temperature of the plasma as a function of time. The neutron yield is recorded by a silver activation counter.

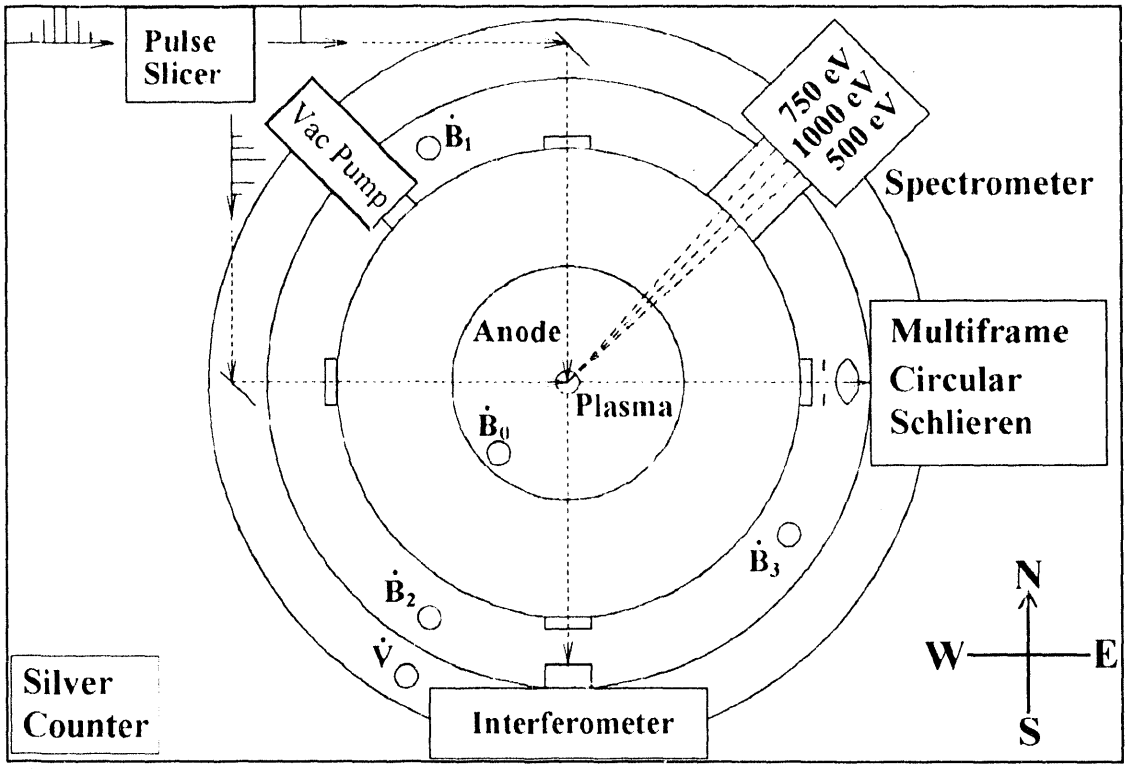

Fig. 3.3 Top-down view of diagnostic placement.
The optical paths of the interferometer and the circular schlieren pass through the same volume of plasma along orthogonal lines. The primary B-dot probes are separated by ~120° around the load. The voltage probe is located near B-dot probe 2 at a larger radius. The x-ray spectrometer and silver activation counter diagnostics are located NE and SW of the load chamber.

These diagnostics are deployed around the load chamber as shown in Fig. 3.3.

The high field and energy densities in the region of the plasma place constraints on the types of diagnostics that may be used. Physical probes are ruled out, so one is limited to x-ray and fusion product emissions and optical probes. The short duration of the plasma (~150 ns) requires that the imaging diagnostics use a very short exposure time (< 1 ns) to prevent smearing of the image by the radial expansion (~30 km/s) of sections of the plasma.

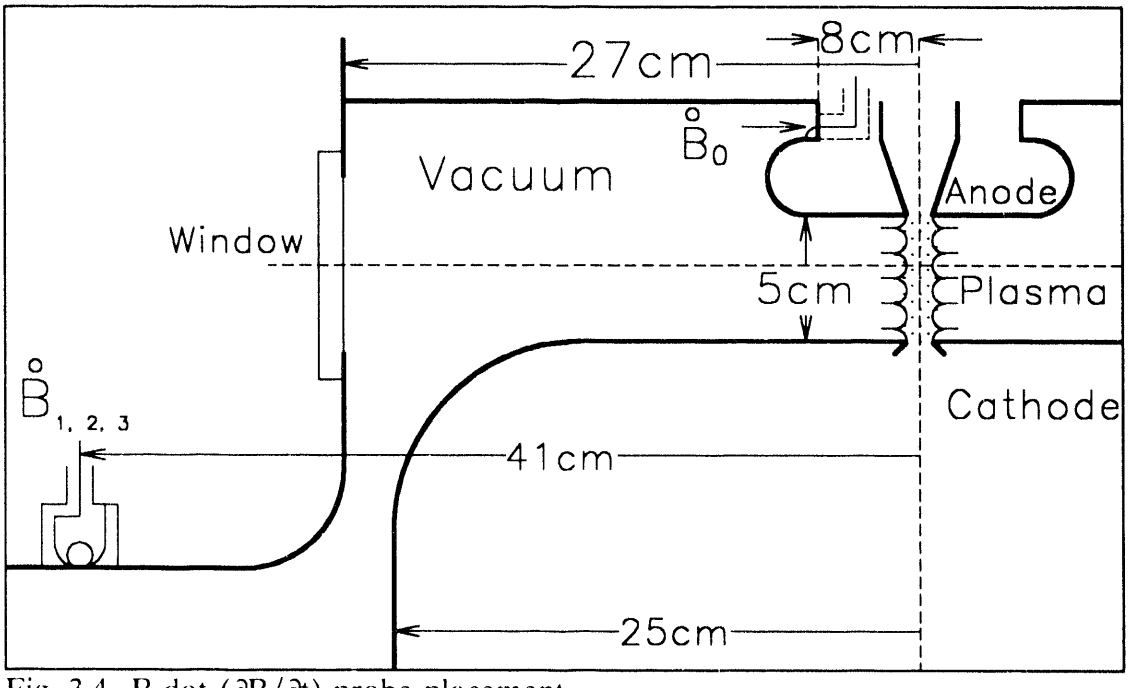

Fig. 3.4 B-dot (∂B/∂t) probe placement.
Probes B_1, B_2, and B_3, are distributed around the load at a radius of 406 mm, separated by ~120° and B_0 is above the anode plate at a radius of 82.6 mm.

3.3.1. Electrical Diagnostics

The current through the load chamber was measured by B-dot (∂B/∂t) loop probes, $\dot{B}_1$, $\dot{B}_2$, and $\dot{B}_3$, placed at a radius of 406 mm and separated by ~120°, as shown in Fig. 3.3. These probes are within the radius of the vacuum insulator. To verify that the current flowed through the plasma rather than shorting out the magnetically insulated transmission line (MITL), an additional B-dot probe, $\dot{B}_0$, was added to the top of the anode plate as shown in Fig. 3.4. This probe was at a radius of 82.6 mm. The anode plate blocked the probe from direct radiation from the plasma, reducing the possibility that the surface of the probe would "flash over." This probe's readings proved to be consistent with the average of the other

B-dot probes until ~120 ns into the current when its signal clamped to zero. This is probably due to the probe flashing over, which excludes the magnetic field from its sensing loop. The B-dot signals were recorded on a digital oscilloscope and integrated numerically to provide a record of the current in the load.

The current waveforms input to the simulation described in the next chapter were usually recorded from the $\dot{B}_0$ probe. If this probe flashed over too early to provide a useful signal, the average of the other three probes was used.

The voltage probe capacitively measures the voltage across the transmission line feed at the load chamber at a radius of 508 mm. Because this probe is in the water it must be calibrated while the water tank is full to provide the same capacitance as during a shot.

The voltage probe and the B-dot probes were calibrated by shorting out the water switch in the vertical line and attaching a high-voltage, fast pulser to the bottom of the vertical line. The load was replaced by a cylindrical array of resistors whose resistance matched the impedance of the transmission line. The calibration pulse was measured with a current-viewing precision resistor at the load. Scale factors were then computed for each of the B-dot probes and for the voltage probe by comparing their outputs with the known current and voltage of the pulse.

3.3.2. Nd:YAG Diagnostic Laser

An interferometer and a multiframe circular schlieren use light from a single Nd:YAG laser. The laser is mode-locked to provide pulses of width ~100 ps every 10 ns. The laser is also Q-switched to produce a comb of about twenty bright mode-locked pulses, as shown in Fig. 3.5.

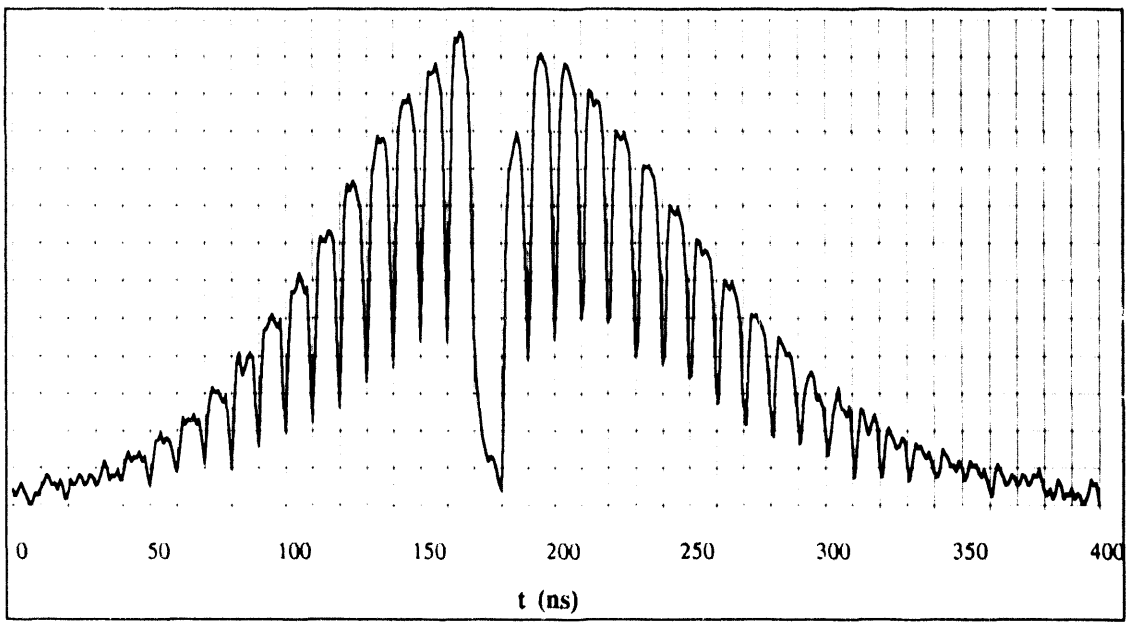

Fig. 3.5 Laser pickoff PIN diode signal for shot 411.
Signal shows a Q-switched comb of mode-locked pulses with period $\Delta t = 10$ ns. The pulse at 170 ns was sliced out.

A PIN diode detector records the fraction of the laser output which is removed from the beam by a reflection from a lens used to expand the beam for transport to the diagnostics. The PIN diode takes almost 10 ns to output the charge pairs created by the 100-ps laser pulses, and does not measure the width of individual pulses; this gives a measure of the maximum frequency response of the detector-oscilloscope pair. This detector is identical to those used in the x-ray spectrometer described in Section 3.3.6.6. The pulses arrive at the detector at the times when the signal suddenly increases. One of these pulses is sliced out by a Pockels cell, amplified, frequency doubled, and delivered to the interferometer. The remaining pulses in the comb are routed to the multiframe circular schlieren.

3.3.2.1. Pulse Slicer

The pulse slicer is a Pockels cell that rotates the vertical polarization of the lasers beam 90° so that it is reflected by a thin-film multilayer (TFML) polarizer. The Pockels cell changes the polarization of the laser beam in ~1 ns, holds for 10 ns, then switches it back in ~1 ns. The TFML, which is transparent to vertically polarized light, reflects most of the horizontally polarized light into the path that leads to the interferometer. The Pockels cell is open long enough to divert one pulse, and on occasion half of two pulses. The timing of the sliced pulse relative to the triggering of the Pockels cell has an inherent 5-ns jitter because there is no synchronization between the mode locker and the Pockels cell trigger. Although this delay cannot be set to better than 5-ns precision, the timing of this pulse is recorded by a laser pickoff to within ~1 ns, as shown in Fig. 3.5. The pickoff recorded at 1 giga-samples per second shows the sudden increase in signal voltage for the sample taken at the time that the laser pulse strikes the detector.

The infrared (IR) (1.064 μm) light produced by the laser is frequency doubled to visible, green (λ=532 nm) light, and the remaining IR is filtered out before the light is imaged by the diagnostics. The use of visible light expedites the alignment of the diagnostics, improves the safety for the operator, and permits diagnosis of plasmas at four times the density that can be diagnosed by the original IR.

Light of a frequency below the plasma's electron frequency[50],

$$\omega_{pe} = \sqrt{\frac{n_e e^2}{\epsilon_0 m_e}} \approx 56.4\sqrt{n_e} \quad (rad/s) \quad , \tag{3.1}$$

is reflected, defining a cutoff density for a given wavelength of light as

$$n_{crit} = \frac{\epsilon_0 m_e}{e^2}\left(\frac{2\pi c}{\lambda}\right)^2 \approx 1.11\times 10^{15}\,\lambda^{-2} \quad (m^{-3}) \quad . \tag{3.2}$$

The green light used to probe the plasma $\lambda = 532$ nm has a plasma cutoff density of $n_{crit} = 4\times 10^{27}$ m^{-3}. This light can penetrate a plasma created from a solid deuterium $n_e = 5\times 10^{28}$ m^{-3} fiber that has become fully ionized and uniformly expanded in radius by a factor of $r/r_0 \approx 4$.

A fully ionized CD_2 plasma will have particle densities

$$n \equiv n_C = \frac{n_D}{2} = \frac{n_e}{8} \quad (m^{-3}) \ , \tag{3.3}$$

and solid CD_2 has carbon number density $n_{CD2} = 3.7\times 10^{28}$ m^{-3}. A fully ionized CD_2 plasma must expand by $r/r_0 \approx 10$ to be transparent at this wavelength. At higher densities, the light cannot propagate and is rejected from the image for reasons that do not depend on density gradients.

3.3.3. Laser and Diagnostic Triggering

The Q-switch is triggered by a fixed delay relative to the trigger for the Marx bank. Although the electro-optic Q-switch opens ~1 ns after being triggered, it takes ~300 ns for the mode-locked pulse to build up to peak brightness within the laser. There is jitter of ~50 ns in the delay between the triggering of the Marx bank and the beginning of the main current in the load. Despite this jitter, the eight bright pulses needed by the multiframe circular schlieren can be selected from the twenty available bright pulses in the comb.

The pulse slicer and the sweep of the streak camera used in the multiframe circular schlieren are triggered by a fixed delay relative to the closing of the SF_6 gas switch in order to avoid the jitter in the Marx bank. A fiber optic cable near the gas switch catches some of the light produced when the switch begins to

conduct. The fiber optic leads to a trigger box that issues an electrical signal to trigger the sweep of the streak camera and to trigger the pulse slicer. The delay relative to this signal is set by varying the length of the cable from the trigger box to the triggered device.

The current starts in the load ~300 ns after the gas switch closes, with a 20-ns jitter. This allows enough time to send a signal from the gas switch to the pulse slicer and for the light at the pulse slicer to propagate to the load before the main current starts.

3.3.4. Point-Diffraction Interferometer

As shown in Fig. 3.6, a "point-diffraction" interferometer splits the laser beam into two legs after it passes through the plasma. The advantages of point-diffraction interferometry are described in Section 3.3.4.2. A collimated laser beam illuminates a refractive object, and a lens collects the light. The light is then split into two legs. One leg is spatially filtered with a pinhole aperture and becomes the reference leg of the interferometer. The other leg, called the "scene" leg, has some neutral density filtering to match its brightness to that of the

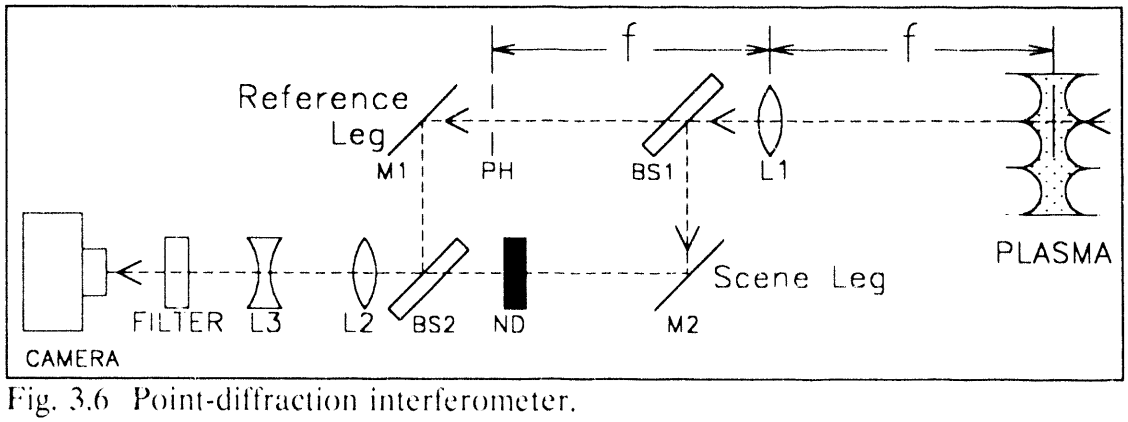

Fig. 3.6 Point-diffraction interferometer.
Plasma backlit by laser beam which is split into two legs, one of which is filtered to form a reference leg and then recombined to interfere with the scene leg.

reference leg for better fringe contrast. The two legs are then recombined to form an interferogram, which is imaged by a camera. The interferometer measures the electron density integrated along the scene beam. The fringes of the interferograms can be integrated to infer the electron line density; if axi-symmetry can be assumed, the density as a function of radial and axial position can also be derived from the fringes by Abel inversion.

3.3.4.1. Detailed Description of the Interferometer

The light enters the interferometer at lens L_1 with an aperture radius of 38 mm at one focal length (f = 45 cm) from the plasma. Light from a point source at the object plane of the plasma will be collimated; this makes imaging of the "scene" leg insensitive to the position of the second lens, with the same focal length. Using two lenses of the same focal length separated by twice the focal length provides a magnification of 1 for both legs. The portion of the collimated laser beam not perturbed by the plasma will come to a focus at one focal length past the first lens (L_1). A 50% dielectric beam splitter (BS_1) is placed shortly after the first lens to allow room to mount a filter at the focus of the lens in one of the paths. The leg that passes through the beam splitter is filtered by a 50-μm pinhole aperture (PH) placed at the focal point, creating a reference leg. The light from the scene leg is reduced by a neutral density filter ($ND \approx 1$) to match the expected brightness of the reference leg, improving the fringe contrast of the final image.

The two legs are reflected by aluminum mirrors (M_1 and M_2) and recombined by a second dielectric beam splitter (BS_2.) The combination of the two legs passes through the second lens (L_2.) This lens is placed at one focal length beyond the pinhole filter to recollimate the reference leg and image the scene leg. The image is formed one focal length beyond the second lens with

magnification 1. The light is filtered with a laser-line filter and a polarizer to reduce the image of light emitted by the plasma. The image is collected by a CCD camera, which integrates the image for 1/6 s and sends a video frame to a frame-grabber board in an IBM PC that saves the digital image in a file. The exposure of the camera is set with neutral density filters ($ND \approx 2.$) The magnification can be changed by adding a third lens (L_3) between the second lens and the camera.

3.3.4.2. Point-Diffraction vs. Mach-Zehnder

The point-diffraction interferometer has some advantages over the commonly used Mach-Zehnder interferometer. The principal advantage of the point-diffraction interferometer is that the beam is not split until after it has illuminated the plasma. All of the optics in the interferometer can be mounted on one small, rigid platform. This allows the optics to be better protected from mechanical damage and desteering. The alignment is simplified by having all of the adjustments near each other. It is also easier to adjust the lengths for the two legs to be equal, which is required for laser pulses with short coherence lengths. The point-diffraction interferometer has long been used for testing optical components. Recently it has been applied to imaging large wind-tunnel flow fields[51].

This interferometer works well for the parameters of HDZP-II. But, if the object occupies too much of the input laser beam, then most of the light will be filtered out of the reference leg and the fringe contrast will be poor. It is possible to compensate by putting more neutral density in the scene leg if the filtered intensity is predictable and if the laser is bright enough.

3.3.4.3. Physics of Interferometry

Light traveling through plasma will have its phase advanced by

$$\phi = \frac{2\pi}{\lambda} \int dx(1-\mu_r) \approx \lambda r_e \int dx\, n_e \quad (rad) \quad , \tag{3.4}$$

where n_e is the electron density, the integral is along the path of the light ray, the index of refraction of the plasma is approximately[52]

$$\mu_r \approx \sqrt{1 - \frac{\omega_p^2}{\omega^2}} \approx \sqrt{1 - \frac{4\pi r_e c^2}{\omega^2} n_e} \approx 1 - \frac{2\pi r_e c^2}{\omega^2} n_e \quad , \tag{3.5}$$

and the classical electron radius is defined as

$$r_e \equiv \frac{e^2}{4\pi \epsilon_0 m_e c^2} \approx 2.818 \times 10^{-15} \quad m \ . \tag{3.6}$$

When this light interferes with the reference leg, the fringes will shift in proportion to the amount of plasma the light has gone through.

The line density can then be computed by integrating the fringe shifts along a line (on the image) normal to the z axis which is collinear with the pinch axis

$$N_e(z) \equiv \int_{-\infty}^{\infty} dy \int_{-\infty}^{\infty} dx\, n_e \approx \frac{1}{\lambda\, r_e} \int_{-\infty}^{\infty} dy\, \phi \quad (m^{-1}) \tag{3.7}$$

without making any assumptions about axi-symmetry.

In practice, one of the mirrors is tilted slightly to produce horizontal background fringes (perpendicular to the z axis.) This simplifies counting fringe shifts. A reference image is taken to record these background fringes about five minutes before applying voltage to the fiber. The reference image also provides the initial position of CD_2 fibers. The fringe shifts in a plasma interferogram

relative to this reference are then counted along lines normal to the axis and integrated to compute the line density.

The integral defining the fringe shifts in polar coordinates

$$\phi \approx \lambda r_e \int dx\, n_e = \frac{\lambda\, r_e}{2} \int_y^{r_0} \frac{dr\, r\, n_e}{\sqrt{r^2 - y^2}} \quad (rad) \tag{3.8}$$

can be inverted by a transform called "Abel inversion"[53]

$$g(y) \equiv \int_y^{r_0} \frac{dr\, r\, f(r)}{\sqrt{r^2 - y^2}} \quad \Rightarrow \quad f(r) = -\frac{2}{\pi} \int_r^{r_0} \frac{dy}{\sqrt{y^2 - r^2}} \frac{\partial g(y)}{\partial y} \tag{3.9}$$

assuming axi-symmetry, to produce the electron density as a function of radial and axial position

$$n_e(r,z) \approx -\frac{\pi}{\lambda r_e} \int_r^{r_0} \frac{dy}{\sqrt{y^2 - r^2}} \frac{\partial \phi(y,z)}{\partial y} \quad (m^{-3}) \,. \tag{3.10}$$

All of the interferograms taken are symmetric enough about the axis of the pinch to assume axi-symmetry. The fringe-shift data taken along a line normal to the z axis for the line density calculation, described above, is fit by a cubic spline. The partial derivative of this fit is then integrated to provide the density as a function of r and z according to Eq. (3.10).

3.3.5. Multiframe Circular-Schlieren Diagnostic

The multiframe circular schlieren, as shown in Fig. 3.7, collects a series of up to eight circular schlieren images on an **Imacon 790** fast streak camera, made by Hadland Photonics. The circular-schlieren diagnostic will be described below in Section 3.3.5.1. The short duration of the mode-locked pulses (~100 ps)

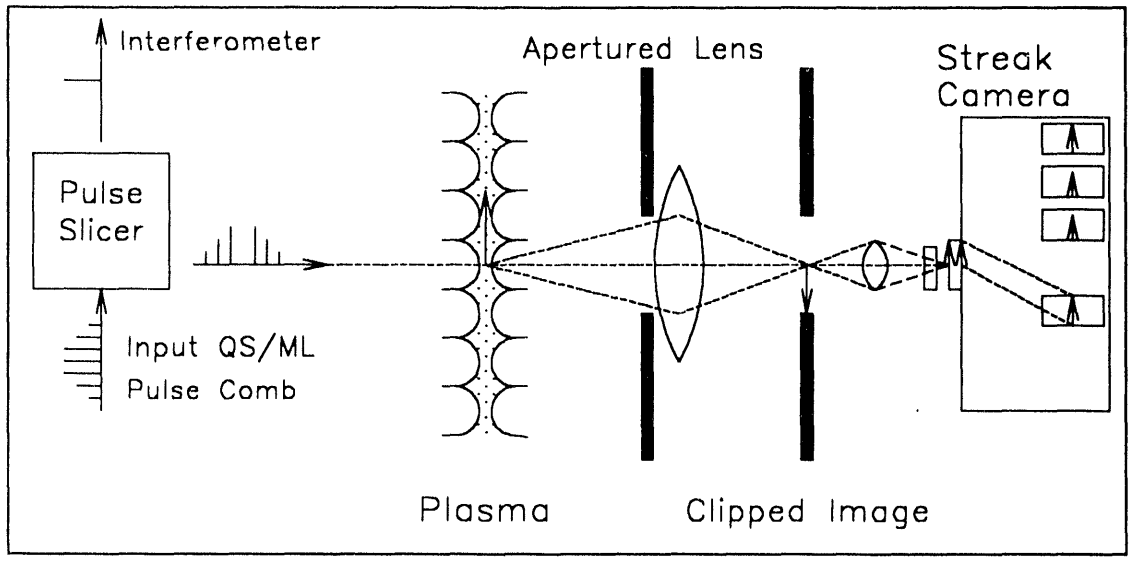

Fig. 3.7 Multiframe circular-schlieren diagnostic setup.
The backlit plasma is imaged by an apertured lens. The image is clipped and relayed to the input of a streak camera.

produces a result similar to a very fast framing camera. The light collected on the front of the streak camera is converted to a stream of electrons, which preserves the image as it is swept across the output phosphor screen at ~1 mm/ns and is recorded on film. The period between mode-locked pulses of 10 ns limits the width of a circular-schlieren image on the film to 10 mm. A rectangular aperture was placed at the input image plane of the camera to limit the width of the images on the film to 10 mm, restricting the overlap of images produced by successive pulses. The available width of 70 mm of the output phosphor screen imposes a limit of seven full frames on the film.

The mode-locked laser is Q-switched to increase the brightness of the pulses and, more importantly, to act as a fast shutter on the laser output. All light collected by the streak camera is integrated continuously on the left side of the phosphor screen until the image begins to sweep. This bright area is labeled as F0 at the left side of Fig. 3.8. More than 100 mode-locked pulses will cause this

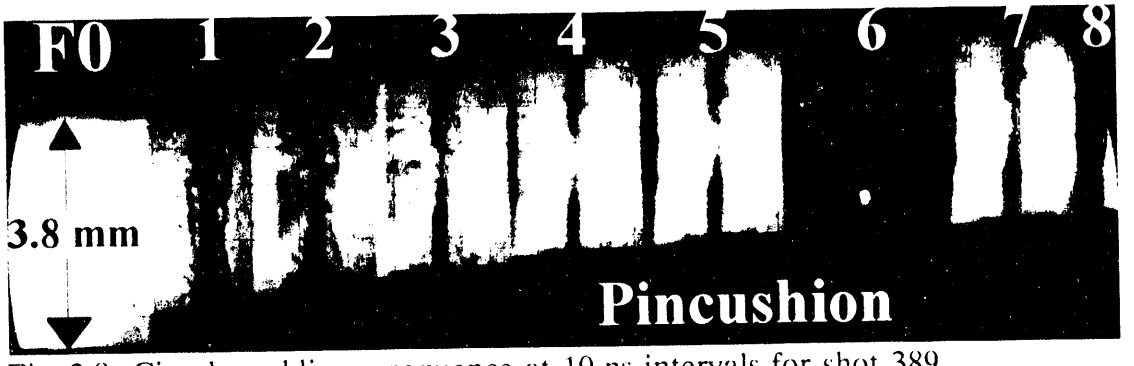

Fig. 3.8 Circular-schlieren sequence at 10-ns intervals for shot 389. Frame 5 shows pincushion distortion due to overexposure. The increasing overexposure of the frames give the false impression that the plasma is contracting in this reproduction. The first frame is exposed well enough to see a plasma column with a dense core.

patch to "bloom" over the entire film surface, washing out the circular-schlieren images. The Q-switch produces a comb of about twenty bright pulses with pulse energy falling off quickly outside this window. If this bright area (frame 0) could be shifted off the edge of the phosphor, by changing the initial steering voltage, or if the mode-locked comb were gated more accurately, this bloom would be less of a problem and the first 10 mm of the phosphor screen would be available for imaging another frame.

Background room light and light emitted by the plasma are reduced by using neutral density filters and a line filter which passes only a narrow band around the wavelength of the laser. The amount of neutral density used ($ND \approx 2$) is chosen just before each shot to give the best exposure. The circular-schlieren images in Fig. 3.8 show the pincushion distortion produced when the streak camera is overexposed. Different shifts between the frames are due to variations in the streak rate of the camera. The 10-ns delay between images is dictated by the mode-lock period of the laser used and is very consistent frame to frame and shot to shot.

One of the mode-locked pulses is sliced out of the Q-switch pulse train and redirected to the interferometer diagnostic. This results in one dimly lit circular-schlieren frame that in some cases is too faint to provide the shape of the plasma, as can be seen in frame 6 of Fig. 3.8. This does however provide a reliable timing fiducial. The time of the selected pulse is contained in the laser pickoff signal, as shown in Fig. 3.5.

There is a 3-ns shift in time between the two diagnostics due to the difference in their optical paths and is constant from shot to shot. This delay was calibrated by imaging a solid fiber on the multiframe circular schlieren. The neutral density filters normally placed at the image plane of the streak camera were placed in the optical path of the laser before it backlit the fiber. This made the image of the glint of the pulse, directed orthogonally through the interferometer, as bright as the backlit image. This resulted in a series of backlit shadow images with one shadow image replaced by a sidelit image of the fiber. The relative delay was measured from the shift between the position of the sidelit image and the backlit image that it replaced.

3.3.5.1. Physics of Circular Schlieren

"Circular schlieren" is a diagnostic technique very similar to "knife-edge" schlieren[54,55]. This technique is referred to as "circular" because it rejects light refracted outside a circular cone defined by the aperture of an imaging lens. A knife-edge schlieren which rejects light refracted below a knife edge placed near the focal point of an imaging lens.

As shown in Fig. 3.9, the circular-schlieren diagnostic consists of a lens of focal length f_1 = 200 mm and input aperture r_{Ap} = 6.35 mm at o_1 = 381 mm from the backlit plasma forming an image at i_1 = 421.6 mm from the lens. This image is at o_2 = 40.6 mm from a second lens f_2 = 25 mm forming a second image at

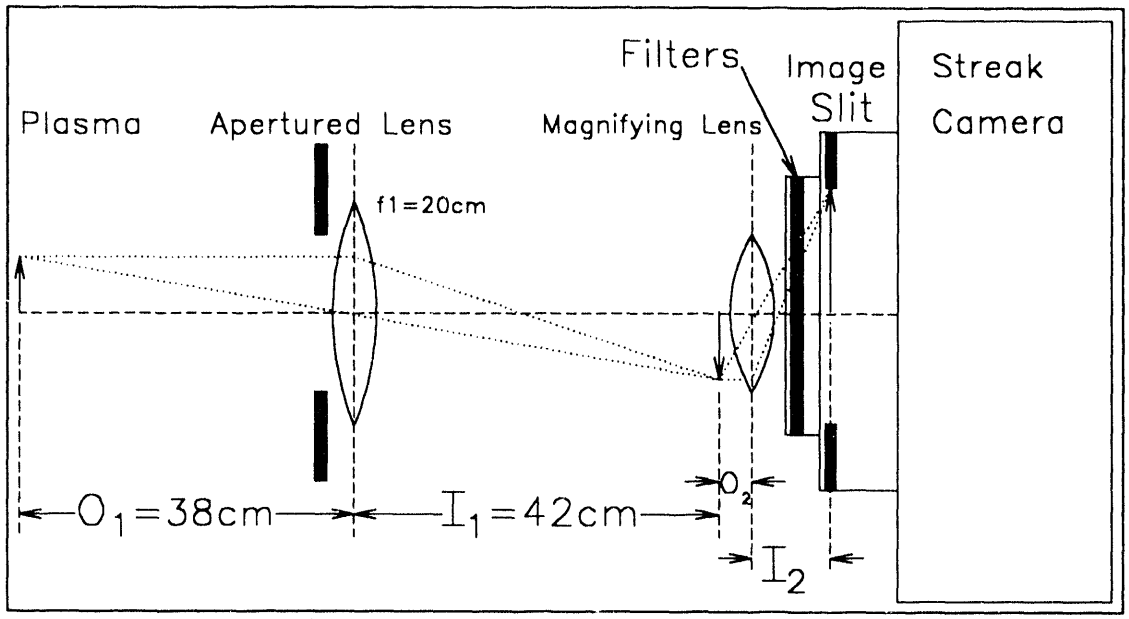

Fig. 3.9 Circular-schlieren diagnostic dimensions.
A lens (f_1 = 200 mm, r_{Ap} = 6.35 mm) at o_1 = 381 mm from the plasma images at i_1 = 421.6 mm, o_2 = 40.6 mm from a second lens (f_2 = 25 mm) forming an image at i_2 = 81.3 mm.

i_2 = 81.3 mm within the image-clipping slit at the input of the streak camera. These two lenses magnify the plasma's image by a factor of ~2.3, and there is an additional magnification in the streak camera of ~2 between the image slit and the film, giving a total magnification of ~4.5. The streak camera used could not resolve the fringes of an interferogram at this wavelength; this is why the camera was used to collect circular-schlieren images.

3.3.5.1.1. Refraction of Light by Pinch

Only those rays that pass through the imaged area and are refracted by the plasma at an angle less than 16 mrad (≈arctan(6.4/381)) are collected by the first lens and imaged by the camera. The edge of the frame at ~ 2 mm from the center of the imaged area must satisfy an even tighter constraint of 12 mrad

(≈arctan((6.4-2)/381)). A smaller lens aperture will reduce the width of this acceptance angle over the imaged area to the point of making alignment very difficult and image quality poor. A larger aperture will require higher density gradients to refract the light out of the aperture.

The angle that a light ray is bent by traveling through a medium with varying refractive index is given as[56]

$$\phi = \int ds \frac{\nabla_\perp \mu_r}{\mu_r} \approx \int ds \frac{\nabla_\perp n_e}{2n_e - \frac{\omega^2}{2\pi r_e c^2}} \approx -\frac{2\pi r_e c^2}{\omega^2} \int ds \nabla_\perp n_e \quad , \qquad (3.11)$$

where the integral is along the optical path ds, $\nabla_\perp n \equiv |\hat{s} \times (\vec{\nabla} n)|$ is the magnitude of the gradient normal to the optical path, and the refractive index is related to the electron density according to Eq. (3.5).

Ideally, the image is a bright uniform background with a dark silhouette of the plasma. However, diffuse uniform "halo" plasmas are almost invisible to this diagnostic. Circular schlieren is quite sensitive to the tenuous, axially nonuniform, radial jets of plasma called "spicules." The low density of spicules cause almost undetectable shifts in interferometer fringes. Despite the low density, the sharp edges of spicules produce gradients in the local electron density that are easily detected by circular schlieren. The strong gradients of the electron density scatter the light out of the aperture leaving a shadow on the image.

A cylinder of constant radius and uniform density, like a glass rod, will not bend a ray that travels through the axis of the cylinder. For a finite lens aperture, there will be a bright area imaged within the shadow of the more refractive edges of the cylinder, as described in Fig. 3.10. This clear band can be obscured if the electron density in the core of the plasma is above the cutoff ($n_{crit} = 4 \times 10^{27}$ m^{-3})

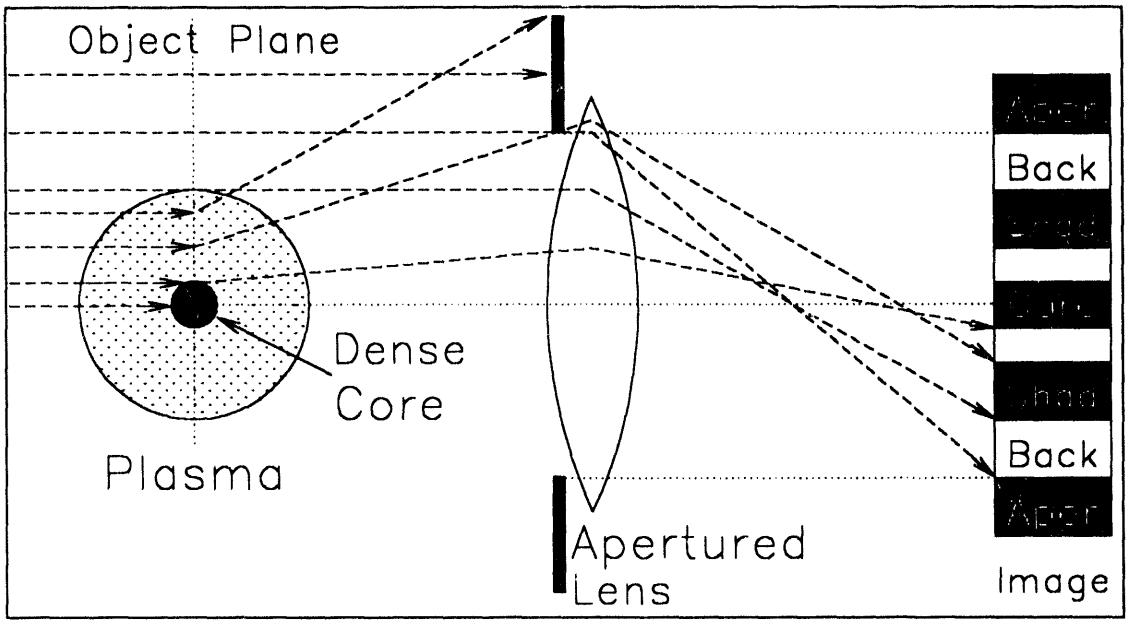

Fig. 3.10 Circular-schlieren of a plasma column with a dense core. The dense core casts a shadow in the center of the column. Light that passes near the edge of the plasma is refracted out of the aperture of the imaging lens.

for the wavelength of light (λ = 532 nm.)

The only circular-schlieren images observed with clear interiors are of plasmas produced by prepulse currents. The first frame of Fig. 3.8 shows the narrow dark outline of the cool plasma, a dark higher density core, and a transparent region in between.

3.3.5.2. Magnification Selection and Calibration

The magnification of the circular schlieren was chosen to facilitate measuring a radius of the plasma from the circular-schlieren images. The later frames in Fig. 3.11 show how the image of the plasma breaks up into disconnected blobs when the plasma expands much beyond a radius of 1 mm, for the lens aperture chosen and the range of line densities. Although the plasma continues to expand rapidly, measuring radii above 1 mm becomes so speculative as to be

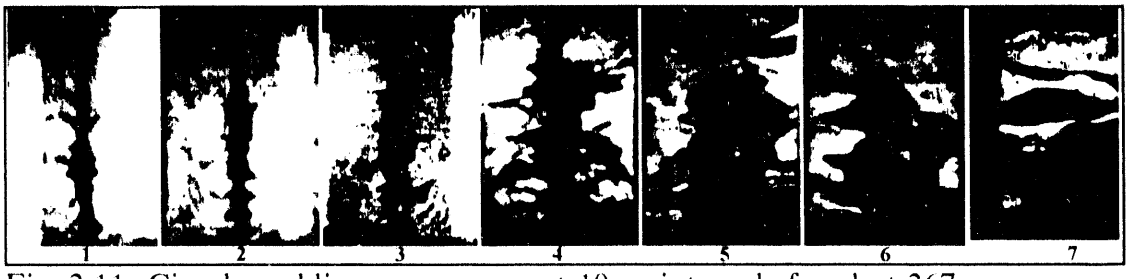

Fig. 3.11 Circular-schlieren sequence at 10-ns intervals for shot 367. Each frame is 2.4 mm wide. The plasma has expanded so much in the last frame that its radius cannot be measured.

of little value. Imaging a width of about 2.4 mm of the plasma allows for measuring the radius of an irregularly shaped shadow up to this threshold. The 10-mm limit on the width of the image then specifies the magnification.

The magnification of the circular-schlieren system was calibrated by imaging q drill rod of diameter 1.6 mm. This magnification was ~4.54 between the rod and its image on the film. The circular-schlieren frame images an area of the plasma 3.8 mm tall and 2.4 mm wide. The height of the image is limited by the active area of the streak camera.

3.3.6. X-Ray Spectrometer

The x rays emitted by the pinch plasma in three narrow energy bands are collected by channels of a spectrometer to measure the volume-averaged electron temperature of the plasma as a function of time. The plasma emits free-bound and bremsstrahlung radiation as described in Section 2.2. Each of the three channels of the spectrometer collects x rays in a different narrow energy band from the same volume of plasma, at a slightly different angle in the plane normal to the pinch axis. The electron temperature is computed from the slope of the spectrum provided by the ratio of the measured signals of either two of the three channels. The redundancy of ratios provides a check of the temperatures inferred

from this diagnostic. This section describes the x-ray spectrum emitted, how narrow energy bands are selected from this continuous spectrum, how filters attenuate the x rays, and how the electron temperature is computed from the signals produced by the detectors exposed to these collimated, filtered x rays.

The three spectrometer channel energies were originally selected to be 1, 2, and 3 keV, but the signals were too weak to provide any usable temperature measurement. The channel energies were then changed to 500, 750 and 1000 eV. Parameters are given in this chapter for all five energies, but only data from 500, 750 and 1000 eV are presented in the next chapter.

3.3.6.1. CD_2 Plasma X-Ray Source

The highest-energy radiation line of a CD_2 plasma arises from free electrons being captured to the lowest energy state of formerly fully ionized carbon ions. This is the ionization potential of hydrogen-like carbon ions C^{+5}:

$$E_{Cmax} \equiv \hbar \omega_{Cmax} / e = Z^2 R_y = 490 \ \ eV \ , \tag{3.12}$$

where $Z_A = 6$ is the atomic number of carbon, and the Rydberg constant is defined as

$$R_y \equiv \frac{e^4 m_e}{8 \epsilon_0^2 h^2} \approx 13.6 \ eV \ , \tag{3.13}$$

By limiting the spectrometer to photon energies above this energy E_{Cmax}, all radiation lines from impurities with $Z_A \leq 6$ are excluded, and only bremsstrahlung and free-bound radiation are collected. This assumes that contamination of the plasma by higher Z_A impurities is negligible.

The blackbody clipping of the emitted bremsstrahlung-recombination spectrum at 500 eV does not affect the electron temperatures calculated from the

TABLE II. Free-bound Gaunt factors for first six excitation states at the photon energies of the x-ray spectrometer channels.

$\hbar\omega/e$ (eV) (EV)	500	750	1000	2000	3000
G_1	0.803	0.896	0.945	0.995	0.983
G_2	1.037	1.057	1.062	1.045	1.012
G_3	1.075	1.082	1.081	1.053	1.017
G_4	0.974	1.002	1.021	1.058	1.074
G_5	1.094	1.095	1.090	1.057	1.019
G_6	1.097	1.097	1.092	1.058	1.020

x-ray signal data. The recorded signals presented in chapter 4 do not exceed the background noise until the plasma has expanded radially by a factor of greater than fifteen. At this density, the plasma is optically thin to bremsstrahlung and recombination absorption at photon energies of 500 eV and higher.

Neglecting continuum lowering, the combined bremsstrahlung and free-bound radiation spectrum was given in Section 2.2 as

$$4\pi j(\omega)d\omega = \frac{C_{Br}}{\sqrt{eT_e}} e^{-\frac{E_\omega}{T_e}} n_e \sum_i \left[Z_i^2 n_i \left(g_{Br} + \frac{Z_i^2 R_y}{T_e} \sum_k \frac{2G_k}{k^3} e^{\frac{Z_i^2 R_y}{k^2 T_e}} \right) \right] \left(\frac{W}{m^3} \right), \quad (3.14)$$

where $C_{Br} \approx 4 \times 10^{-63}$ J$^{3/2}$•m^3, i is the index over ionization states of all ions, k is the index over the excitation states, and the free-bound Gaunt factors $G_k \approx 1$ for the first six excitation states are given in TABLE II for the spectrometer energies.

Although this expression for the combined emissivity is very complicated, the ratio of emissivities at two photon energies, $\hbar\omega_1/e$ and $\hbar\omega_2/e$,

$$\frac{j(\omega_1)}{j(\omega_2)} = e^{\frac{\hbar(\omega_2 - \omega_1)}{e T_e}} \tag{3.15}$$

can be easily solved for the electron temperature. The electron temperature can then be calculated from the ratio of the spectrometer channel signals.

3.3.6.2. Detailed Description of Spectrometer Channel

The path of the x rays from the plasma to the detector is shown in Fig. 3.12. The radiation travels L_1 = 318 mm to a first sheet of lead shielding, then through a collimating hole of radius r_c = 3.2 mm. The radiation then travels a distance L_2 = 241 mm to a second sheet of lead, through a second collimating hole of the same radius (r_c = 3.2 mm) and a thin plastic blast shield. The radiation then travels ℓ_1 = 51 mm and reflects from a potassium acid-phthalate (KAP) crystal at the Bragg angle. The radiation then travels ℓ_2 = 102 mm, then through a

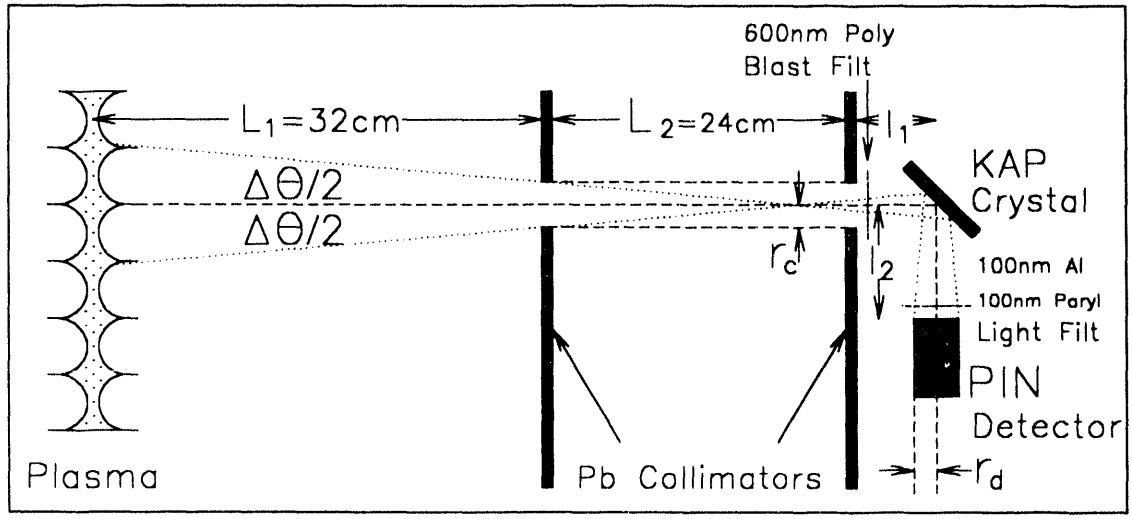

Fig. 3.12 X-ray spectrometer channel.
X rays from a volume of the plasma are collimated by two holes in lead shielding plates and are reflected at the Bragg angle into a filtered PIN diode detector.

visible-light blocking thin aluminum filter, and is finally collected by a PIN diode detector whose circular active-area has radius $r_d \approx 3.2$ mm.

This geometry defines the angular resolution of the spectrometer channel which specifies the photon energy bandwidth of the detector and the horizontal width of the solid angle over which the spectrometer collects x rays from the plasma. The angular resolution of the spectrometer channels is

$$\Delta\theta = 2 \arctan\left[\frac{r_c + r_d}{L_2 + \ell_1 + \ell_2}\right] \approx \frac{6.4\,mm + 2r_d}{394\,mm} \approx 32 \quad (mrad) \quad . \qquad (3.16)$$

Three spectrometer channels are set 50 mrad apart about the pinch axis in the plane normal to the pinch. Each channel is aligned on the same volume of plasma from a slightly different angle, with each crystal-detector pair set to measure the radiation at a different energy band.

3.3.6.3. Bragg Angle

X rays of wavelength λ ca constructively reflect from successive layers of a crystal, as shown in Fig. 3.13, if the radiation is incident at the Bragg angle θ_B

$$n\lambda = 2d \sin\theta_B \ (m) \ , \qquad (3.17)$$

where d is the distance between layers of the crystal, and n is an integer taken to be unity. The reflectance of KAP crystals is much smaller for $n > 1$.

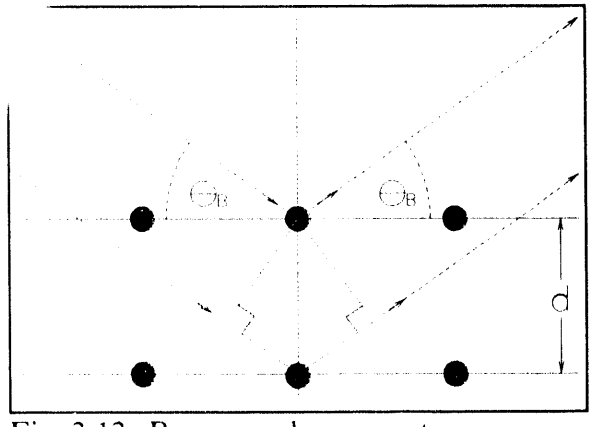

Fig. 3.13 Bragg angle geometry. Light constructively reflects from crystal planes with separation $2d$ = 26.6 Å for KAP.

The photon frequency bandwidth is related to the angular resolution of the spectrometer by the Bragg angle equation,

$$\frac{\Delta\omega}{\Delta\theta} = -\frac{2d\omega^2}{2\pi c}\cos\theta \quad (s^{-1}) \,. \tag{3.18}$$

The associated photon energy bandwidths (ΔE_{ω},) the Bragg angles (θ_B,) and other parameters that are described below are given in TABLE III, at the spectrometer energies and for KAP crystals that have a layer spacing of $2d$ = 26.6 Å.

The reflecting surface of a real crystal is at least partially "mosaic" rather than a perfectly flat sheet. Mosaic refers to the surface being fractured into many small crystal facets whose surface normals are randomly shifted relative to that of the whole crystal. This will increase the solid angle of the reflected radiation. However, the angular deviations of the small crystal plates are insignificant compared to the angular resolution of the spectrometer. The crystal reflectivity integrated over such angular deviations provides the relative reflecting power and reflection angular width of a crystal at different Bragg angles.[57] Since a real crystal is unlikely to be perfect or completely mosaic, the average of the two reflectivites is used.

3.3.6.4. Crystal Reflectivity Curve Parameters

The reflectivity curve of a crystal is defined as the fraction of photons of a given energy reflected by the crystal at an angle θ (relative to a beam of photons of this energy incident at the same angle) over a range of angles as illustrated in Fig. 3.14. There is a strong local maximum in this curve at the Bragg angle (θ_B.) The integral of this curve in the region of the Bragg angle defines the integrated reflectivity (R_{mp}.) This integrated reflectivity is approximately the peak reflectance at the Bragg angle times the full-width half-max of this curve ($\delta\theta$.)

TABLE III. Parameters for KAP, $2d$ = 26.6 Å, and filter transmission at x-ray spectrometer energies.

$\hbar\omega/e$ (eV)	500	750	1000	2000	3000
θ_B (rad)	1.198	0.670	0.484	0.235	0.156
$\hbar\,\Delta\omega/e$ (eV)	6.31	30.5	61.2	269	615
R_{mp} (μrad)	33	49	63	100	120
$\delta\theta$ (mrad)	2.02	0.67	0.33	0.11	0.07
T_r	0.12	0.27	0.55	0.66	0.88
TrΔωRmp (eV•mrad)	0.025	0.40	2.1	18	65

It is more accurate to use the integrated reflectivity (R_{mp}) rather than $R_{peak}\ \delta\theta$ in calculating the signal produced by the detector. The effective solid angle collected by the detector at a given energy is the product of $\delta\theta$ and the horizontal angular resolution of the spectrometer channels ($\Delta\theta$.) The integrated reflectivities (R_{mp}) and the full-width half-max angle ($\delta\theta$) are given in TABLE III[58] for the appropriate photon energies.

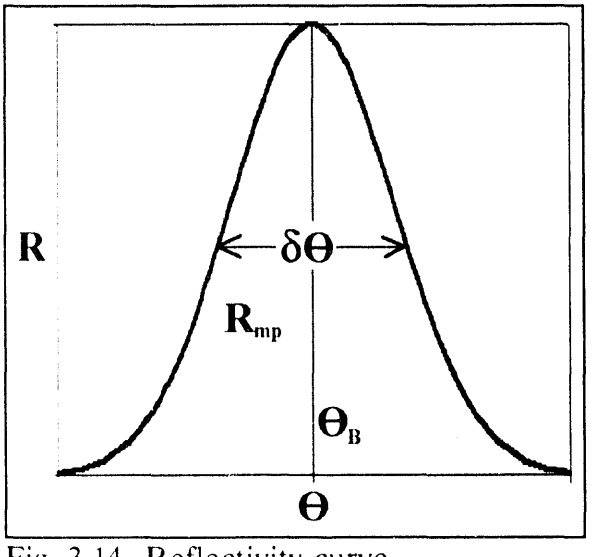

Fig. 3.14 Reflectivity curve. Showing how integrated reflectivity R_{mp} and full-width half-max $\delta\theta$ are defined.

3.3.6.5. Blast and Visible-Light Blocking Filters

Each spectrometer channel has a similar thin plastic blast filter and aluminized-plastic visible-light blocking filter; however, the transmission of the filters varies with photon energy. The spectrometer is open to the vacuum of the

load chamber to prevent attenuation of the x rays by a vacuum interface. However, a straight-line channel would leave the crystals exposed to debris from the pinch. Polypropylene filters of thickness 0.6 μm have been inserted between the second collimator holes and the crystals. Also, aluminized paralene filters (d_{Al} = 0.1 μm, d_{pr} = 0.1 μm) on the detectors block the visible light that reflects from the surface of the crystals. The PIN diode detectors are covered by a dead layer of silicon (d_{Si} = 0.7 μm) which also acts as a filter. The net transmission (T_r) of these filters at the energies of interest are also given in TABLE III.

3.3.6.6. PIN Diode Detectors

The collimated, filtered x rays are converted to electrical signals by PIN diode detectors made by the Quantrad Sensor Division of Applied Electron, Inc. They are reverse-biased to ~300 V. Channels *a* and *c* have detectors with an active area of A ≈ 25 mm^2 and channel *b* has an active area of $A \approx 100$ mm^2; however, the holder for the light blocking filter only allows $A \approx 25$ mm^2 to be exposed. The detectors all have an intrinsic layer thickness of $\ell \approx 125$ μm. The capacitance of detectors *a* and *c* is then

$$C_{PIN} \approx \epsilon_{Si}\, \epsilon_0\, A / \ell \approx 8.3 \times 10^{-7}\, A \approx 2.1 \times 10^{-11} \quad F\,, \tag{3.19}$$

where $\epsilon_{Si} \approx 11.7$ is the dielectric constant of silicon, and the capacitance of detector *b* is four times this value. The response time for a 50-Ω load is then about one nanosecond. At a bias voltage of ~300 V, a charge $Q \approx 6.3$ nC is available for fast pulses. This is larger than a typical signal charge of ~1 nC for the diagnostics described in this chapter.

The sensitivity of the detector is flat over the range of photon energies collected by the spectrometer and has a value of $S \approx 0.276$ A/W, according to the manufacturer specifications. The signal from the detector across a 50-Ω resistor

is 13.8 V per watt of x rays collected. This sensitivity is used by the simulation in calculating the expected signal strength but is not needed to calculate the electron temperature.

3.3.6.7. Ratio of Spectrometer Channel Signals

The signal W from a spectrometer channel is computed as the efficiency of the detector ϵ times the integral of the combined bremsstrahlung and free-bound emissivity $j(\omega)$ over the volume of the plasma that illuminates the detectors, over the range of photon frequencies collected by the channel, and over the solid angle subtended by the crystal-detector pair $d\Omega$:

$$W = \int dV \int_{\omega-\Delta\omega/2}^{\omega+\Delta\omega/2} d\omega \left\{ \varepsilon \; T_r \int d\Omega \; [R \, j(\omega)] \right\} \quad (V) \quad , \tag{3.20}$$

where the signal is reduced by the reflection efficiency of the crystal R and the transmission of the filters T_r. In terms of the parameters discussed above the signal is approximately

$$W = w(T_e) \; R_{mp} \; \varepsilon \; \frac{\hbar \Delta\omega}{e} \; e^{-\frac{\hbar\omega}{eT_e}} \quad (V) \quad , \tag{3.21}$$

where from Eq. (3.14)

$$w(T_e) = \frac{C_{Br} V \Delta\theta}{4\pi\hbar} \sqrt{\frac{e}{T_e}} \, n_e \sum_i \left[Z_i^2 n_i \left(g_{Br} + \frac{Z_i^2 R_y}{T_e} \sum_k \frac{2G_k}{k^3} \; e^{\frac{Z_i^2 R_y}{k^2 T_e}} \right) \right] \left(\frac{V}{eV} \right) \tag{3.22}$$

is the same for each channel. The ratio of two signals is then

$$R_{12} \equiv \frac{W_1}{W_2} = \frac{\varepsilon_1 \; T_{r1} \; R_{mp1} \; \Delta E_{\omega 1}}{\varepsilon_2 \; T_{r2} \; R_{mp2} \; \Delta E_{\omega 2}} \; e^{\frac{\hbar(\omega_2 - \omega_1)}{e \, T_e}} \quad . \tag{3.23}$$

The relative efficiencies of the crystal-detector pairs were calibrated by setting each pair to collect the same frequency of radiation and then exposing them to the same plasma radiation. These ratios have been measured at $\hbar\omega/e$ = 1000 eV for detectors *a*, *b*, and *c* as $K_{ab}(1\text{keV}) \approx 0.5$ and $K_{cb}(1\text{keV}) \approx 0.3$. (The subscripts *a*, *b*, and *c* reference the physical detectors; the subscripts 1 and 2 reference the photon energies they are set to collect. For the computed electron temperatures, E_a = 1000 eV, E_b = 500 eV, and E_c = 750 eV.) This measured ratio calibrates for differences in the sensitivity and active area between detectors.

The electron temperature can be computed from the measured ratio of signals R_{12} as

$$T_e = \frac{E_{\omega 2} - E_{\omega 1}}{\ln\left[\dfrac{R_{12}}{K_{ab}} \dfrac{T_{r2}\,\Delta E_{\omega 2}\,R_{mp2}}{T_{r1}\,\Delta E_{\omega 1}\,R_{mp1}}\right]} \quad (eV) \ . \tag{3.24}$$

The products of fixed constants in the logarithm are given in TABLE III.

Although the tables give parameters for five different spectrometer energies, only data for the first three energies are presented. This spectrometer was designed for the higher three energies, but the signals proved to be too weak. Therefore, channel *a* only collects photons at $E_a \approx 1000$ eV, channel *b* at $E_b \approx 500$ eV, and channel *c* at $E_c \approx 750$ eV. The electron temperature is computed from the ratios of the higher photon energy channel signals to that of the lower energy channel to avoid numerical difficulties. The three temperature measurements are then computed as

$$T_{ab} = \frac{500\ eV}{[3.7 - \ln(W_a/W_b)]} \ , \tag{3.25}$$

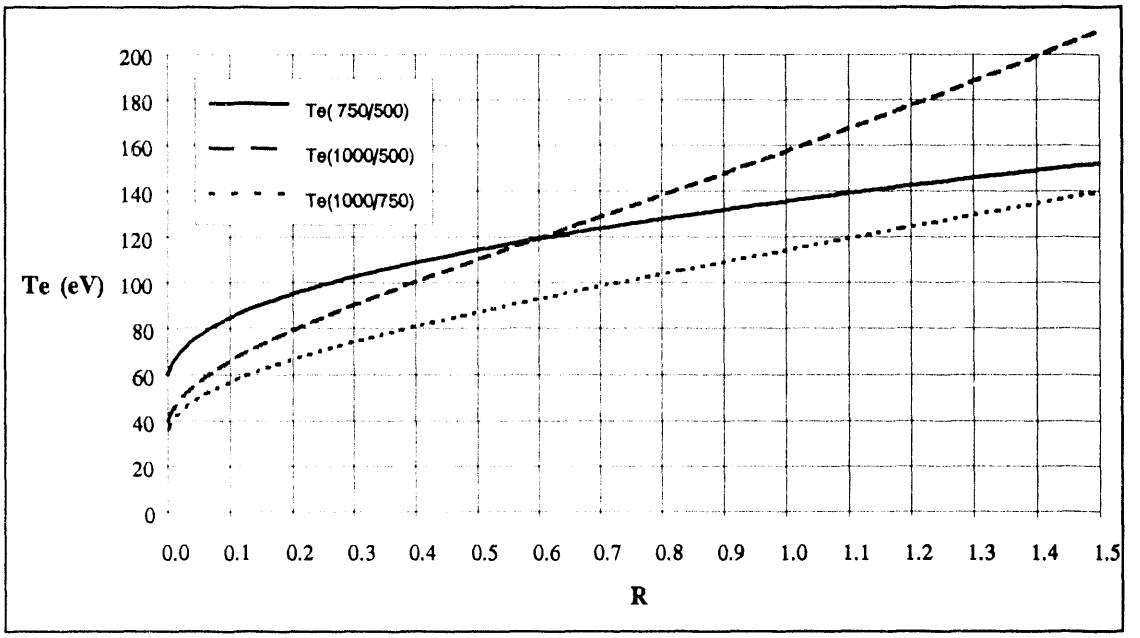

Fig. 3.15 Electron temperature vs. signal ratios.

$$T_{cb} = \frac{250\ eV}{[1.6 - \ln(W_c/W_b)]}\ , \tag{3.26}$$

and

$$T_{ac} = \frac{250\ eV}{[2.2 - \ln(W_a/W_c)]}\ . \tag{3.27}$$

Only two signals are required to compute the electron temperature. The redundancy of three channels provides independent measurements of the electron temperature.

The plots in Fig. 3.15 show the electron temperatures calculated as a function of these ratios. The variation of the electron temperature with the ratios is quite linear for ratios above 0.1.

3.3.7. Silver Activation Neutron Counter

The neutron yield produced for each shot was measured by a moderated silver activation neutron counter. The silver activation counter is the standard type developed by Lanter and Bannerman,[59] which consists of four Geiger-Müller (G-M) tubes, each wrapped with 10-mil silver foil and inserted into holes in a 12" × 12" × 6" block of polyethylene. Fast neutrons are moderated to thermal energy by the polyethylene and cause activation of the silver.

The installation and calibration of this diagnostic is described in Appendix D, which is excerpted from an internal report written by Dr. Robert Chrien. The calibration for this detector gave $(2.6 \pm 0.1) \times 10^5$ neutrons per count with a background count of 159 cpm.

IV RESULTS

This chapter describes the results obtained from the diagnostics. The electrical diagnostics record the voltage and current delivered to the load. The multiframe circular schlieren images the shape and size of the plasma as a function of time. The interferometer provides the electron density profile at one instant. The three-channel x-ray spectrometer measures the spatially averaged electron temperature as a function of time. The radius and electron temperature data were combined to infer a lower bound on the ion temperature, under the assumption of approximate pressure balance. The total neutron yield for each shot was measured using a sliver activation detector.

4.1. Timing Relative to the Current Signal

The time-resolved data in this chapter are presented relative to the main current signal recorded by the B-dot pickoff detectors. The current on any given shot can have a wide variety of prepulses due to capacitive feed-through of the water switch in the vertical transmission line. The zero time of each shot was normalized as shown in Fig. 4.1, which shows the current from shot 385. (This shot has a large prepulse.) The B-dot probe signal is recorded on a digital oscilloscope sampling every 2.5 ns and integrated numerically to yield the current through the load. A linear least-squares fit of the 10 current samples centered at the half maximum is extrapolated to zero current. This intercept provides the "zero time" of each current waveform, and all timing data for the shot is expressed relative to this time. All current through the load before this time is by definition a prepulse.

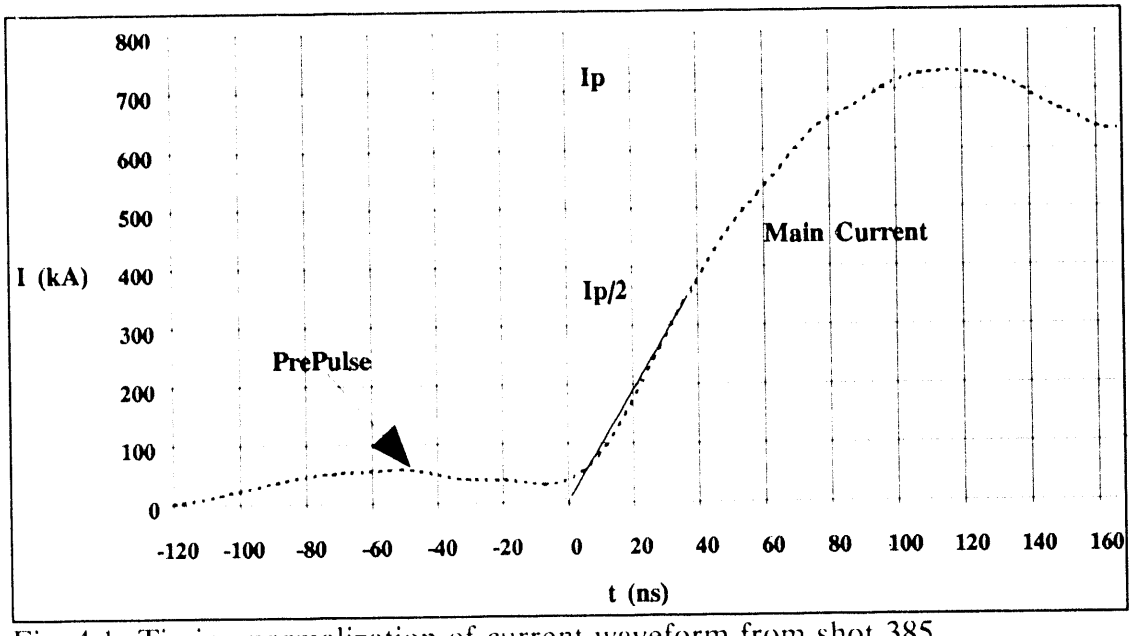

Fig. 4.1 Timing normalization of current waveform from shot 385.
Current curve near half-max current is extrapolated to "zero time" of current.

4.1.1. Current Prepulse Parameters

Current prepulses create different initial conditions of the pinch at the time the main current starts. A current prepulse provides an inductive load which is qualitatively different from a solid fiber. Prepulses are described in terms of their qualitative "shape" and the integral of the prepulse current in mC. The prepulse shapes are illustrated in Fig. 4.2. A "hook" shape is a "bump" shape that was interrupted by an early start of the main current. Similarly, the "parabolic" shape is very close to the "double ramp" shape, and so the designation of shape is somewhat subjective.

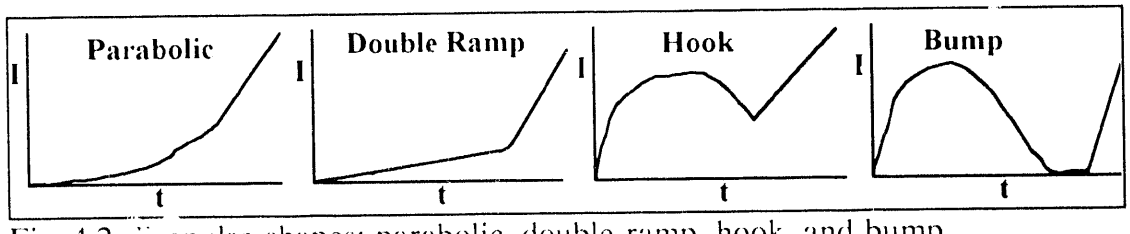

Fig. 4.2 Prepulse shapes: parabolic, double ramp, hook, and bump.

4.2. Radius vs. Time from Circular Schlieren

The multiframe circular schlieren provides up to eight images of the shape of the plasma-vacuum boundary at 10-ns intervals. The sequence of images shown in Fig. 4.3 are from shot 410, which had a CD_2 solid-fiber radius of $r_0 \approx 19$ μm.

Frame 1 of Fig. 4.3 is a circular-schlieren image of the solid fiber, partially obscured by the integrated image of the light collected before the start of the sweep. The next image shows the rapid initial expansion of radial jets of plasma called "spicules". The loss of the sixth frame is due to the pulse being rerouted to the interferometer. The right edge of the eighth frame was swept off the edge of the phosphor screen and was not recorded on the film.

4.2.1. Circular-Schlieren Radius Measurement Method

The irregular shape of the circular-schlieren image edges make it difficult to describe each frame by a single "averaged" radius. The rms radius was chosen for comparison with the 0-D simulation rather than a simple mean. This radius defines a uniform cylinder of volume equal to that of the irregularly shaped plasma-vacuum boundary depicted in the circular-schlieren images. This cylinder

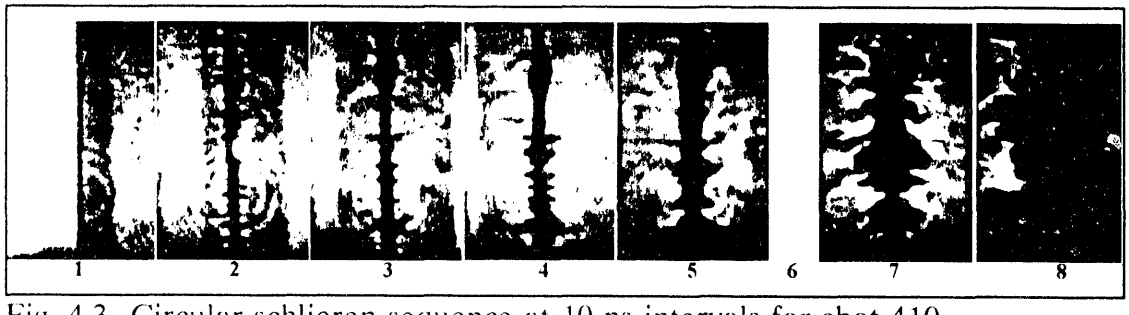

Fig. 4.3 Circular-schlieren sequence at 10-ns intervals for shot 410. Each frame is 2.4 mm wide. The laser pulse for frame six was routed to the interferometer and is not included due to underexposure.

and the plasma will have the same average density if most of the plasma is within this boundary.

The "radius" of the plasma is measured for each circular-schlieren image as follows. First, it must be assumed that the plasma density falls off sharply at a boundary with the surrounding vacuum; in the following section, the interferometer data will be used to show that this is a reasonable assumption. It is also assumed that the plasma is axi-symmetric. This seems justified by the high degree of left-right symmetry of the circular schlieren images about the pinch axis.

Each image was digitized, and the column positions of the left and right edges of the shadow for each row of image pixels were determined from the horizontal gradient in image intensity. The least-squares fit of the axis location was computed from these edges, weighted by the strength of the edge gradients of the image. The rms radius of the shadow was computed as the square root of the weighted sum of the squares of the distance of the edges from this axis:

$$r_{rms} = Res \times \sqrt{\sum_{i=1}^{NRow} \left[(jl_i - jaxis_i)^2 \nabla l_i + (jr_i - jaxis_i)^2 \nabla r_i \right] / \sum_{i=1}^{NRow} \left[\nabla l_i + \nabla r_i \right]} , \quad (4.1)$$

where *Res* is the size of the image pixels in meters, *NRow* is the number of rows in the image, jl_i and jr_i are the column positions of the left and right edges, ∇l_i and ∇r_i are the strength of the gradients at the left and right edges, and $jaxis_i$ is the column position of the pinch axis for row *i*. This is effectively the cross-sectional area of the pinch, averaged over the axial length of the image.

The slope of the axis is nearly vertical and constant from frame to frame but not shot to shot, since the position of the solid fiber varies from shot to shot. This parameter can be more accurately measured in earlier frames. The measured slope from the earlier frames can be used in finding the axis in later images to

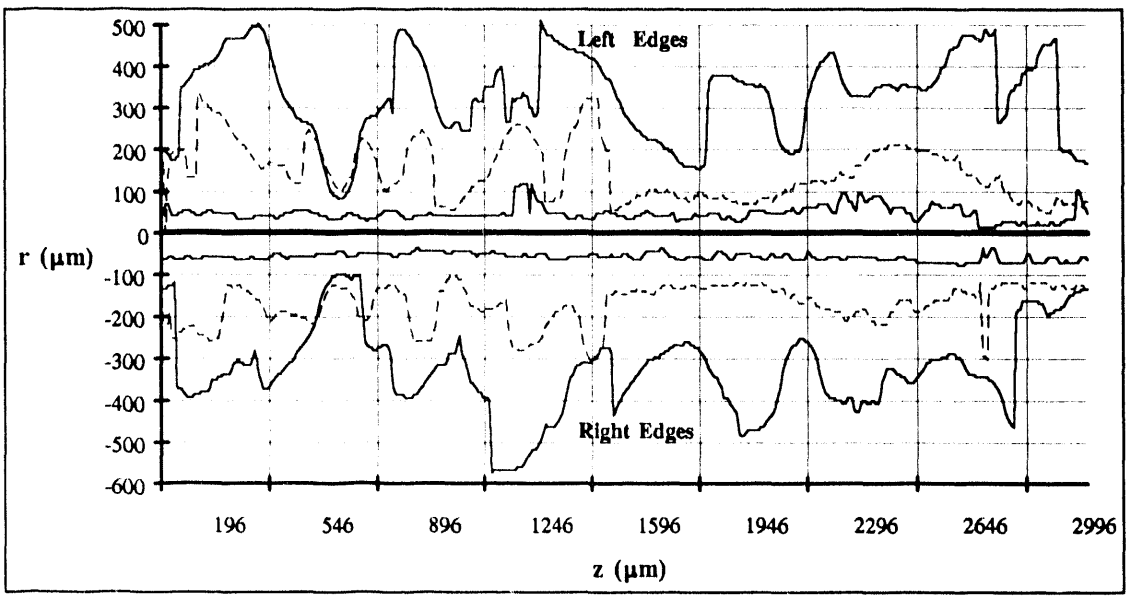

Fig. 4.4 Circular-schlieren edges vs. z for frames 1,4, and 7 of shot 410. Left/right edge radii are plotted as positive/negative values. Axial distance is relative to bottom of frame.

improve the accuracy of the radius measurements. If only one edge can be measured in a partial image, the horizontal position of the axis is also input as being the same offset from the side of the frame as another frame in the sequence. This seems to be justified by the lack of horizontal motion of the axis, relative to the frame, in the frames which have complete left and right edges of the shadow. The lack of horizontal motion of the pinch in the two orthogonal planes image by the circular schlieren and the interferometer is evidence that there are not large wavelength $m = 1$ instabilities growing within the first 50 ns of the main current.

The plots in Fig. 4.4 show the measured edges for the circular-schlieren images in frames 1, 4, and 7 of Fig. 4.3. The left and right edge radii are plotted as a function of the position along the z axis. The right-edge radii are plotted as negative values. The symmetry of the edges about the axis is consistent with the

axi-symmetry of $m=0$ instabilities. The initial expansion of the radius is slower than during the main current because these frames were taken during a 53-ns current prepulse. The first frame was taken at the onset of this prepulse current. The minimum radii of the "necks" of frame 7 dip below the average radii of frame 4, suggesting that the mass of the plasma has begun to flow axially.

4.2.2. Radius vs. t data

The radius vs. time data are divided into six bins according to the CD_2 solid-fiber radius of the shots. This variation in solid-fiber radius does not seem to have a large effect on the expansion of the plasma, but it will be shown in the next chapter that some of the models predict that it should. The bins were chosen so that there would be approximately five shots presented in each bin. Plots of these bins are shown in Fig. 4.5, Fig. 4.6, Fig. 4.7, Fig. 4.8, Fig. 4.9, and Fig. 4.10. The error bars are based on the irregularity of the shape of the circular-schlieren images. The data points of each shot are connected by lines to make it easier to find all of the points of a given shot. The data in the plots are referenced by shot number since there are multiple shots at the same solid-fiber radius. The solid-fiber radius for each shot number is given in TABLE IV with parameters describing the current prepulse of the shot. Data taken before the last 10 ns of the prepulse current is not presented due to the wide variety of prepulse currents. The physics of the initial stages of the breakdown of the fiber into a cold dense plasma is quite different from the plasma conditions for the majority of the main current and is beyond the scope of this document.

TABLE IV. Parameters for circular-schlieren shots: solid-fiber radius bin, shot number, solid-fiber radius (μm), peak current (kA), integral of the prepulse current (mC), and prepulse shape.

Bin	Shot	r_0 μm	I_P kA	Q_{pre}	$Shape_{pre}$	Bin	Shot	r_0 μm	I_P kA	Q_{pre}	$Shape_{pre}$
1	362	10.25	567	0.11	None	2	367	16.00	677	1.34	DRamp
1	379	13.75	608	0.00	None	2	370	16.00	677	3.92	DRamp
1	369	14.50	852	5.85	Hook	2	374	16.00	721	1.02	Parab
1	373	14.50	628	5.35	Hook	2	376	16.25	590	0.39	None
1	377	14.50	653	0.27	None	2	381	17.00	551	0.17	None
3	417	18.50	530	0.09	None	4	402	22.25	672	4.13	Bump
3	408	19.00	820	1.52	DRamp	4	403	23.75	749	1.42	Parab
3	410	19.00	820	1.95	DRamp	4	411	26.75	800	1.83	DRamp
3	353	20.50	749	1.05	DRamp	4	386	27.50	687	1.73	DRamp
3	409	20.75	795	1.76	DRamp	4	385	31.00	730	4.46	Hook
5	415	34.50	640	0.04	None	6	382	39.75	717	3.94	Bump
5	372	35.00	710	3.85	Bump	6	423	43.25	676	0.08	None
5	383	36.25	697	4.87	Bump	6	416	57.00	547	0.30	None
5	405	36.50	621	4.24	Bump						

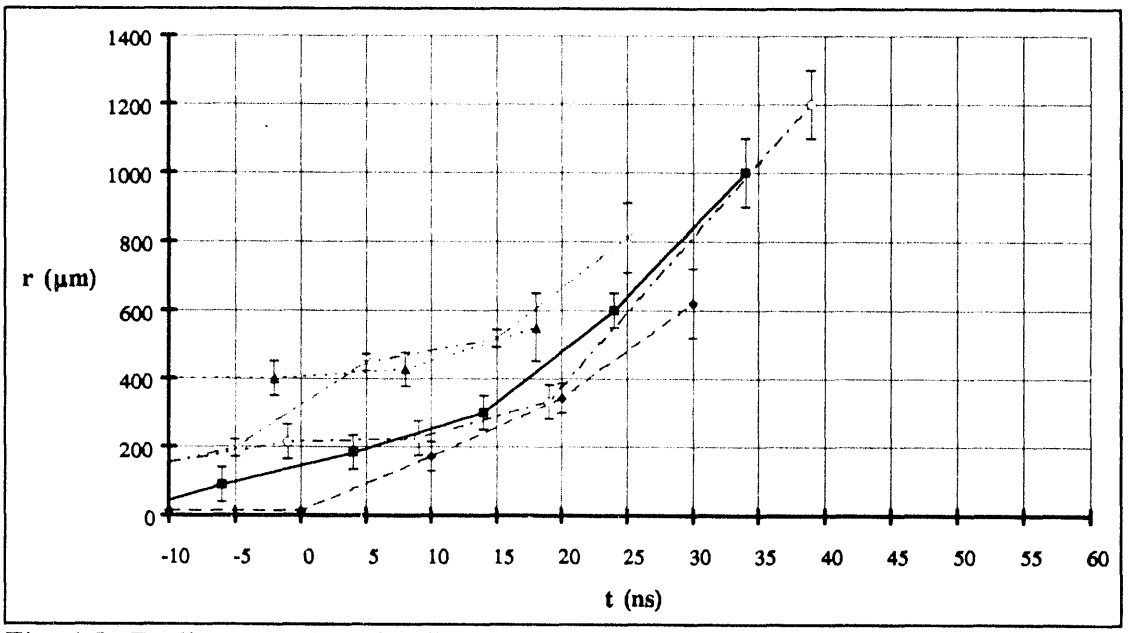

Fig. 4.5 Radius vs. t data for fiber-radius bin 1: 10.3-14.5 μm.
Legend: (■) shot 362, (♦) shot 379, (▲) shot 369, (O) shot 373, and (x) shot 377.

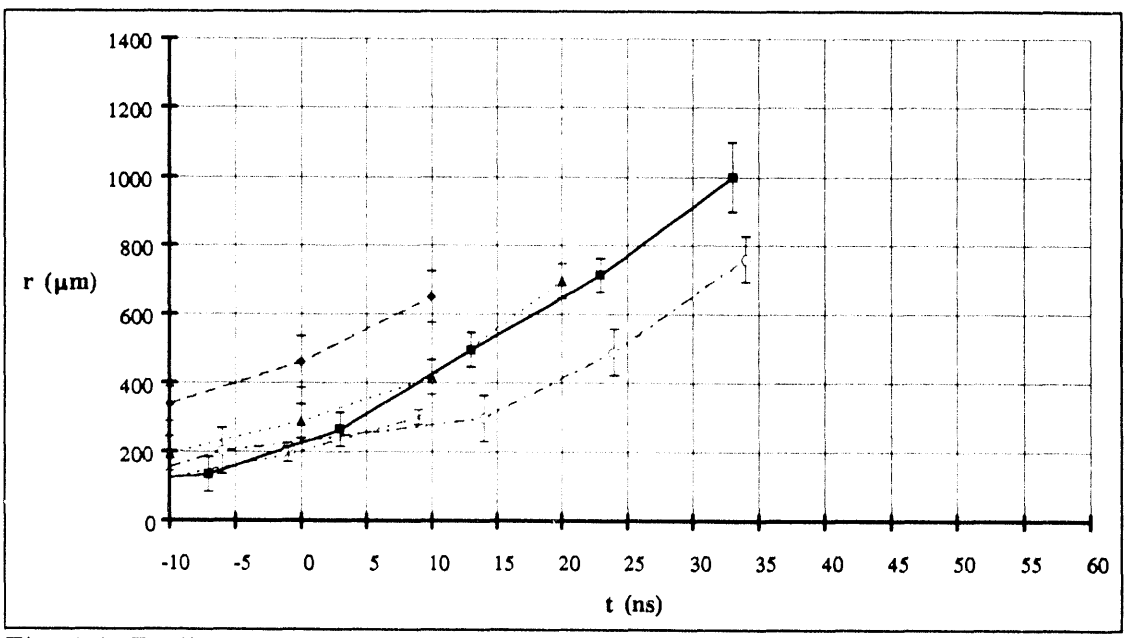

Fig. 4.6 Radius vs. t data for fiber-radius bin 2: 16.0-17.0 μm.
Legend: (■) shot 367, (♦) shot 370, (▲) shot 374, (O) shot 376, and (x) shot 381.

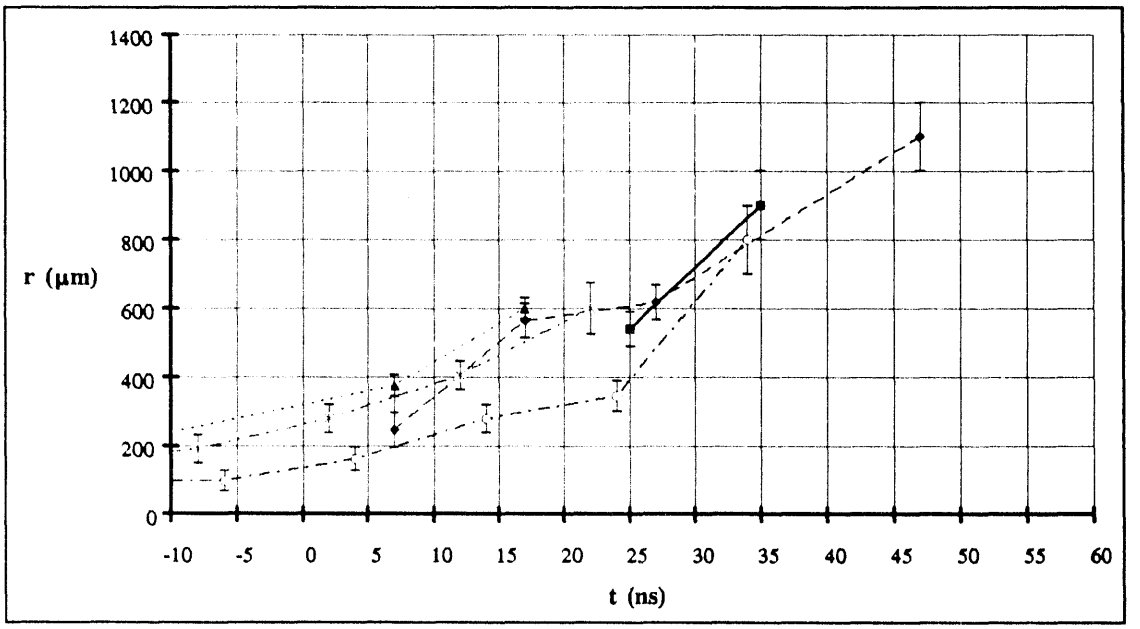

Fig. 4.7 Radius vs. t data for fiber-radius bin 3: 18.5-20.8 μm.
Legend: (■) shot 417, (♦) shot 408, (▲) shot 410, (O) shot 353, and (x) shot 409.

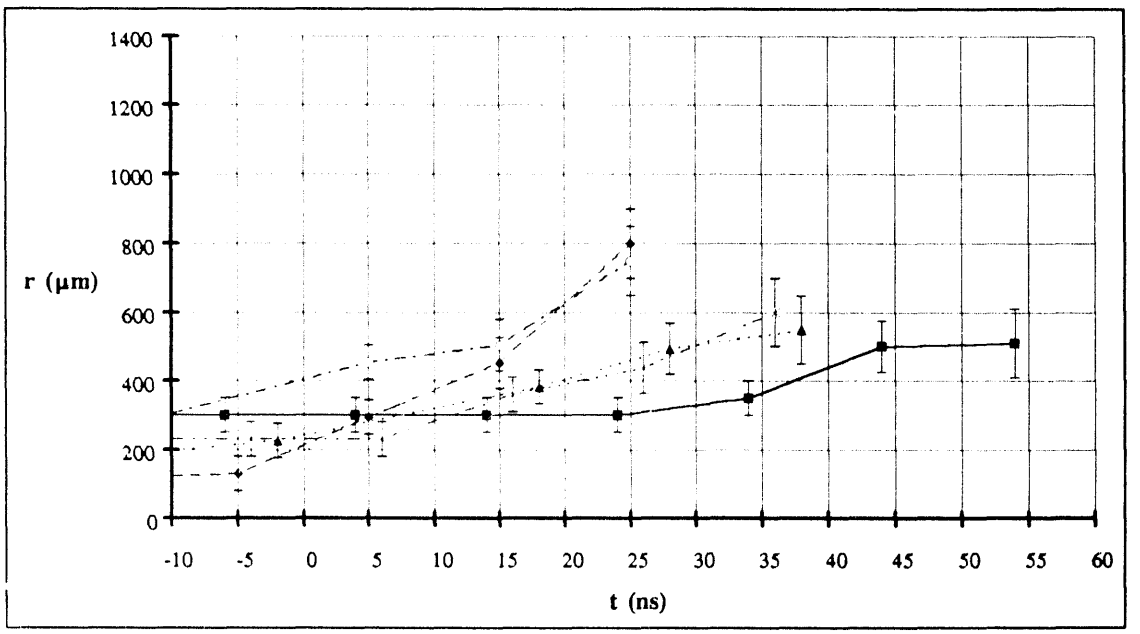

Fig. 4.8 Radius vs. t data for fiber-radius bin 4: 22.3-31.0 μm.
Legend: (■) shot 402, (♦) shot 403, (▲) shot 411, (O) shot 386, and (x) shot 385.

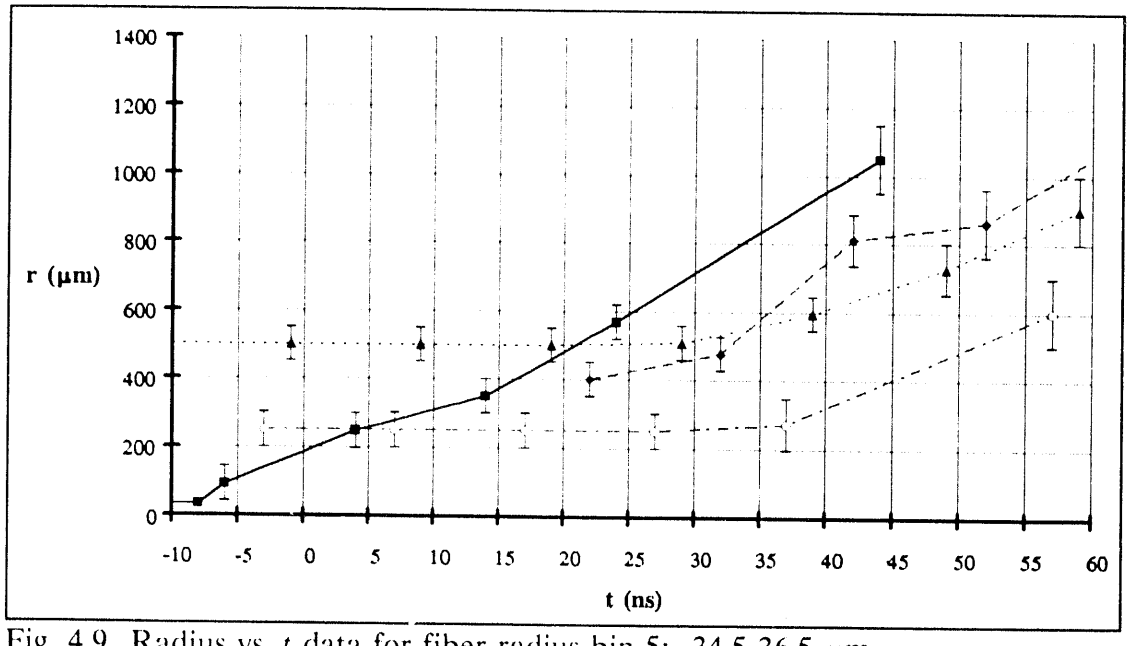

Fig. 4.9 Radius vs. t data for fiber-radius bin 5: 34.5-36.5 μm.
Legend: (■) shot 415, (♦) shot 372, (▲) shot 383, and (O) shot 405.

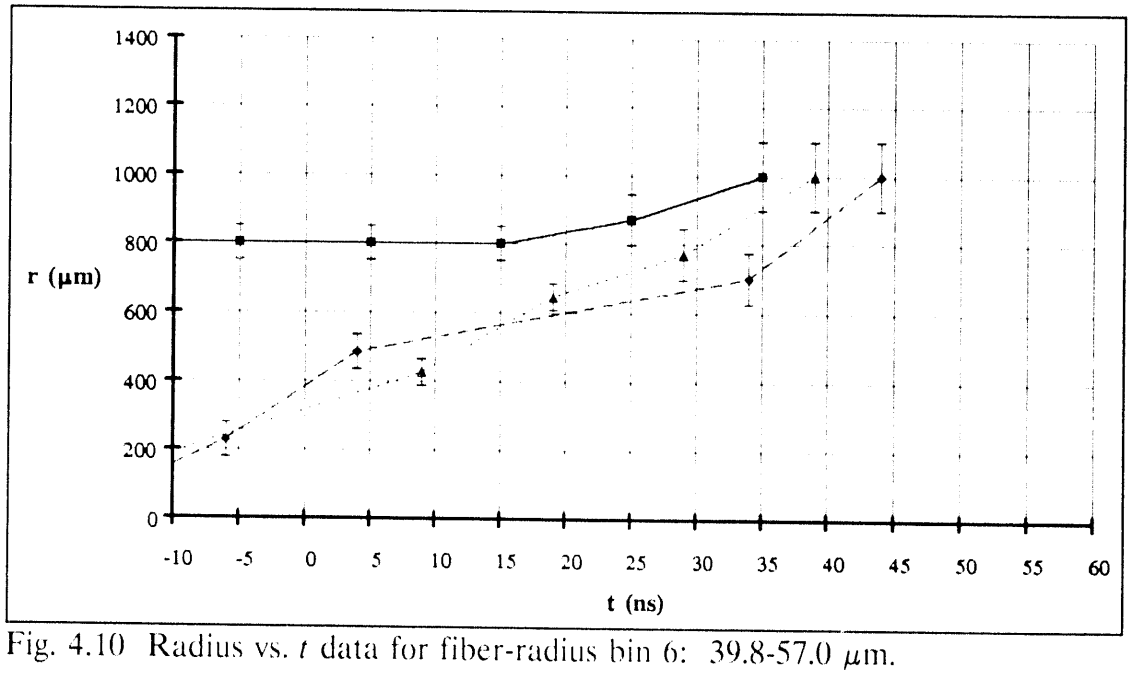

Fig. 4.10 Radius vs. t data for fiber-radius bin 6: 39.8-57.0 μm.
Legend: (■) shot 382, (♦) shot 423, and (▲) shot 416.

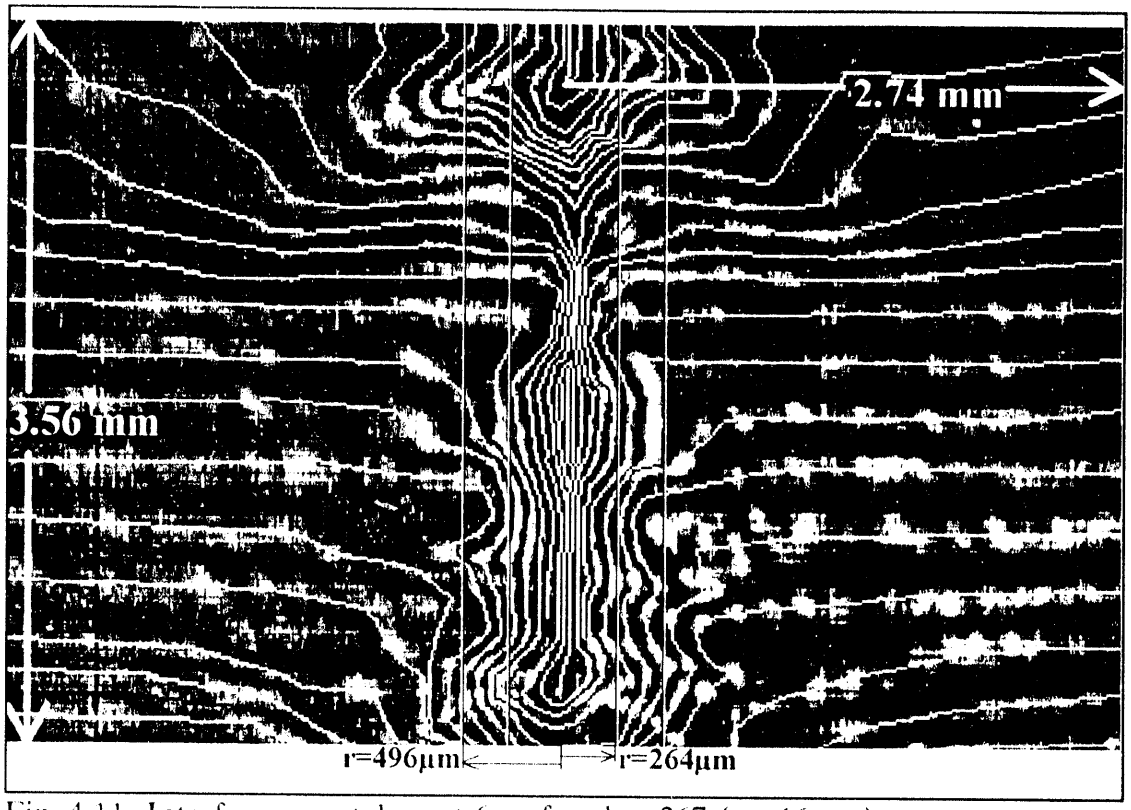

Fig. 4.11 Interferogram taken at 6 ns for shot 367 (r_0=16μm.)
The fringes are highlighted and circular-schlieren radii at 3 and 13 ns are drawn.

4.3. Electron Density Profile from Interferometry

The interferogram shown in Fig. 4.11 (5.48 mm wide and 3.56 mm tall) was taken by the point-diffraction interferometer at 6 ns into the main current of shot 367 with a solid-fiber radius of r_0 = 16 μm. The fringes have been emphasized by scaling the image grey-values to 2-253 and labeling the fringe maxima and minima with lines at 255 and 0. (Interferograms are collected as eight-bit digital images (0-255), where 0 is black and 255 is white. They are converted to one bit per pixel images with 1800 columns before being printed on a 300 dot per inch laser printer.)

The vertical lines mark the radii (264 and 496 μm) measured by the circular schlieren at 3 and 13 ns into the main current as given in Fig. 4.6. Although there is obviously a tenuous halo outside these radii at some axial positions, the Abel inversion presented below shows that the average radius of the plasma imaged in the interferogram can reasonably be said to fall within r(3ns) = 264 μm and r(13ns) = 496 μm.

The plots in Fig. 4.12 show the electron line density computed as described in Section 3.3.4.3 from the interferogram shown in Fig. 4.11. The maximum line density is about a factor of three larger than the minimum, showing some axial flow of particles as early as 6 ns into the main current. For each row of the image, the column positions of the fringe maximums and minimums (marked with 255 and 0) are found and then the fringes are integrated by a simple trapezoid algorithm. The error bands assume that the number of fringes counted from the edge of the image has an uncertainty of $\pm 1/2$ fringe over the entire width of the

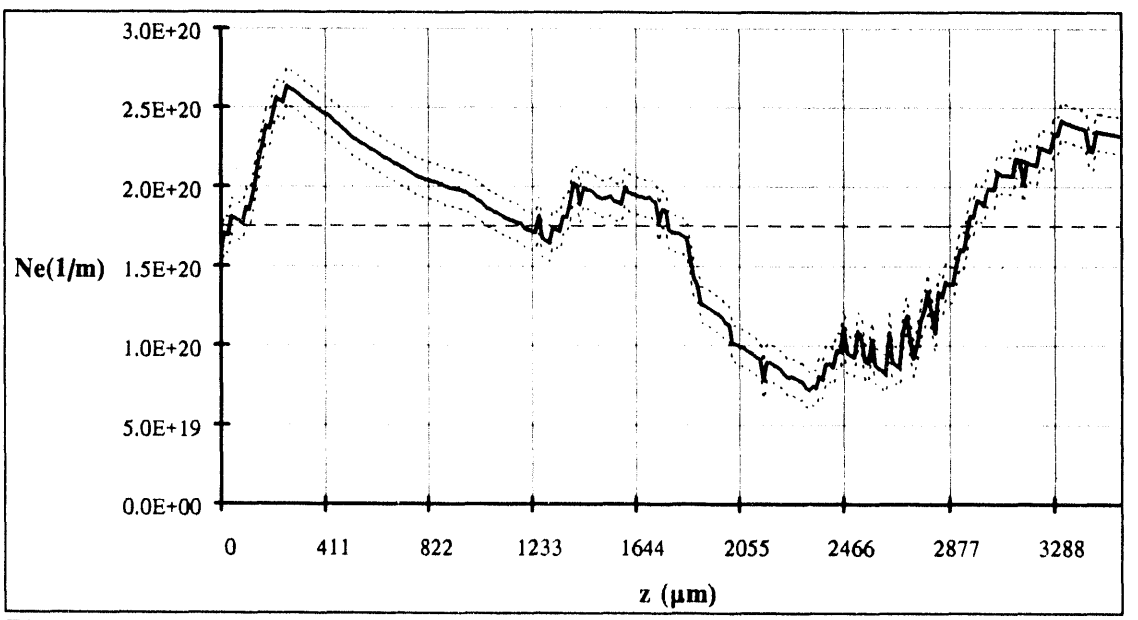

Fig. 4.12 N_e vs. z at 6 ns for shot 367 (r_0 = 16μm.)

Pinch has average value $N_e \approx 1.7 \times 10^{20}$ m^{-1} and inferred carbon ionization $Z_c \approx 3.8$.

interferogram. The average line density of this section of the pinch ($N_e \approx 1.7\times10^{20}$ m^{-1}) corresponds to an average carbon ionization state of $Z_c \approx 3.8$.

The image in Fig. 4.13 shows the electron density as a function of radial and axial position computed by Abel inversion, described in Section 3.3.4.3, from the fringe data extracted from the interferogram in Fig. 4.11. The intensity of the image is proportional to the logarithm of the density. The peak electron density on axis is 2×10^{27} m^{-3}, just short of the cut-off density ($n_{crit} \approx 4\times10^{27}$ m^{-3}) for this wavelength of light. The range of image intensities covers the range of densities from 10^{25} m^{-3} < n_e < 2×10^{27} m^{-3}, electron densities below this range are set to white.

As in Fig. 4.11, the radii (r(3ns) = 264 μm and r(13ns) = 496 μm) measured from the two circular-schlieren images taken before and after the interferogram

Fig. 4.13 Image of log[$n_e(r, z)$] at 6 ns for shot 367 (r_0=16μm.)
Peak electron density $\approx 2\times10^{27}$ m^{-3} on the axis.

are marked by vertical lines for scale. This image shows the full field of view (5.48 mm wide and 3.56 mm tall) of the original interferogram. The outline is very similar to the circular-schlieren images taken at 3 ns and 13 ns shown in frames 3 and 4 of Fig. 3.11

The wire plot in Fig. 4.14 shows the same electron density data. Again, the range of densities plotted are limited to 10^{25} m^{-3} < n_e. The zero radius corresponds to the horizontal center of the interferogram, and the zero position of the z coordinate corresponds to the bottom of the interferogram. Only 2 mm of the 5.48 mm total width of the interferogram is plotted. The density falls off steeply with radial position even on a logarithmic scale.

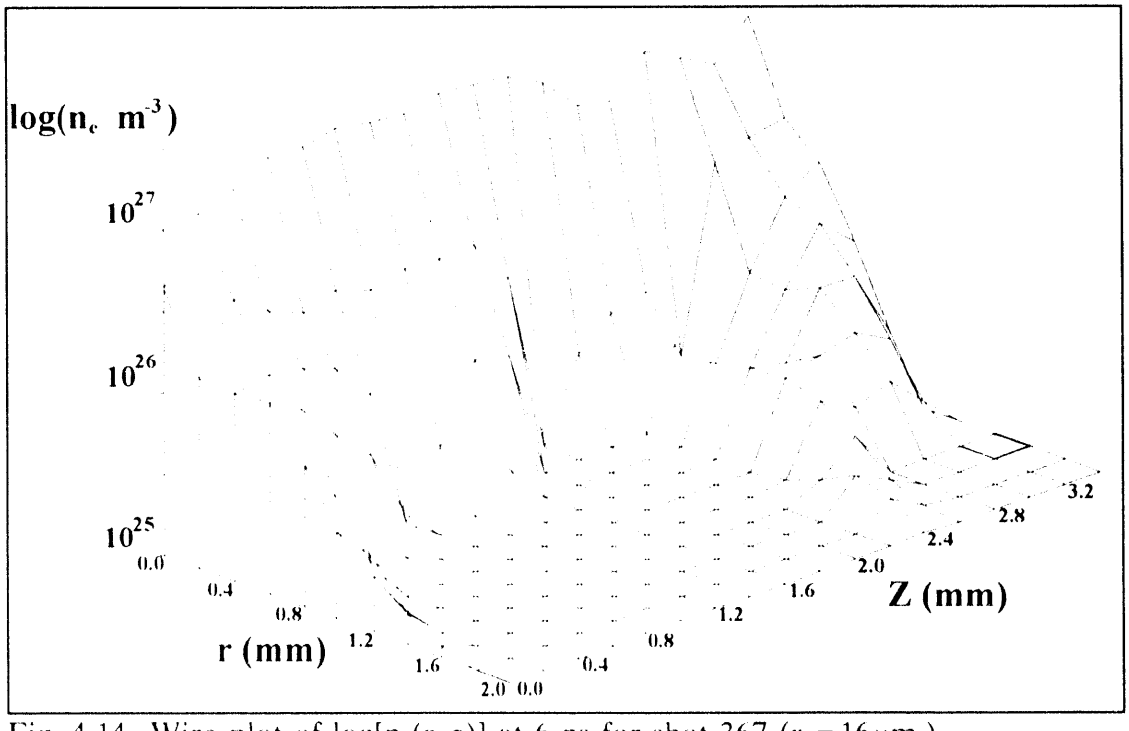

Fig. 4.14 Wire plot of log[$n_e(r, z)$] at 6 ns for shot 367 (r_0 = 16μm.) The peak electron density ≈ 2×10^{27} m^{-3} on the axis.

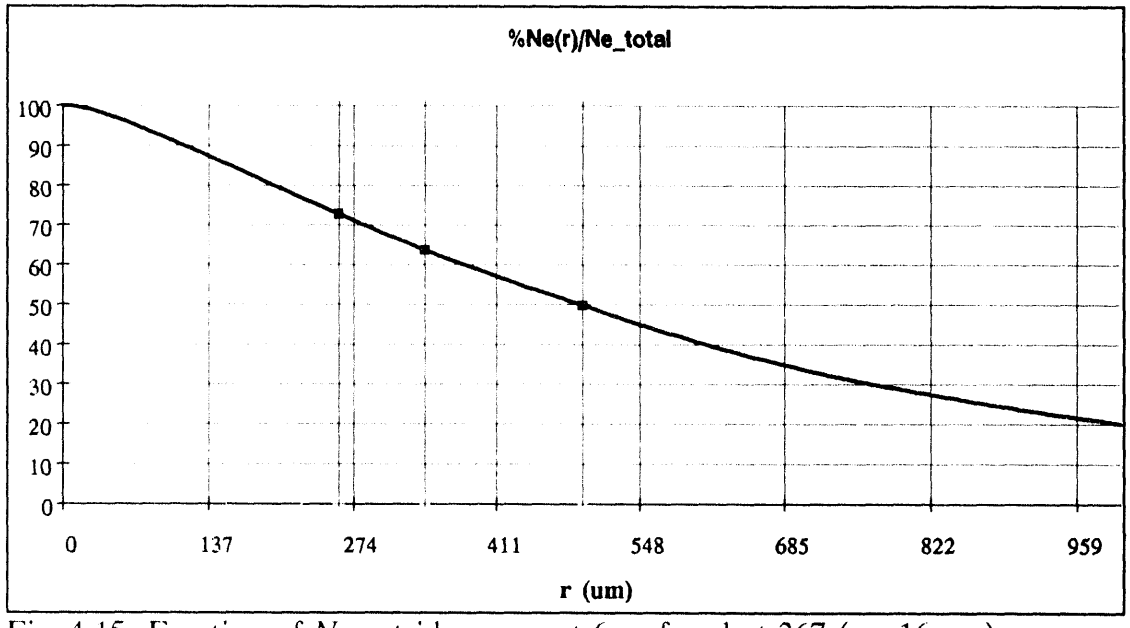

Fig. 4.15 Fraction of N_e outside r vs. r at 6 ns for shot 367 ($r_0 = 16\mu$m.) The radii (264, 496 μm) from circular-schlieren images taken at 3, 13 ns are marked with interpolated radius 334 μm at 6 ns.

The plot in Fig. 4.15 shows the fraction of the electron line density outside a straight cylinder of radius r vs. r averaged over the length of the z axis shown in the interferogram displayed in Fig. 4.11. The radii measured from the circular-schlieren images taken 3 ns before and 7 ns after the interferogram are marked along with the radius interpolated to the time of the interferogram. In this case, the circular-schlieren radius is a good estimate of the pinch radius falling near the 50 percentile of the number of enclosed particles. This plot underestimates how well the circular schlieren measures where the plasma is by using a straight cylinder instead of the shape of the schlieren image. However, it is clear that the density profile of the plasma is far from the uniform cylinder assumed by the 0-D model.

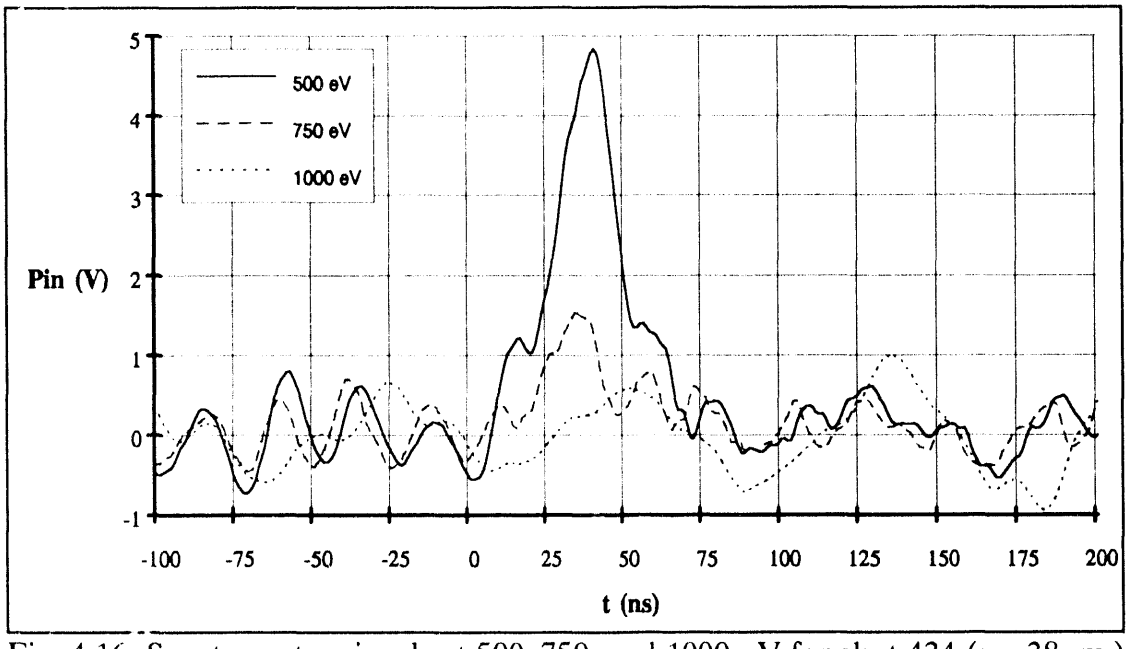

Fig. 4.16 Spectrometer signals at 500, 750, and 1000 eV for shot 434 (r_0=38μm.) Plot shows background noise with an amplitude of ~ 1 V.

4.4. Electron Temperature from X-Ray Emissions

The plots in Fig. 4.16 show the spectrometer signals for the 500, 750, and 1000-eV channels for shot 434. This typical spectrometer data has a background noise signal of amplitude ~1 V contained in two narrow frequency bands.

The plots in Fig. 4.17 show the noise power spectra of the three channels. The signals before the main current and after 100 ns into the main current were assumed to be noise. (All of the data presented from the spectrometer were taken after the shielding plate was added to the water switch, and so there is no current prepulse associated with these shots.) The noise is strongest in the frequency bands (12 < f < 18 MHz) and (29 < f < 49 MHz). The FFTs of the signals were filtered by zeroing the (29 - 49 MHz) frequency band and subtracting the FFT of the noise in the (12 - 18 MHz) band from the FFT of the signal.

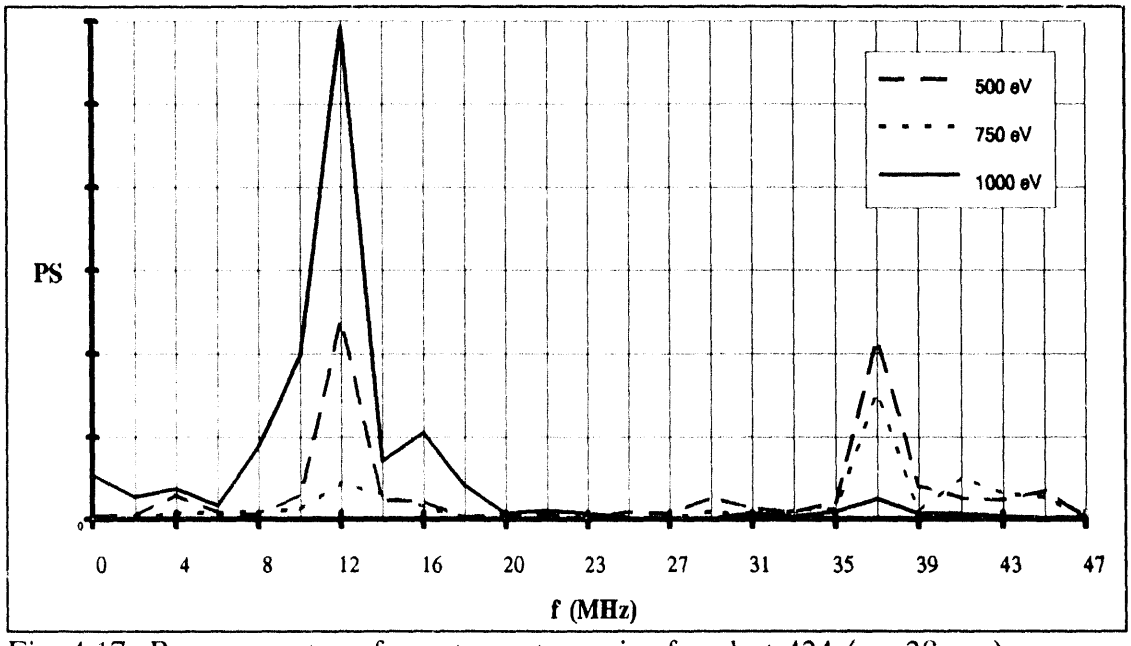

Fig. 4.17 Power spectra of spectrometer noise for shot 434 (r_0=38μm.)
The noise is strongly peaked at 12 and 37 MHz.

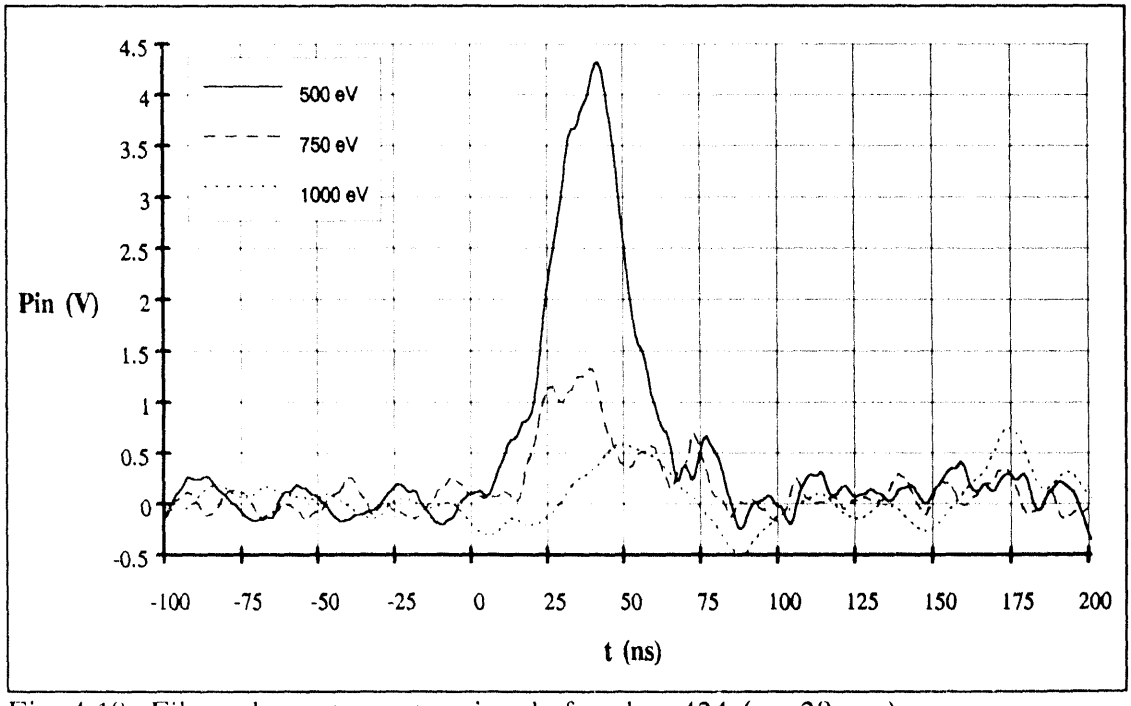

Fig. 4.18 Filtered spectrometer signals for shot 434 (r_0=38μm.)
The noise amplitude reduced from ~ 0.5 V to ~ 0.3 V.

The filtered signals are shown in Fig. 4.18. This filtering reduces the noise amplitude to about 0.3 V, which is still comparable to the 1000-eV signal. The spectrometer channels were changed from the original energy settings at 1, 2 and 3 keV because it was found that the plasma electron temperature never reached a level which produced large amounts of x rays above 1 keV.

The plasma electron temperature is computed from the ratios of the filtered signals, as described in Section 3.3.6.7. The plots in Fig. 4.19 show the temperatures computed from the three ratios of the 500, 750, and 1000 eV channels. The curves above and below represent error bands based on adding and subtracting 0.3 V (noise amplitude) from the signals; the numerator and denominator of the ratios are limited to be at least 0.01 to prevent numerical problems.

$$Te_{Max} = \frac{\Delta E_{AB}}{C_{AB} - \ln\left(\frac{A-0.3V}{B+0.3V}\right)} \qquad Te_{Min} = \frac{\Delta E_{AB}}{C_{AB} - \ln\left(\frac{A+0.3V}{B-0.3V}\right)}, \qquad (4.2)$$

where the subscripts A and B refer to the spectrometer signals whose ratios are used to calculate the electron temperature. The error bars are generally smallest for the 750/500 ratio. The temperatures given in TABLE V for other shots were computed from the 750/500 ratio if available, otherwise from the 1000/500 ratio.

The temperature remained close to 95 eV for the entire time that the signals are strong enough to calculate the temperature with any accuracy. The stable theory predicted that the electron temperature would grow monotonically to over 1 keV in the first 100 ns, hence the original choice of spectrometer energies at 1, 2, and 3 keV.

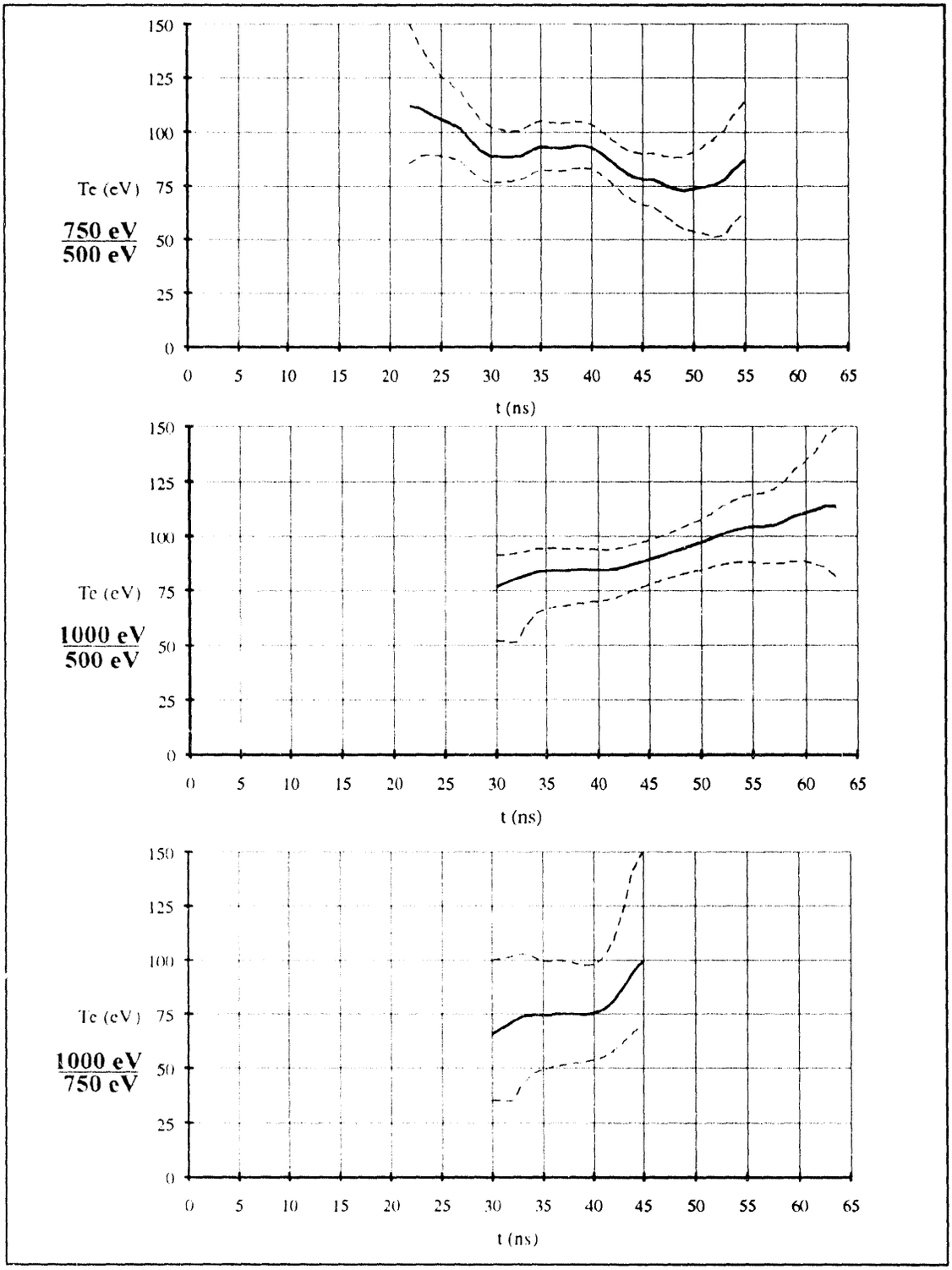

Fig. 4.19 T_e from each of three ratios vs. t for shot 434 (r_0=38μm.)
Error bands are from computing temperatures from ratios of signals ± 0.3 V.

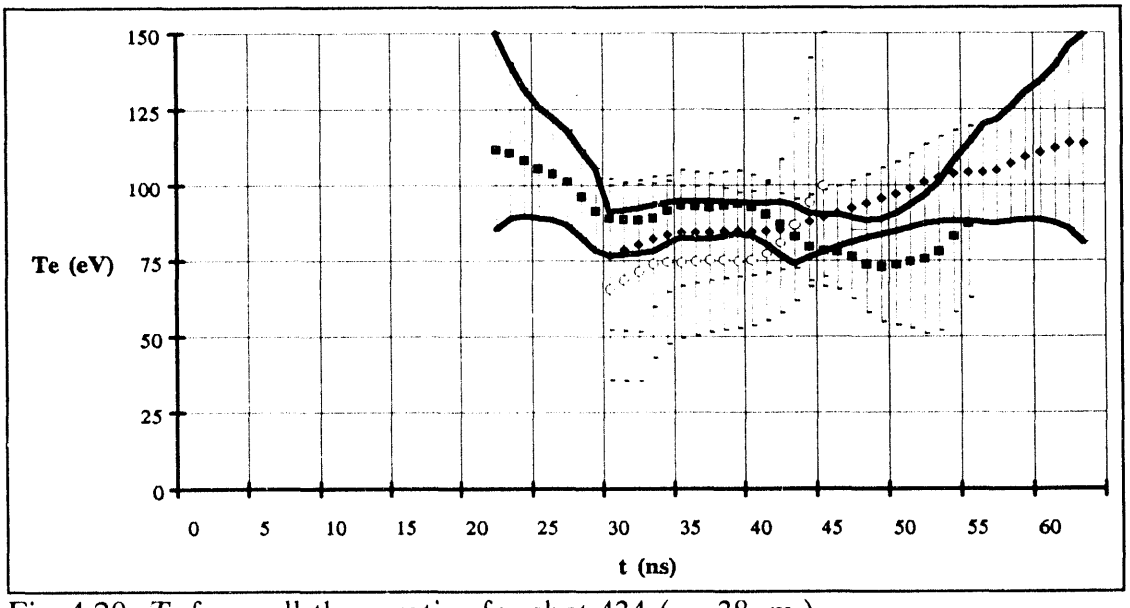

Fig. 4.20 T_e from all three ratios for shot 434 (r_0=38μm.)
The least-upper and greatest-lower bounds show that the error bands overlap.

The plots in Fig. 4.20 show the three calculated electron temperatures. The heavy lines show the least-upper and the greatest-lower bounds of the error bars of the three curves, showing that there is a region where the error bands overlap. Thus, the three electron temperature curves are consistent with each other, within experimental error, supporting the assumption that they are sampling bremsstrahlung and free-bound radiation.

TABLE V shows that the electron temperature averaged over time is very consistent over the entire range of solid-fiber radii (3.5-38μm). The time-averaged temperature is given because the temperature varies so little over the time that the temperature can be measured. The spectrometer signal became strong enough to measure the temperature at about the same time into the main current (20-50 ns), and the computed temperature remains flat at ~90 ± 15 eV for the entire time the signals are strong enough to compute the temperature. The 750-eV channel was not installed for the shots with smaller solid-fiber radii

(425-427). The length of time the signals are strong seems to be longer for smaller solid-fiber radii.

TABLE V. Electron temp. vs. r_0.

$r_0(\mu m)$	Shot	t(ns)	Te(eV)
3.5	425	50-115	68±30
9.3	426	25-110	74±30
16.3	427	30-90	93±30
17.3	428	35-95	102±20
20.3	429	40-85	87±15
24.5	432	45-80	95±15
28.8	430	42-80	95±15
30.8	431	32-81	94±15
35.3	433	35-80	95±15
38	434	20-65	95±15

The plots in Fig. 4.21 show the 500-eV channel signals for shots over the range of solid-fiber radii of 3.5-20 μm. The signals seem to have two bumps. The shots with the smaller solid-fiber radii seem to have a larger second bump. As the solid-fiber radius increases, the second bump becomes smaller and the first bump becomes larger until only the first is seen for radii above 17 μm.

These bumps will be interpreted in the next chapter in terms of changes in the density of the expanding plasma that lead to changes in the ionization of the carbon ions despite the electron temperature remaining relatively constant.

4.4.1. Ion Temperature Estimation from T_e

Though the plasma seems to be expanding rapidly based on the circular schlieren data presented in Section 4.2, a lower bound on the ion temperature can be computed from the electron temperature and the current based on quasi-pressure balance between the magnetic field produced by the current and the kinetic pressure of the ions and electrons (Bennett equilibrium) as discussed in Section 1.3

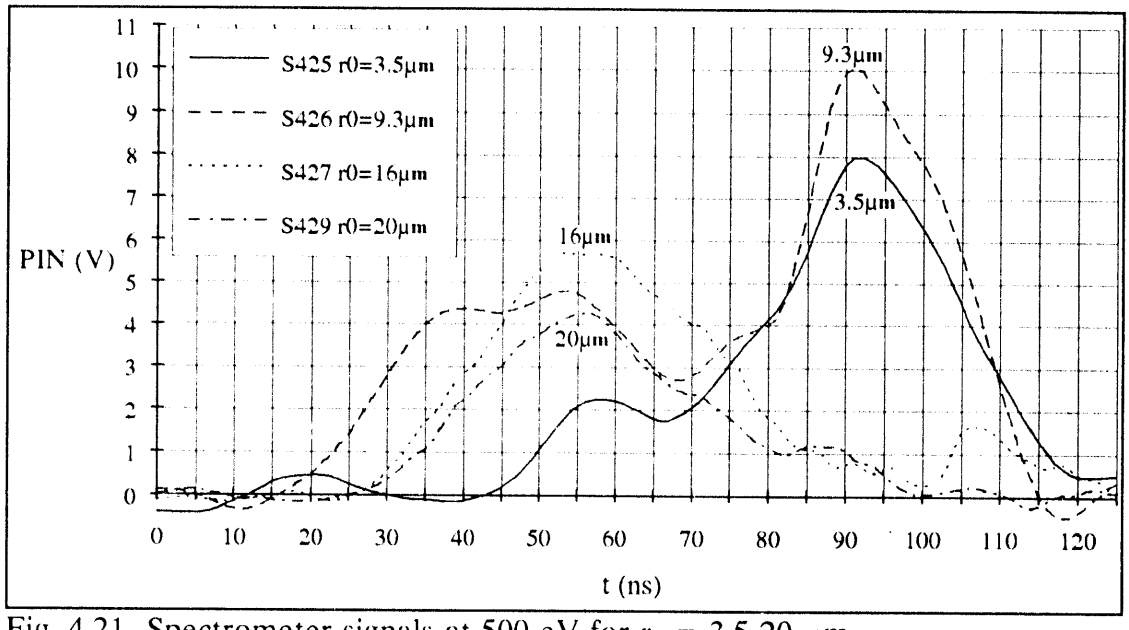

Fig. 4.21 Spectrometer signals at 500 eV for r_0 = 3.5-20 μm.

$$T_i \approx \frac{\mu_0 I^2}{8\pi e \Sigma N_i} - \frac{N_e}{\Sigma N_i} T_e \approx 8.83\times10^{-19}\left(\frac{I}{r_0}\right)^2 - \frac{Z_c+2}{3} T_e \ (eV) , \qquad (4.3)$$

where it is assumed that the deuterons are stripped and so $N_e/\Sigma N_i = (Z_c+2)/3$. This equation also assumes that the carbon and deuterium ions have the same temperature due to their relatively similar masses. At the time when the 500-eV spectrometer signals rise above the noise (30 ns), the current is ~400 kA, and the carbon ionization is $Z_c \approx 5$, giving an estimated ion temperature of $T_i \approx 136$ eV for a solid-fiber radius of ~20 μm. At this time, the densities are high enough for the thermal equilibration time between ions and electrons to be short and so the electron and ion temperatures are expected to be similar.

The plots in Fig. 4.22 show the ion temperature in eV computed from current waveforms of five shots with solid-fiber radii ranging from 10-35 μm. These calculations assumed that the plasma was fully ionized and had an electron temperature of 95 eV. For solid-fiber radii less than 35 μm, the calculated ion

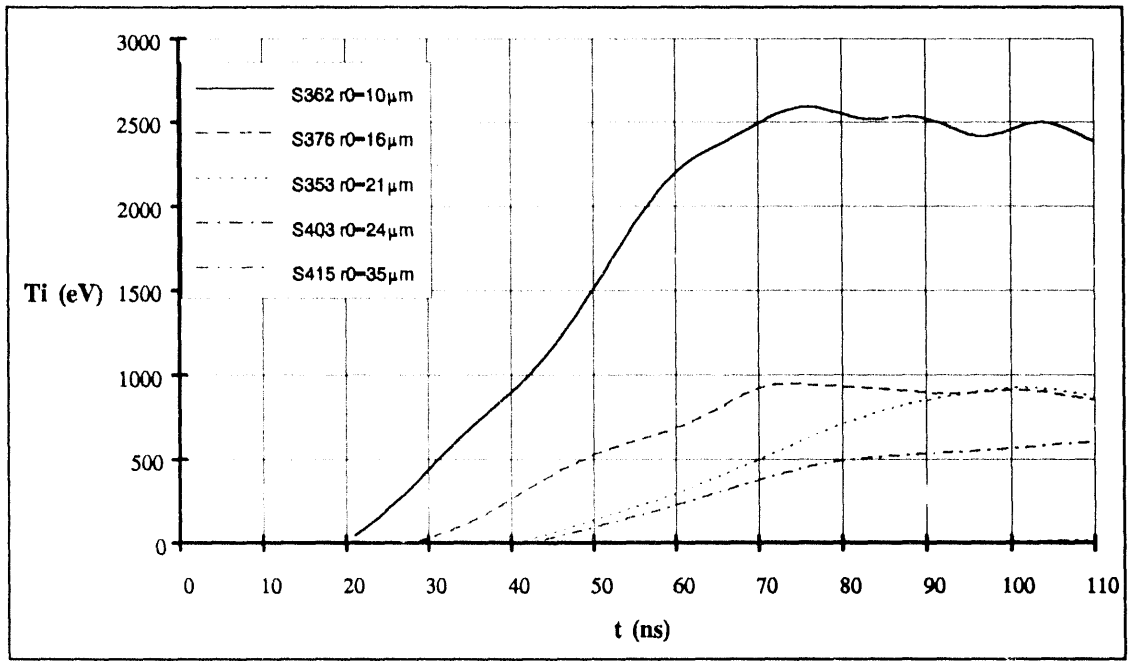

Fig. 4.22 Ion temperature from current for Z_C = 6 and T_i = 95 eV.

temperature greatly exceeds the assumed electron temperature over most of the main current.

The estimated ion temperature being higher than the measured electron temperature may suggest that the ohmic heating of the electrons is not the dominant heating mechanism of the ions. An estimated ion temperature higher than the electron temperature cannot be attributed to a weakness in the assumption of quasi-pressure balance for an expanding plasma because an expanding plasma requires a kinetic pressure greater than the magnetic pressure.

The assumption of quasi-pressure balance is valid to the extent that the plasma expands slower than the thermal velocity of the ions. The thermal velocity of deuterium ions of temperature 140 eV is ~81 km/s and the corresponding velocity for carbon ions is ~33 km/s. The radial velocity measured by circular-schlieren is ~40 km/s. Thus the assumption of quasi-pressure balance seems very marginal, but provides a lower bound on the ion temperature as discussed above.

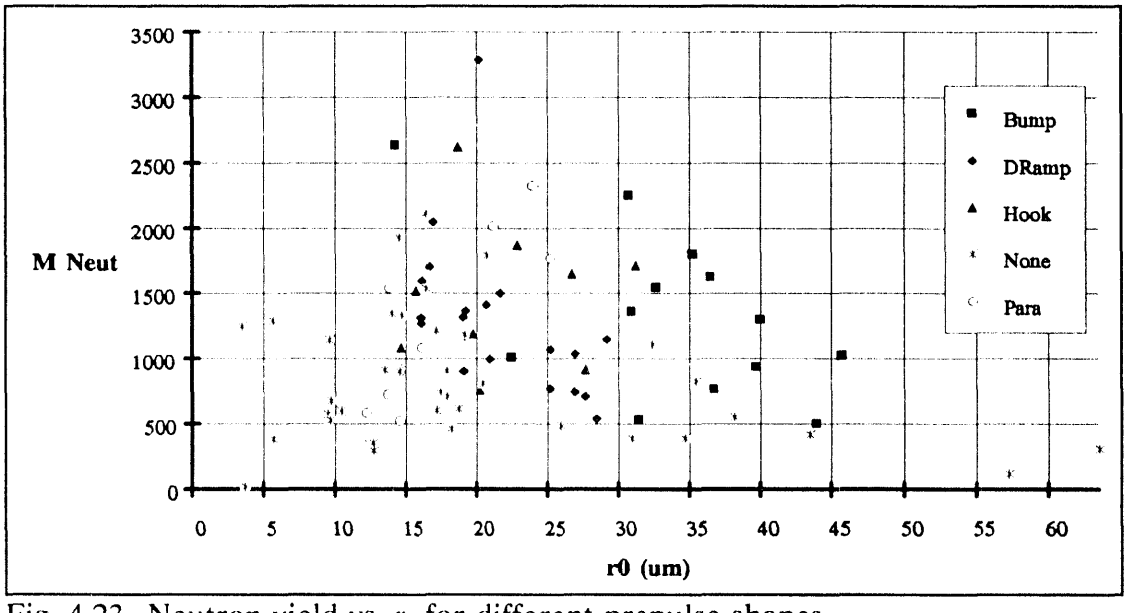

Fig. 4.23 Neutron yield vs. r_0 for different prepulse shapes.

4.5. Neutron Yield Measurements

The scatter plot in Fig. 4.23 shows the neutron production as measured by the silver activation detector for CD_2 fiber shots as a function of the solid-fiber radius. The background count of 159 cpm was subtracted off of the recorded count, and then the count was scaled by 2.6×10^5 neutrons/count. Although there is a large spread in the neutron yield at a given solid-fiber radius, the yield seems to goes through a maximum near a solid-fiber radius of ~22 μm and falls off for larger and smaller solid-fiber radii.

The data points in Fig. 4.23 are segregated according to current prepulse shape in an attempt to see the effect of different prepulses on neutron yield. The points do not seem to divide vertically but there seems to be soft boundaries between prepulse shapes according to the solid-fiber radius.

A shielding plate was added to the water switch in the vertical line before the last nineteen shots were conducted on the machine and is responsible for

many of the larger solid-fiber radii shots having no prepulse. This horizontal distribution of the prepulse shapes indicates a different breakdown voltage for the surface of the fiber according to its radius.

Kies[60] reports that a fiber pinch with a prepulse is less disrupted than one without a prepulse. A less disrupted pinch should produce a higher thermonuclear neutron yield due to its higher ion density. There seems to be a slightly higher neutron yield for bump, hook, and perhaps double ramp prepulses than for no prepulse. It is not clear from the small number of data points that "accidental" prepulses on HDZP-II enhanced the neutron yield.

V ANALYSIS

This chapter compares the data presented in the previous chapter with 0-D simulations of a "stable" model with Joule heating using Spitzer resistivity, an "enhanced Spitzer" model with a multiplier on Spitzer resistivity, and a "turbulent" model with turbulent heating added. In Appendix E, the turbulent heating model is also compared to the stable model with no magnetic confinement.

5.1. Stable Model

The stable model is the first compared with the data presented in the previous chapter. This model is based on Joule heating with Spitzer resistivity, without turbulent heating, and with magnetic confinement. This model predicts a radial collapse of the plasma about halfway into the main current which is not seen in any data presented in the previous chapter. Historically, the failure to observed radial collapse led to the investigation of the other models discussed in this chapter.

5.1.1. Comparison of Stable Model with Circular-Schlieren Results

The 0-D simulation of the stable model, described in Section 2.3, was run using the current waveforms and solid-fiber radii from the shots whose circular-schlieren radii were presented in Section 4.2. The simulation was started at the time and radius of a frame taken near the start of the main current. The initial temperature was set to the Bennett temperature at the starting time.

The simulation assumes that the fiber is fully vaporized (no solid core) and that the plasma electron temperature is high enough for Spitzer resistivity to be valid. The simulation was not started earlier than 15 ns before the start of the main current. For Spitzer resistivity to be valid, the simulation was started after the current has risen above 30 kA. The Bennett temperature for CD_2 at this

TABLE VI. Initial conditions for 0-D simulation of circular-schlieren shots: shot number, solid-fiber radius, starting time, starting radius, starting radial velocity, and starting Bennett temperature.

Bin	Shot	r_0 (μm)	t_1 (ns)	r_1 (μm)	v_1 (m/s)	T_B (eV)
1	362	10.25	-6	90	9400	2
1	379	13.75	3	20	5800	7
1	373	14.50	9	225	1000	17
1	377	14.50	-5	196	8100	3
2	367	16.00	-7	133	2800	7
2	370	16.00	-10	338	4600	7
2	374	16.00	-10	193	6500	3
2	376	16.25	-6	201	4800	3
3	408	19.00	7	247	32000	6
3	353	20.50	-6	98	200	4
3	409	20.75	-8	191	4000	5
4	403	23.75	-5	130	1500	5
4	411	26.75	-2	226	3700	5
4	386	27.50	-15	255	4200	3
4	385	31.00	6	230	0	3
5	415	34.50	4	247	16000	2
5	372	35.00	22	400	7700	12
5	383	36.25	19	500	0	8
5	405	36.50	27	250	0	13
6	382	39.75	15	800	0	6
6	423	43.25	-6	228	19000	2
6	416	57.00	9	427	12000	3

current is

$$T_B(30kA, 20\mu m) = \frac{\mu_0}{8\pi^2 e\ 3.75\times10^{28}} \frac{I^2}{(5+Z_c)\, r_0^2} \approx 1\ eV \qquad (5.1)$$

where the radius of the solid fiber is assumed to be $r_0 \approx 20\ \mu$m. In the case of a prepulse large enough to produce a constant radius vs. time into the main current, the simulation is started at the last time this constant radius is recorded.

The plots in Fig. 5.1, Fig. 5.2, Fig. 5.3, Fig. 5.4, Fig. 5.5, and Fig. 5.6 compare the results of the 0-D simulation of the stable model with the rms radii presented in the same six bins of solid-fiber radius used to display the data in Section 2.3. The simulation was only run for shots that have at least two measured radii after the chosen starting time; this is because the early time behavior is affected by the initial temperature and radial velocity chosen.

An important heating term, not included in the stable theory, is suggested by the radial collapse predicted by the simulation after 25 ns into the main current rather than the rapid expansion measured by the circular-schlieren diagnostic.

The radial collapse of the simulated plasma occurs earlier for smaller solid-fiber radii. The initial expansion of the measured and simulated plasma radii seems faster for smaller solid-fiber radii.

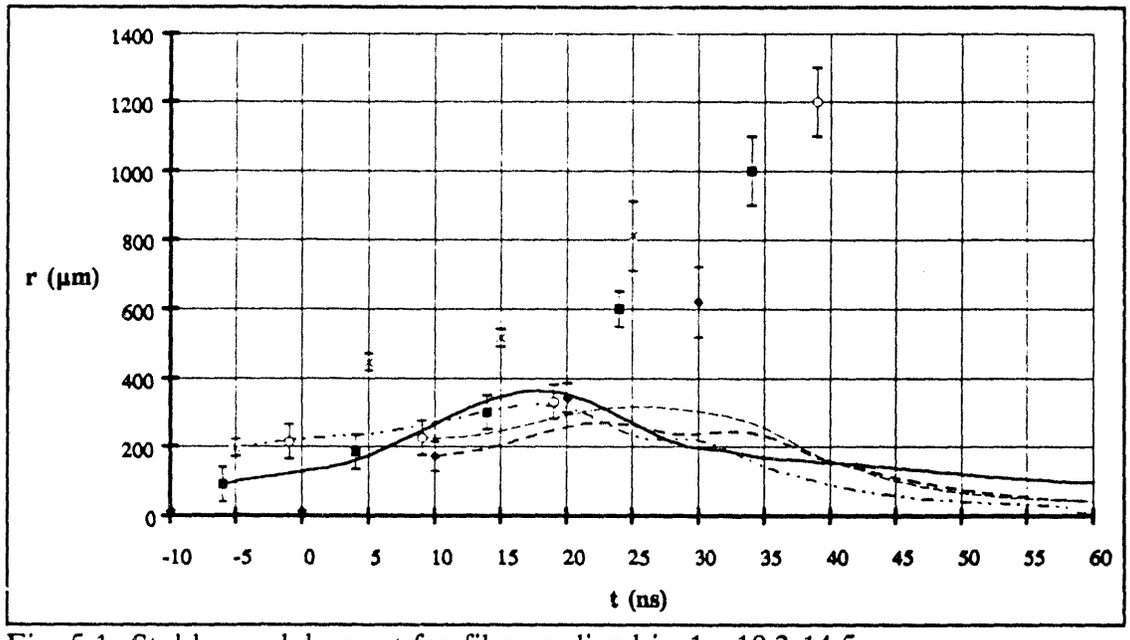

Fig. 5.1 Stable model r vs. t for fiber-radius bin 1: 10.3-14.5 μm.

Legend: (■) shot 362, (♦) shot 379, (O) shot 373, and (x) shot 377.

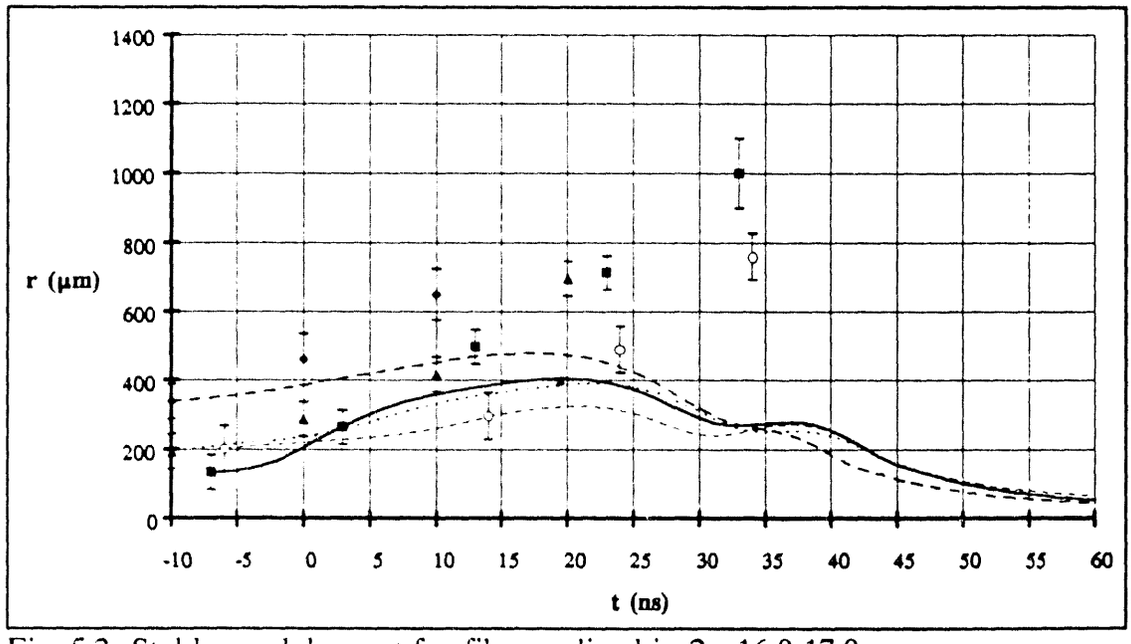

Fig. 5.2 Stable model r vs. t for fiber-radius bin 2: 16.0-17.0 μm.

Legend: (■) shot 367, (♦) shot 370, (▲) shot 374, and (O) shot 376.

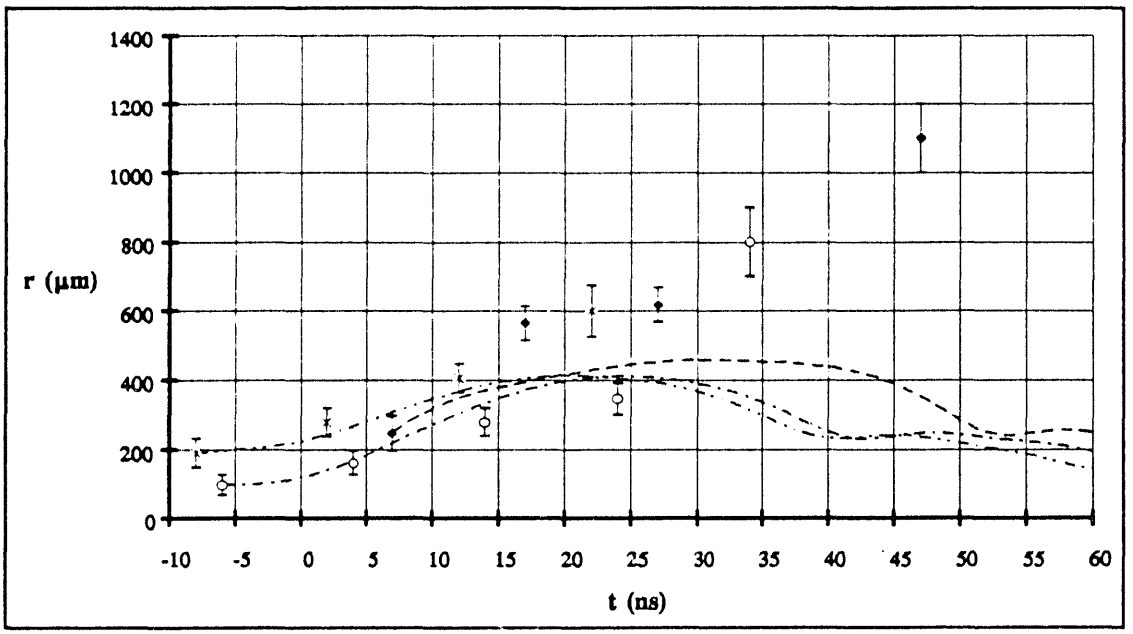

Fig. 5.3 Stable model r vs. t for fiber-radius bin 3: 18.5-20.8 μm.

Legend: (♦) shot 408, (O) shot 353, and (x) shot 409.

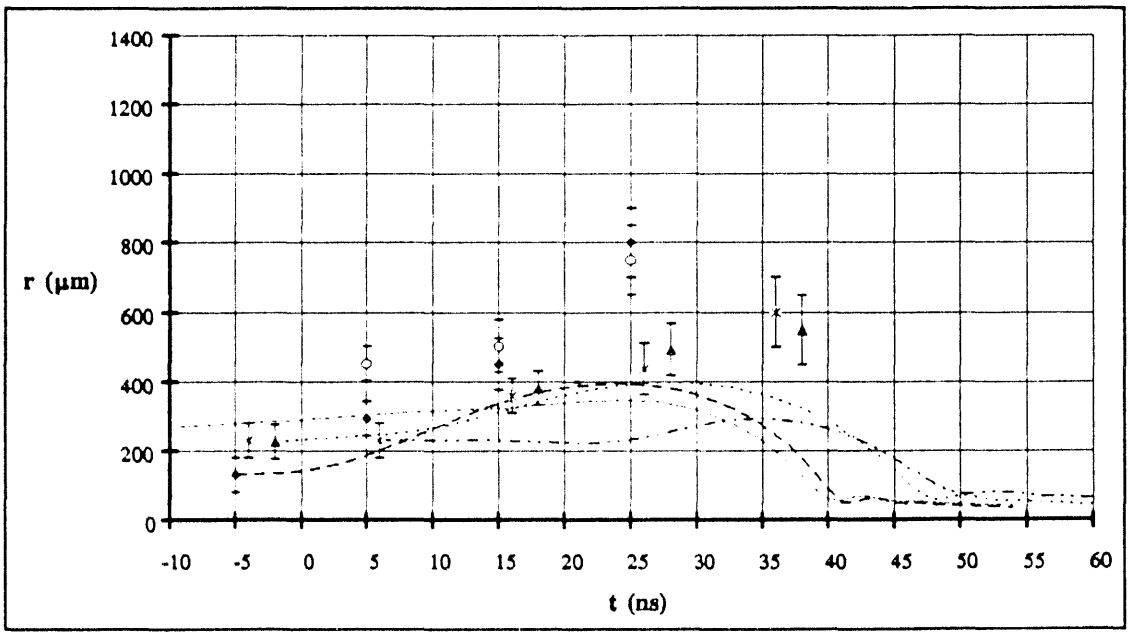

Fig. 5.4 Stable model r vs. t for fiber-radius bin 4: 22.3-31.0 μm.

Legend: (♦) shot 403, (▲) shot 411, (O) shot 386, and (x) shot 385.

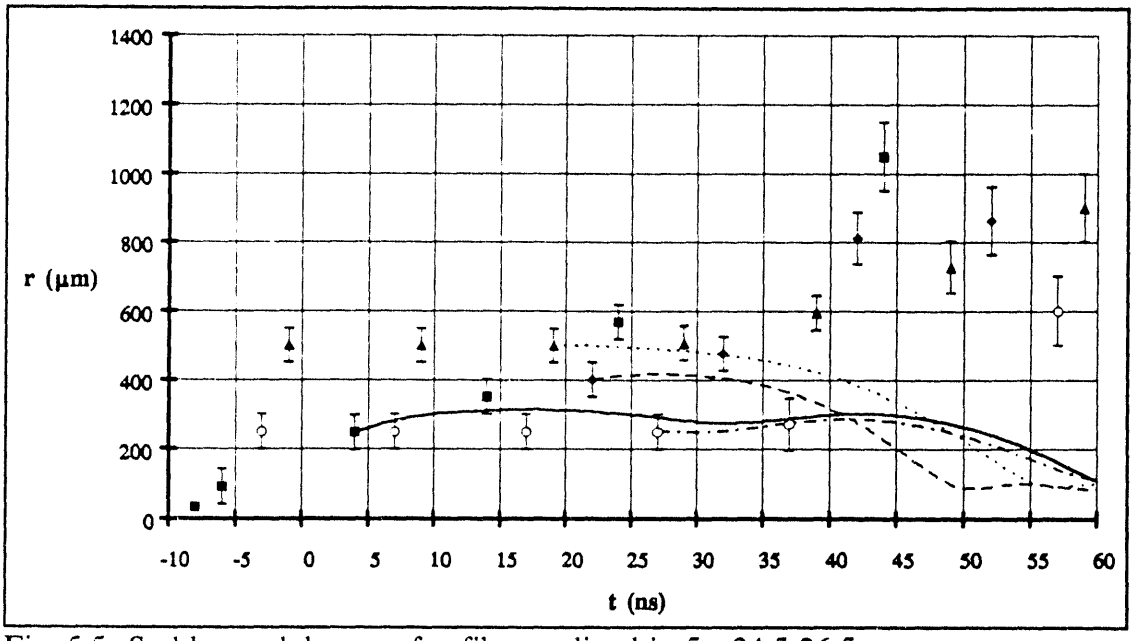

Fig. 5.5 Stable model r vs. t for fiber-radius bin 5: 34.5-36.5 μm.

Legend: (■) shot 415, (♦) shot 372, (▲) shot 383, and (O) shot 405.

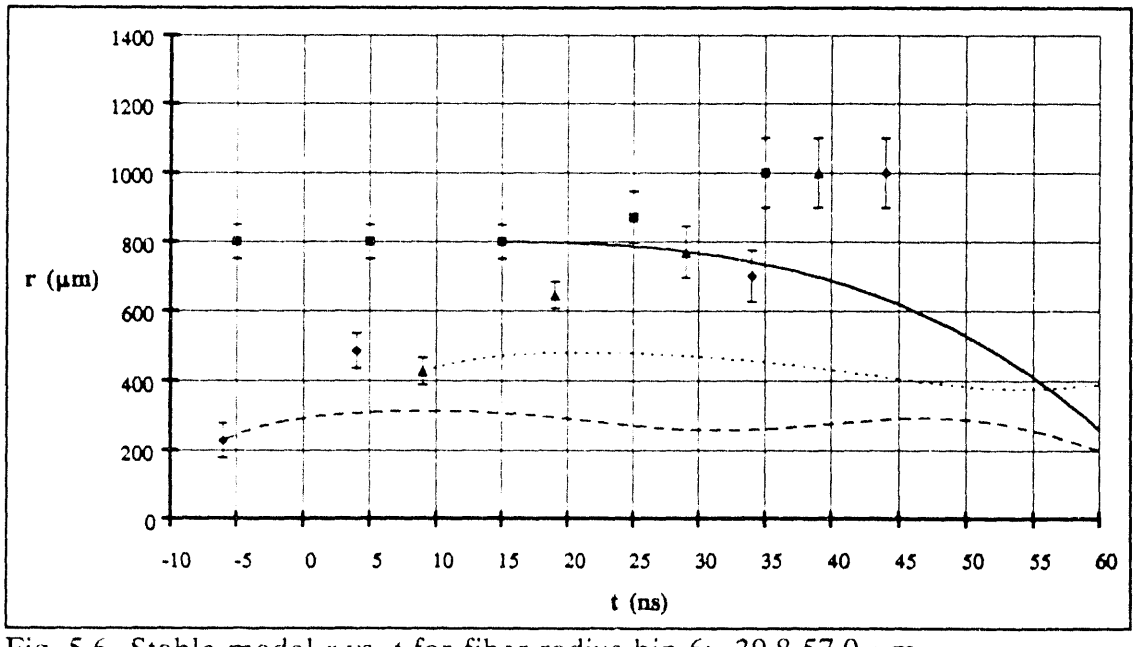

Fig. 5.6 Stable model r vs. t for fiber-radius bin 6: 39.8-57.0 μm.

Legend: (■) shot 382, (♦) shot 423, and (▲) shot 416.

5.1.2. Comparison of Stable Model with T_e Data

The plots in Fig. 5.7 show the electron temperature vs. time curves generated by the runs of the stable model simulation described in the previous section. The shaded area encloses the electron temperature measurements for the full range of solid-fiber radii 3.5-38 μm described in Section 4.4.

One electron temperature curve from each solid-fiber radius bin is plotted to give a sense of the variation with solid-fiber radius predicted by the stable model. Since all of the electron temperature data were collected on shots with no current prepulse, the simulated curve with the smallest prepulse was selected from each bin for comparison with the electron temperature. For the stable model, the peak electron temperature decreases monotonically with increasing

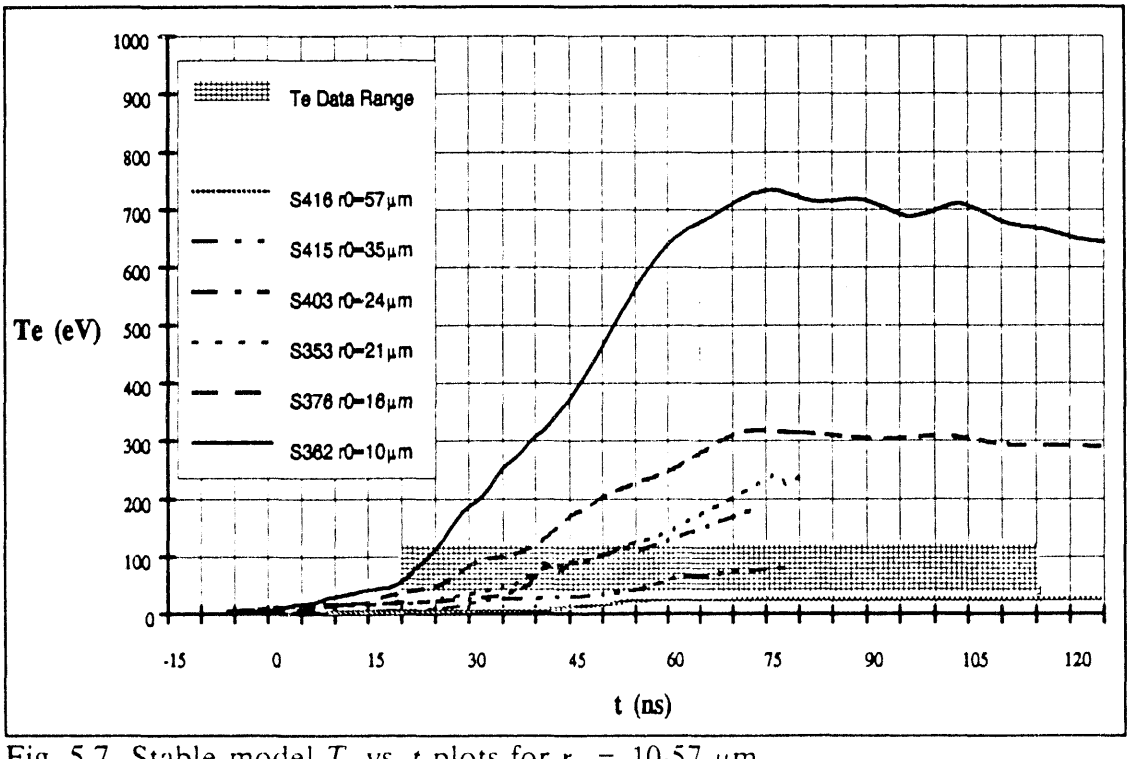

Fig. 5.7 Stable model T_e vs. t plots for r_0 = 10-57 μm.

solid-fiber radius, while the electron temperature data shows almost no dependence on the solid-fiber radius.

5.1.3. Comparison of Stable Model with T_i Data

The plasma stays dense enough during the runs of the stable model that the ions remain in thermal equilibrium with the electrons. The plots in Fig. 5.7 also show the ion temperatures. The ion temperatures predicted by the stable model are about three times smaller than required by Bennett equilibrium, see Fig. 4.22; this is why the simulated pinch collapses. This is an artifact of the term that was added to the equations to prevent radial collapse. Without this term, the simulation would collapse toward zero radius and all temperatures would tend toward infinity.

5.1.4. Comparison of Stable Model with X-Ray Data

The magnitude of the x-ray signals provides a comparison between the models. The plots in Fig. 5.8 show the simulated 500-eV x-ray spectrometer channel signals for the same subset of shots used in the previous section for comparison with the electron temperature.

The x-ray spectrometer signal is strongly dependent on the density and temperature of the plasma. The simulated x-ray signal gets very large at the time that the radius collapses for the stable model. For comparison with the simulated results of the other models, it must be noted that the vertical scale on this plot for the stable model is ten times as large as that of those for the other models presented in this chapter. The x-ray signals predicted by this model are over a hundred times as large as the data presented in Section 4.4.

5.1.5. Comparison of Stable Model with Neutron Data

The neutron yield predicted by the stable model is strongly dependent on how far the plasma is allowed to radially collapse before the simulation stops the collapse to prevent numerical difficulties. Without this numerical barrier, the plasma would achieve near infinite density and temperature, and all available deuterium fuel would be consumed almost instantly. The neutron yield for this model can then be set to half the number of deuterium atoms in the fiber, $neut \approx 3.8\times10^{28}\ \ell\pi r_0^2 \approx 2.4\times10^{18}$ for solid-fiber radius r_0 = 20 μm and length ℓ = 5 cm.

5.2. Enhanced Spitzer Model

The most direct way to change the stable model to make it more consistent with the data is to increase the Spitzer resistivity of the plasma. The simulation

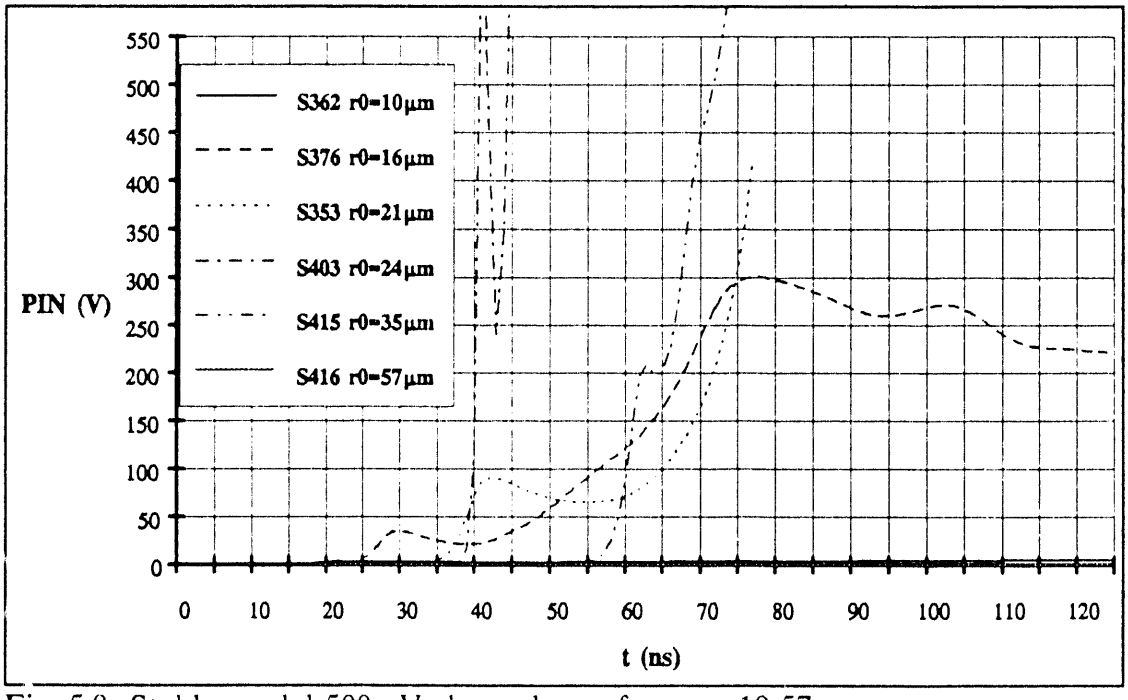

Fig. 5.8 Stable model 500-eV channel vs. t for r_0 = 10-57 μm.

computes an "enhanced Spitzer" model by using a constant multiplier to the Spitzer resistivity calculation.. The calculations used a multiplier of 10 unless otherwise stated.

5.2.1. Comparison of Enhanced Spitzer Model with Circular-Schlieren Results

The plots in Fig. 5.9, Fig. 5.10, Fig. 5.11, Fig. 5.12, Fig. 5.13, and Fig. 5.14 compare the measured rms radii with the results of the enhanced Spitzer model simulation. The multiplier of 10 is large enough to prevent a radial collapse of the plasma. Even though this model usually over-shoots the first radius point in each sequence and reaches a larger radius than the stable model, it levels off at radii smaller than measured by the circular-schlieren diagnostic. Despite the lack of a measurable radius at later times, the circular schlieren shows that the plasma continues to expand beyond a radius of 1 mm, and does not collapse during the main current.

A smaller multiplier would fit the earlier data points better and a larger multiplier would fit the later data points better; thus the chosen value of 10 is a good compromise that shows that no single multiplier can be used to fit all of the data points. The failure of the enhanced Spitzer model is most obvious for the smaller solid-fiber radii where it most over-shoots the initial points and under-shoots the later points.

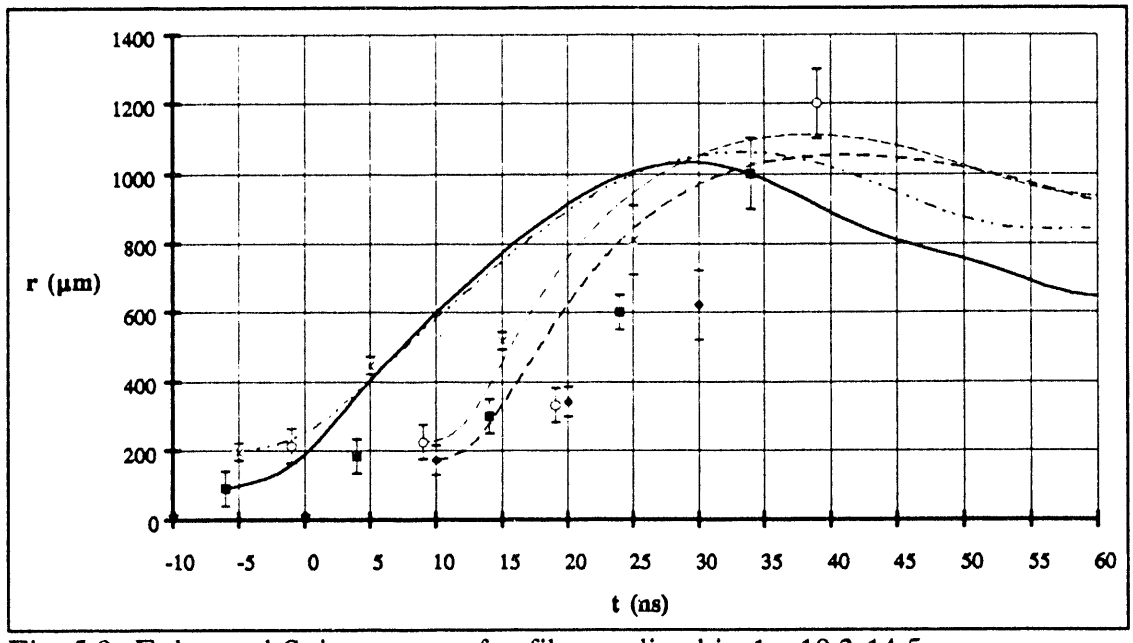

Fig. 5.9 Enhanced Spitzer r vs. t for fiber-radius bin 1: 10.3-14.5 μm.
Legend: (■) shot 362, (♦) shot 379, (O) shot 373, and (x) shot 377.

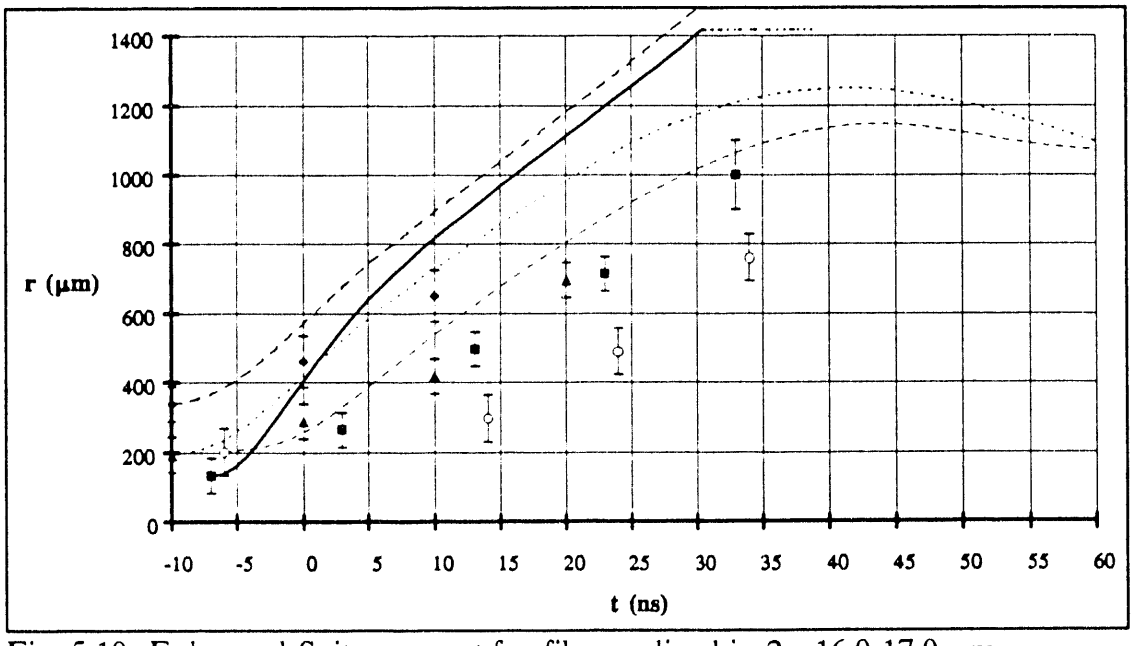

Fig. 5.10 Enhanced Spitzer r vs. t for fiber-radius bin 2: 16.0-17.0 μm.
Legend: (■) shot 367, (♦) shot 370, (▲) shot 374, and (O) shot 376.

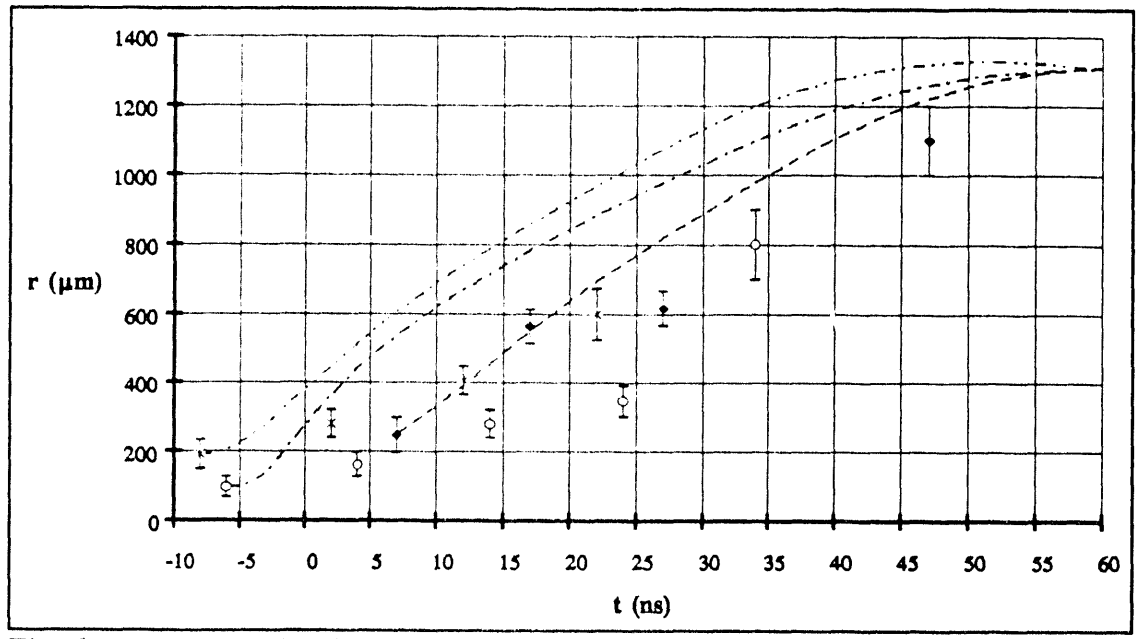

Fig. 5.11 Enhanced Spitzer r vs. t for fiber-radius bin 3: 18.5-20.8 μm.
Legend: (♦) shot 408, (O) shot 353, and (x) shot 409.

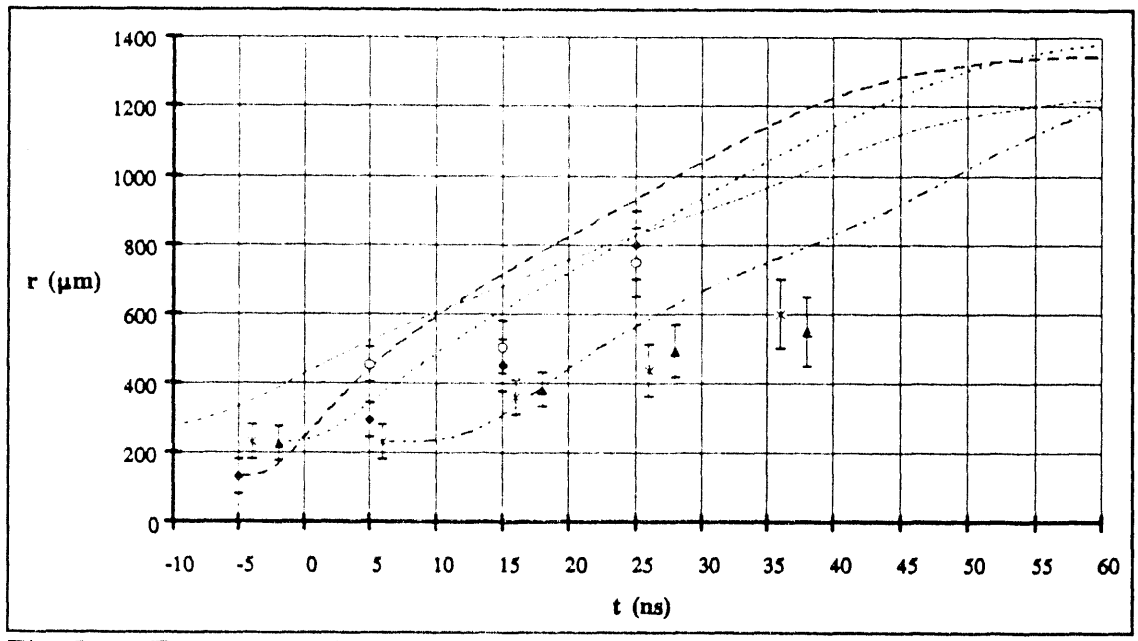

Fig. 5.12 Enhanced Spitzer r vs. t for fiber-radius bin 4: 22.3-31.0 μm.
Legend: (♦) shot 403, (▲) shot 411, (O) shot 386, and (x) shot 385.

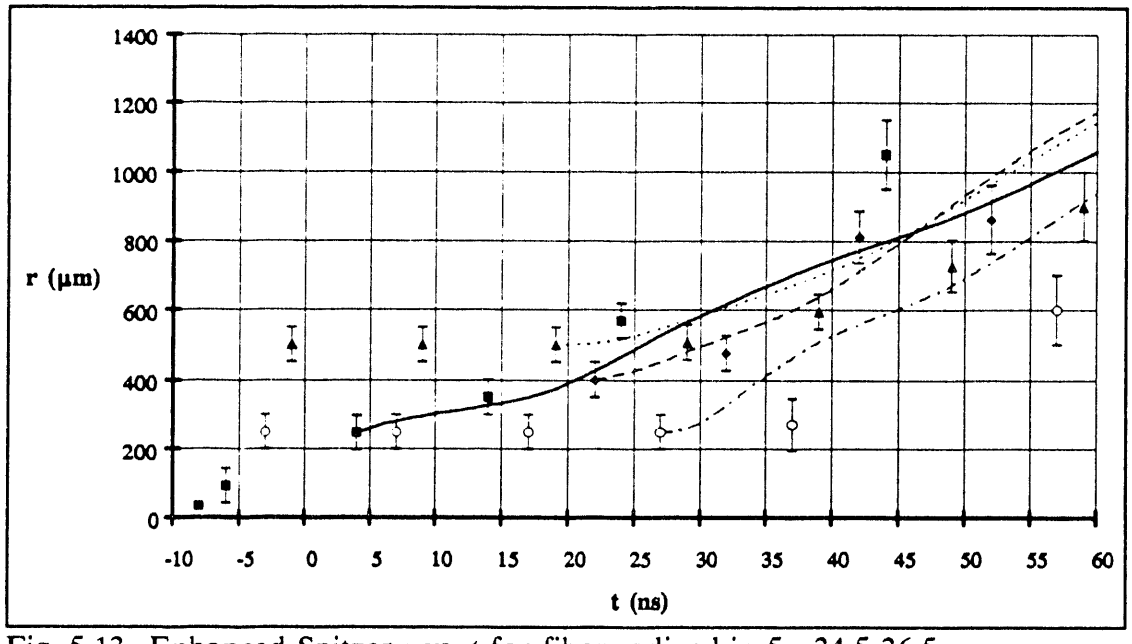

Fig. 5.13 Enhanced Spitzer r vs. t for fiber-radius bin 5: 34.5-36.5 μm.

Legend: (■) shot 415, (♦) shot 372, (▲) shot 383, and (O) shot 405.

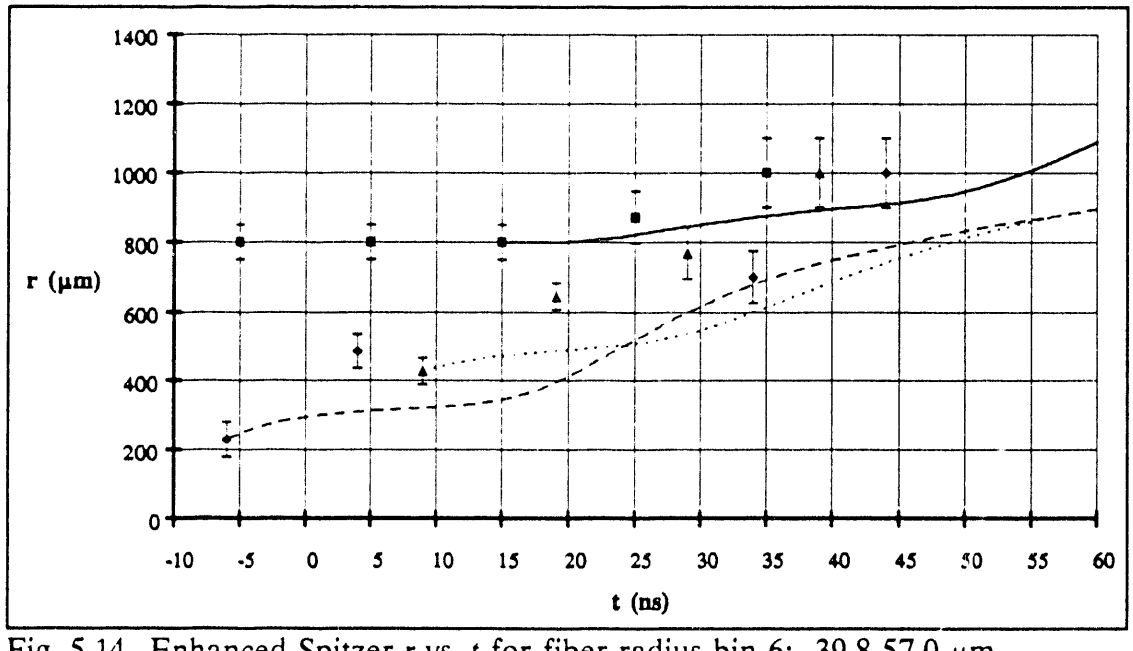

Fig. 5.14 Enhanced Spitzer r vs. t for fiber-radius bin 6: 39.8-57.0 μm.

Legend: (■) shot 382, (♦) shot 423, and (▲) shot 416.

5.2.2. Comparison of Enhanced Spitzer Model with T_e Data

The electron temperatures produced by these enhanced Spitzer resistivity simulations are shown in Fig. 5.15. The same minimum prepulse shots were selected from each solid-fiber radius bin as those used to compare the stable model to the electron temperature data.

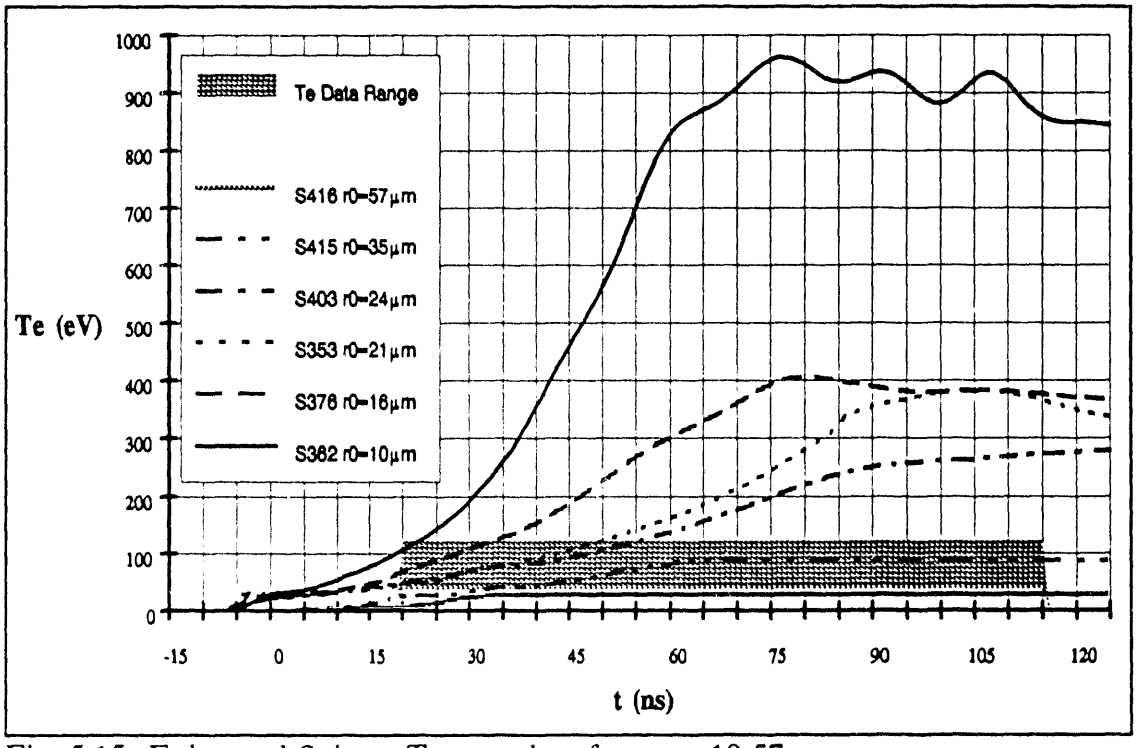

Fig. 5.15 Enhanced Spitzer T_e vs. t plots for r_0 = 10-57 μm.

Like the stable model the peak electron temperature decreases monotonically with increasing solid-fiber radius for the enhanced Spitzer model. The enhanced Spitzer model reaches higher electron temperatures sooner than in the stable model. For smaller solid-fiber radii, the electron temperatures predicted by the enhanced Spitzer model are much higher than what was measured.

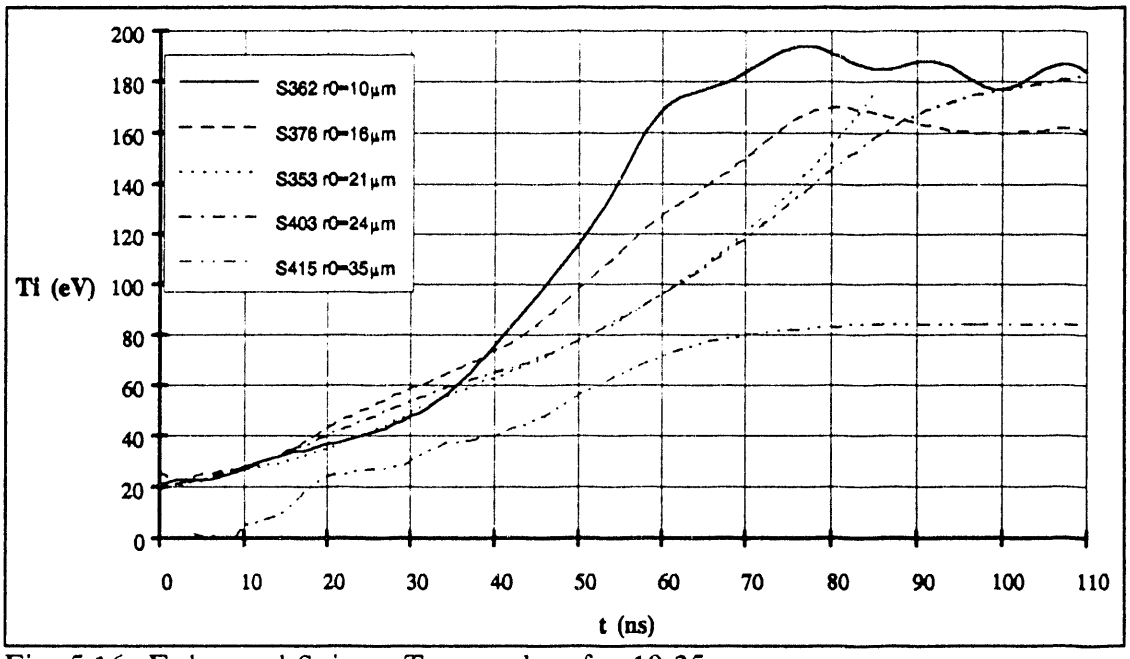

Fig. 5.16 Enhanced Spitzer T_i vs. t plots for 10-35 μm.

5.2.3. Comparison of Enhanced Spitzer Model with T_i Data

The plots in Fig. 5.16 show the ion temperatures predicted for runs of the enhanced Spitzer model. These predicted ion temperatures are about a factor of ten smaller than the data presented is Fig. 4.22. The ion temperature is depressed by an adiabatic expansion driven by the hot electrons. At the lower densities predicted by the enhanced Spitzer model, the thermal equilibration times become long and the electrons do not heat the ions effectively.

5.2.4. Comparison of Enhanced Spitzer Model with X-Ray Data

The plots in Fig. 5.17 show the simulated 500-eV x-ray spectrometer channel signal for the same subset of shots used in the previous section for comparison with the electron temperature.

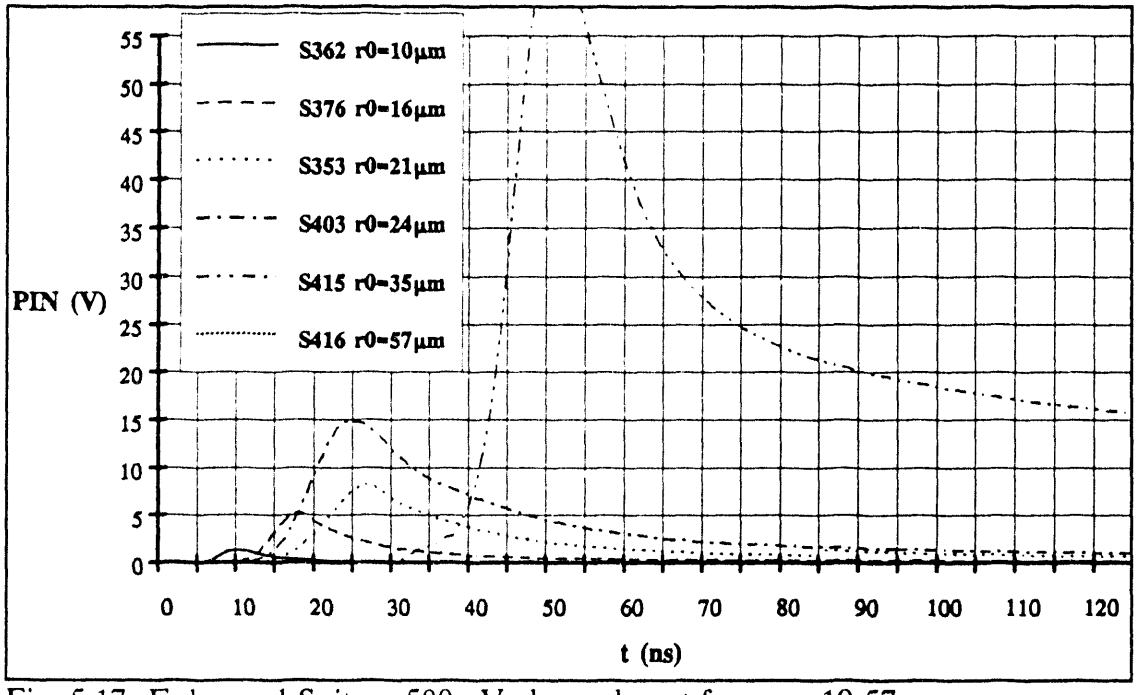

Fig. 5.17 Enhanced Spitzer 500-eV channel vs. t for r_0 = 10-57 μm.

The sharp rise in the spectrometer signals is coincident in the simulation with the sudden increase in fully ionized carbon ions and an associated increase in electron temperature. The slow fall-off in the signals is due to the slow expansion of the plasma at nearly constant electron temperatures, with the exception of shot 415 which predicts a radial collapse. The calculated peak voltage of the signals is about a factor of ten larger than the data for larger solid-fiber radii and about a factor of three smaller than the data for smaller solid-fiber radii. The peaks of the signals of the larger radii shots are predicted to be larger than those of the smaller radii shots, which is not consistent with the data presented in Section 4.4. The simulated signals do not have the second "hump" seen in the data.

5.2.5. Comparison of Enhanced Spitzer Model with Neutron Data

The plots in Fig. 5.18 show the neutron yield as a function of solid-fiber radius predicted by the enhanced Spitzer model for multipliers of 2, 3, and 5 plotted over the measured neutron yields. Each point on the curves was run on the same current waveform which had no prepulse and which had a peak current of $I_{peak} \approx 800$ kA. The figure shows that the enhanced Spitzer multiplier of 10 used in fitting the radius data above does not generate a detectable number of neutrons.

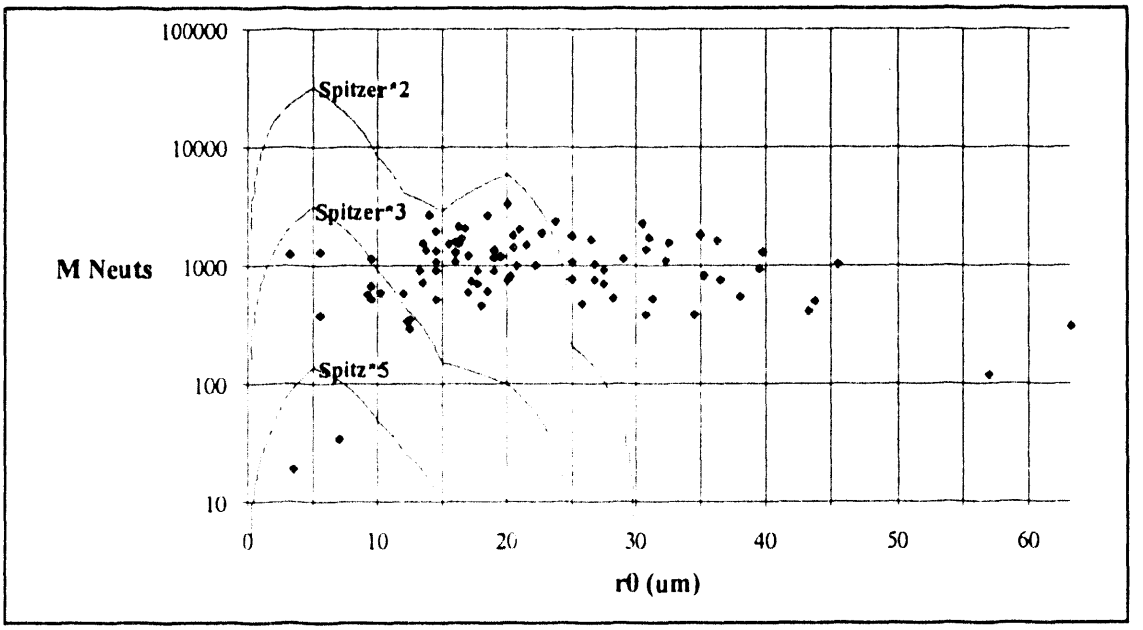

Fig. 5.18 Neutron yield vs. r_0 for Spitzer multipliers of 2, 3, and 5.

The simulated neutron yields for an enhanced Spitzer multiplier of 5 or greater never reach the level of the majority of the data points of around 10^9 neutrons. The curves for multipliers of 2 and 3 only intersect the data for very narrow regions of solid-fiber radii, falling sharply as the radii becomes large or small. The neutron yields for larger radii cannot be explained by thermonuclear reactions based on an enhanced Spitzer model with any reasonable multiplier.

5.3. Turbulent Heating Model

This model is identical to the stable model with the addition of the turbulent heating term described in Section 2.4. This term directly heats the ions unlike Joule heating that heats the electrons which then thermalize with the ions. This permits the ion temperature to exceed the electron temperature in the plasma.

5.3.1. Comparison of Turbulent Heating Model with Circular-Schlieren Results

The plots in Fig. 5.19, Fig. 5.20, Fig. 5.21, Fig. 5.22, Fig. 5.23, and Fig. 5.24 compare the results of the turbulent heating simulation with the measured rms radii. The measured expansion is consistent with this model over a wide range of initial solid-fiber radii. The increase in radial velocity at ~20 ns into the main current occurred when the turbulent heating term becomes larger than Joule heating based on Spitzer resistivity.

This fast radial expansion observed in the data and predicted by the turbulent heating model at later times is clearly different from the collapse predicted by the stable model and the leveling off of the enhanced Spitzer model.

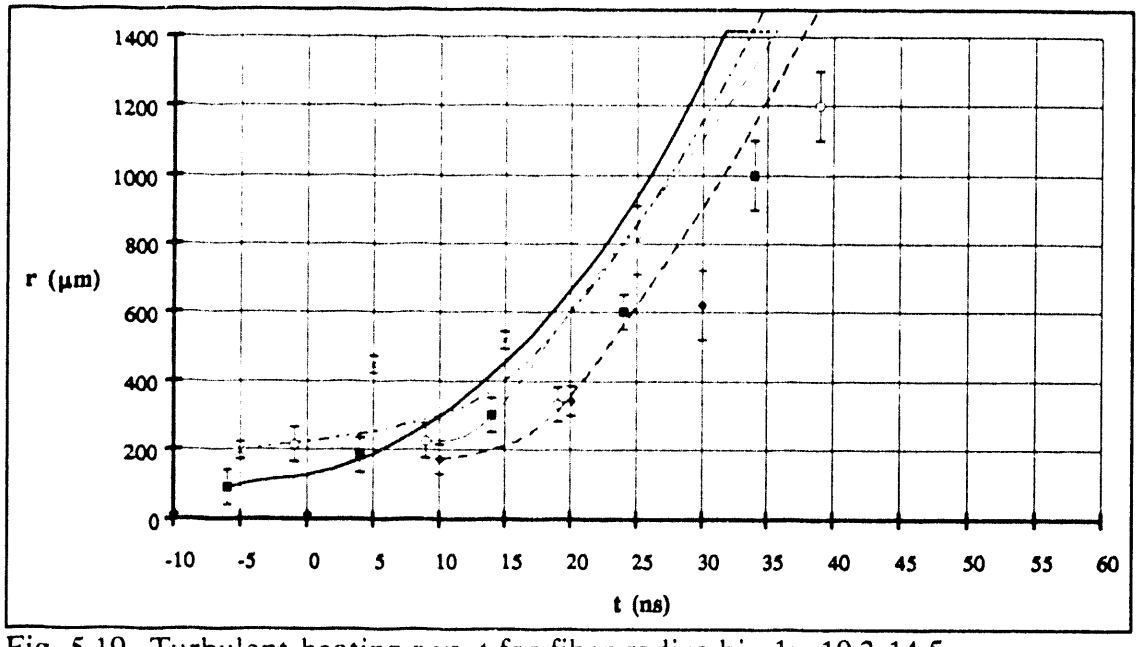

Fig. 5.19 Turbulent heating r vs. t for fiber-radius bin 1: 10.3-14.5 μm.
Legend: (■) shot 362, (♦) shot 379, (O) shot 373, and (x) shot 377.

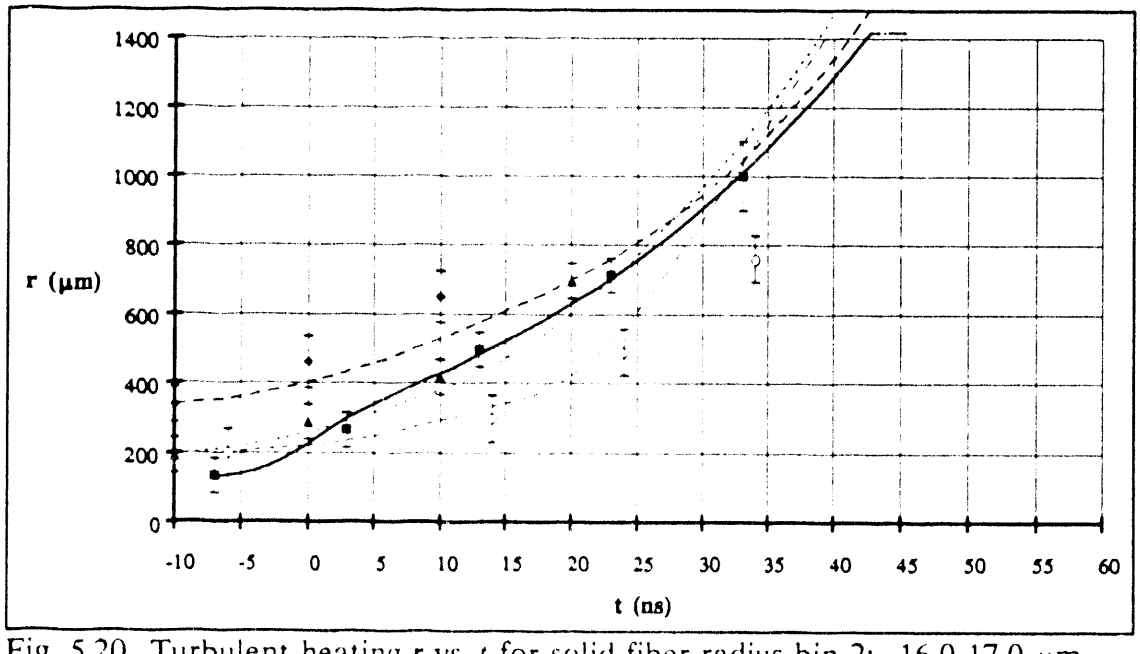

Fig. 5.20 Turbulent heating r vs. t for solid-fiber-radius bin 2: 16.0-17.0 μm.
Legend: (■) shot 367, (♦) shot 370, (▲) shot 374, and (O) shot 376.

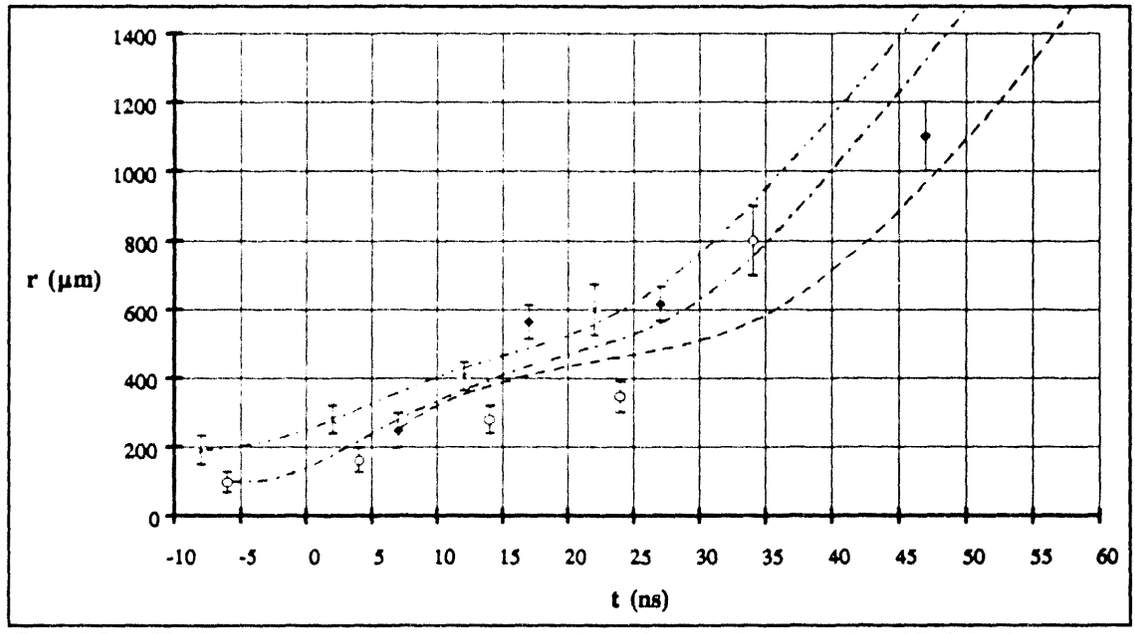

Fig. 5.21 Turbulent heating r vs. t for solid-fiber-radius bin 3: 18.5-20.8 μm.
Legend: (♦) shot 408, (O) shot 353, and (x) shot 409.

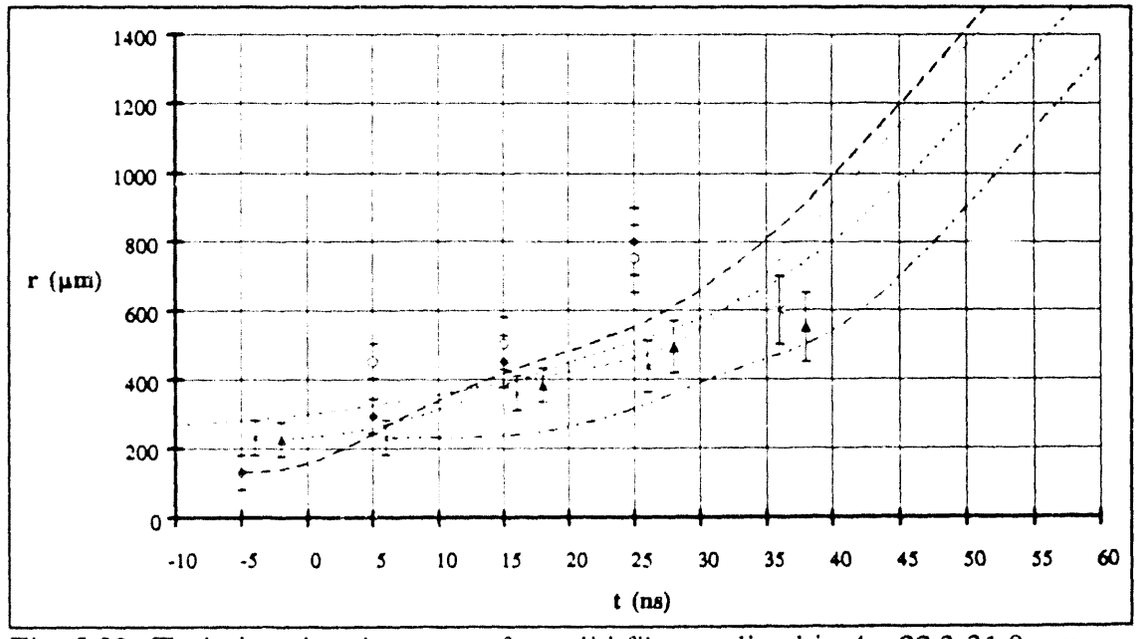

Fig. 5.22 Turbulent heating r vs. t for solid-fiber-radius bin 4: 22.3-31.0 μm.
Legend: (♦) shot 403, (▲) shot 411, (O) shot 386, and (x) shot 385.

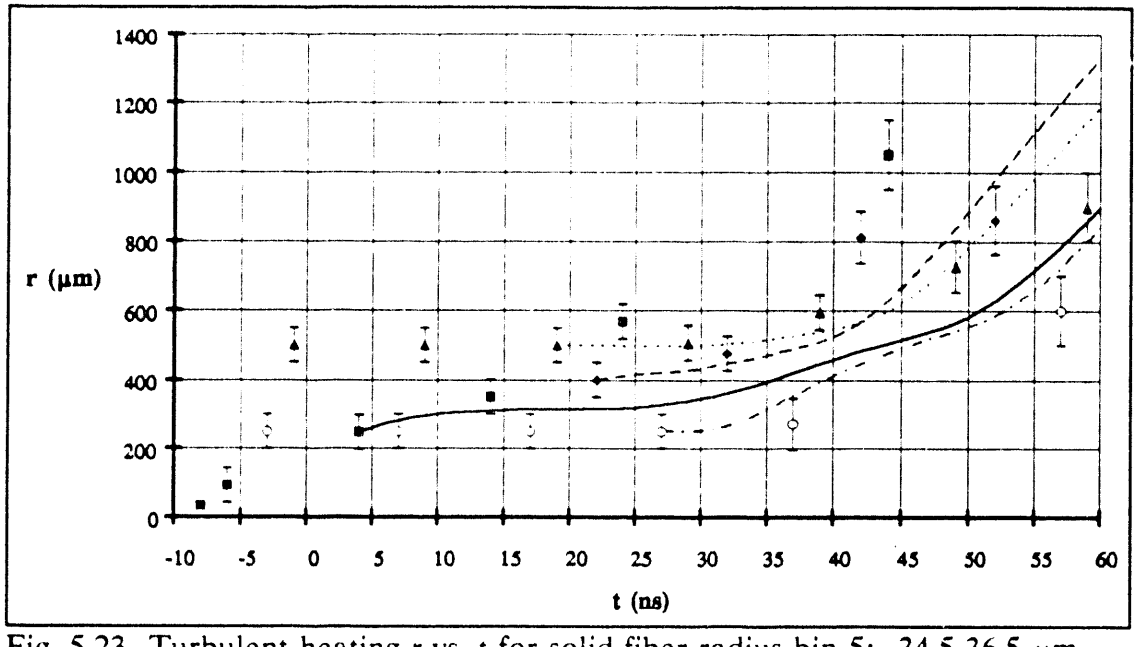

Fig. 5.23 Turbulent heating r vs. t for solid-fiber-radius bin 5: 34.5-36.5 μm.

Legend: (■) shot 415, (♦) shot 372, (▲) shot 383, and (O) shot 405.

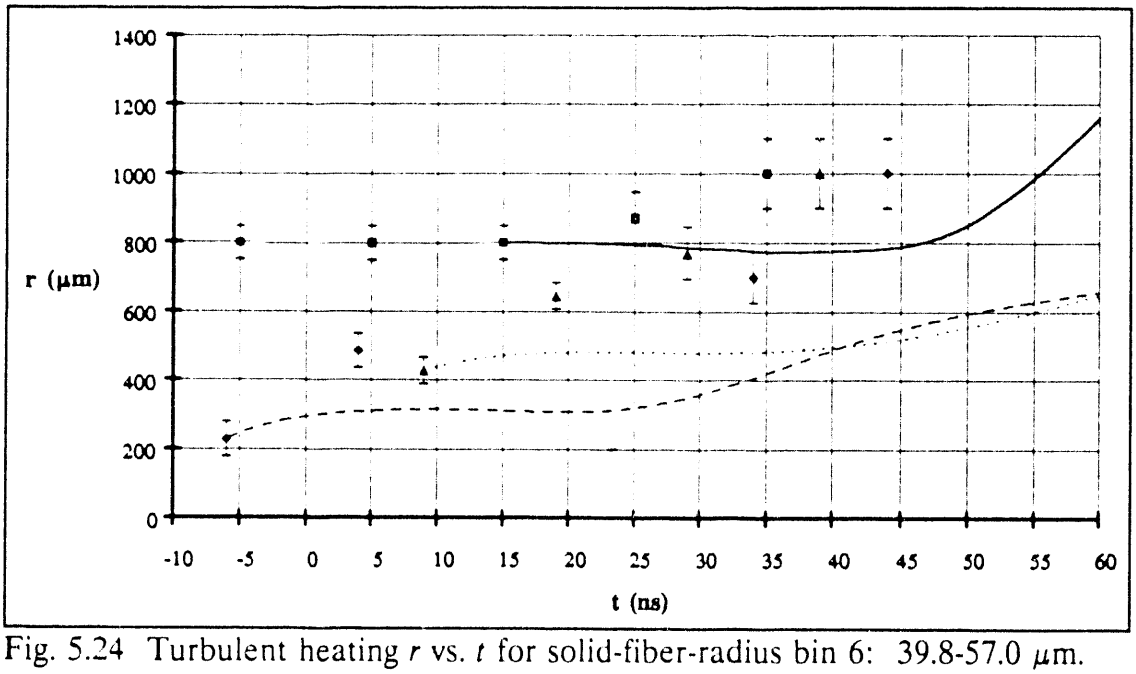

Fig. 5.24 Turbulent heating r vs. t for solid-fiber-radius bin 6: 39.8-57.0 μm.

Legend: (■) shot 382, (♦) shot 423, and (▲) shot 416.

5.3.2. Comparison of Turbulently Heated Model with T_e Data

The plots in Fig. 5.25 show the electron temperatures predicted by the turbulent heating model. Unlike the other models discussed so far whose peak electron temperatures decrease monotonically with increasing solid-fiber radius, the peak electron temperature of the turbulently heated model goes through a maximum at a solid-fiber radius of $r_0 \approx 22$ μm. This is more consistent with the data which has little variation over the range of solid-fiber radii. Although the electron temperatures predicted by the turbulent heating model are above the data range for smaller solid-fiber radii and below for larger solid-fiber radii, all of the temperatures remain very close to the data range. The vertical scale of the plot of the simulation electron temperature is five times smaller than that for the stable and enhanced Spitzer models.

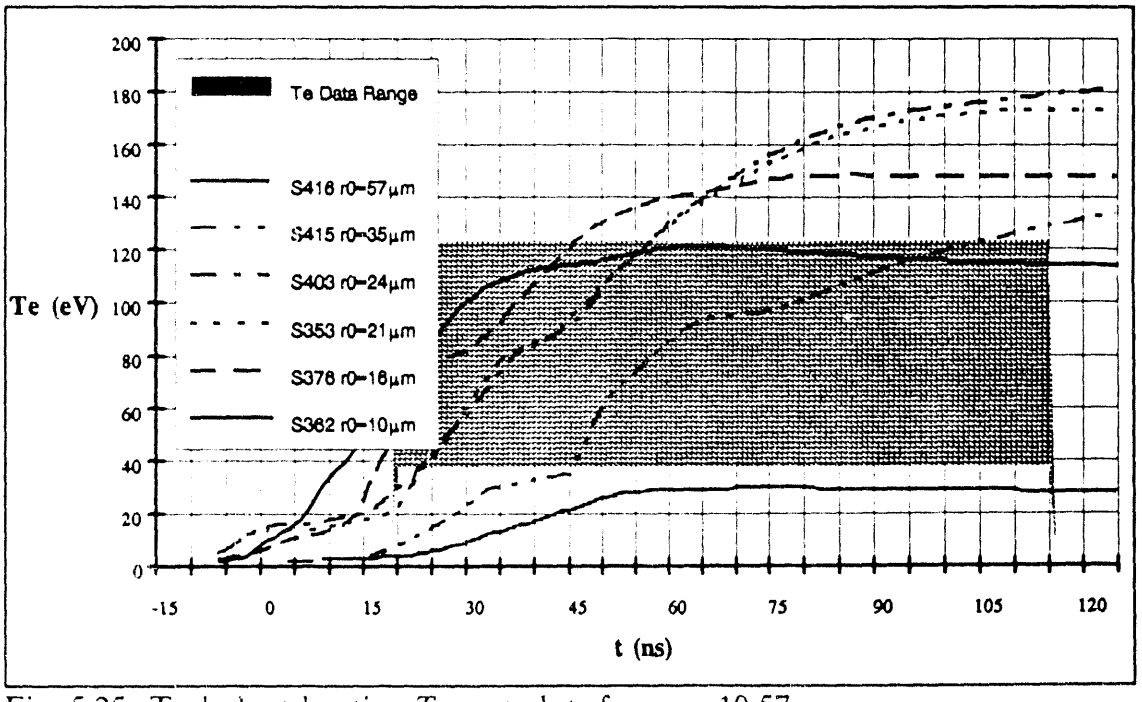

Fig. 5.25 Turbulent heating T_e vs. t plots for r_0 = 10-57 μm.

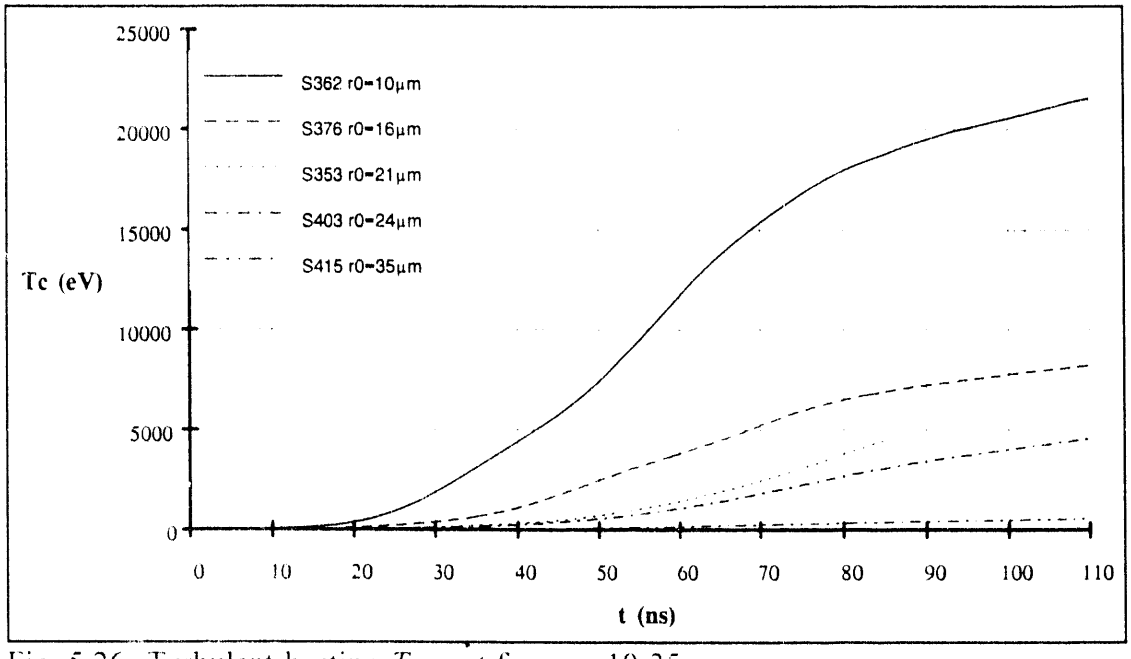

Fig. 5.26 Turbulent heating T_e vs. t for r_0 = 10-35 μm.

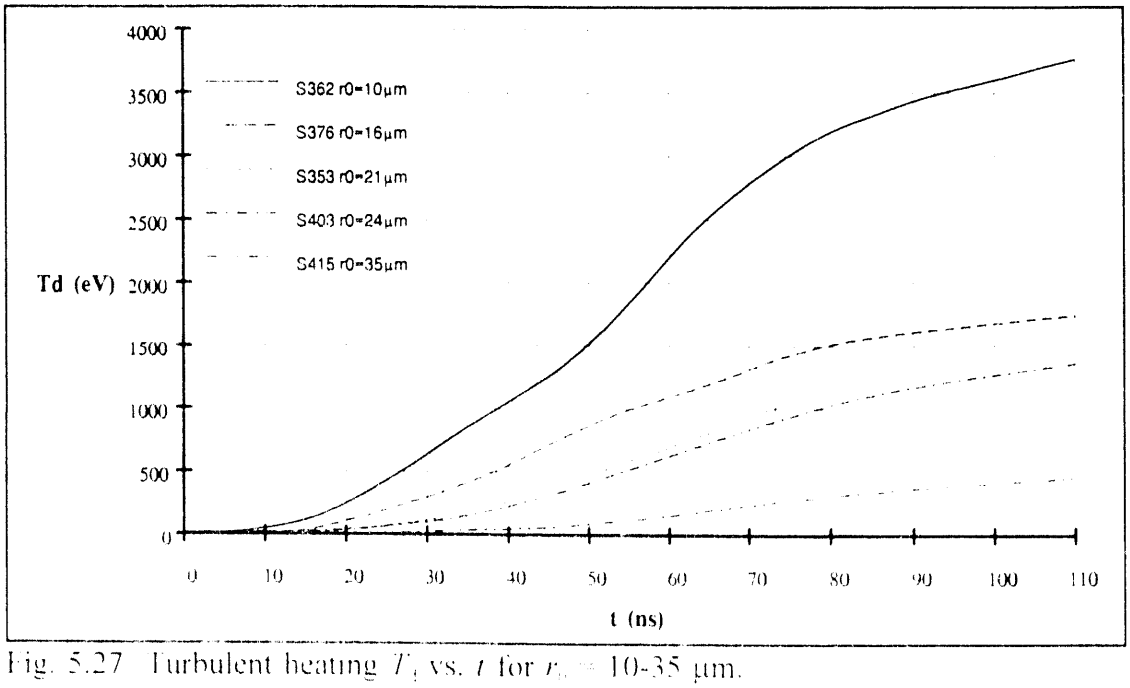

Fig. 5.27 Turbulent heating T_i vs. t for r_0 = 10-35 μm.

5.3.3. Comparison of Turbulently Heated Model with T_i Data

The plots in Fig. 5.26 and Fig. 5.27 show the carbon and deuterium temperatures predicted by the turbulently heated model. These predicted carbon temperatures are about a factor of ten larger than the data presented in Fig. 4.22. The data presented in chapter 4 assumed Bennett equilibrium and can be taken as a lower bound on the ion temperature of an expanding plasma. The turbulent heating model correctly predicts an ion temperature which exceeds that required for Bennett equilibrium and the predicted ion temperature should not be expected to equal this lower boundary.

5.3.4. Comparison of Turbulently Heated Model with X-Ray Data

The plots in Fig. 5.28 show the simulated 500-eV x-ray spectrometer channel signal for the same subset of shots used in the previous section for comparison

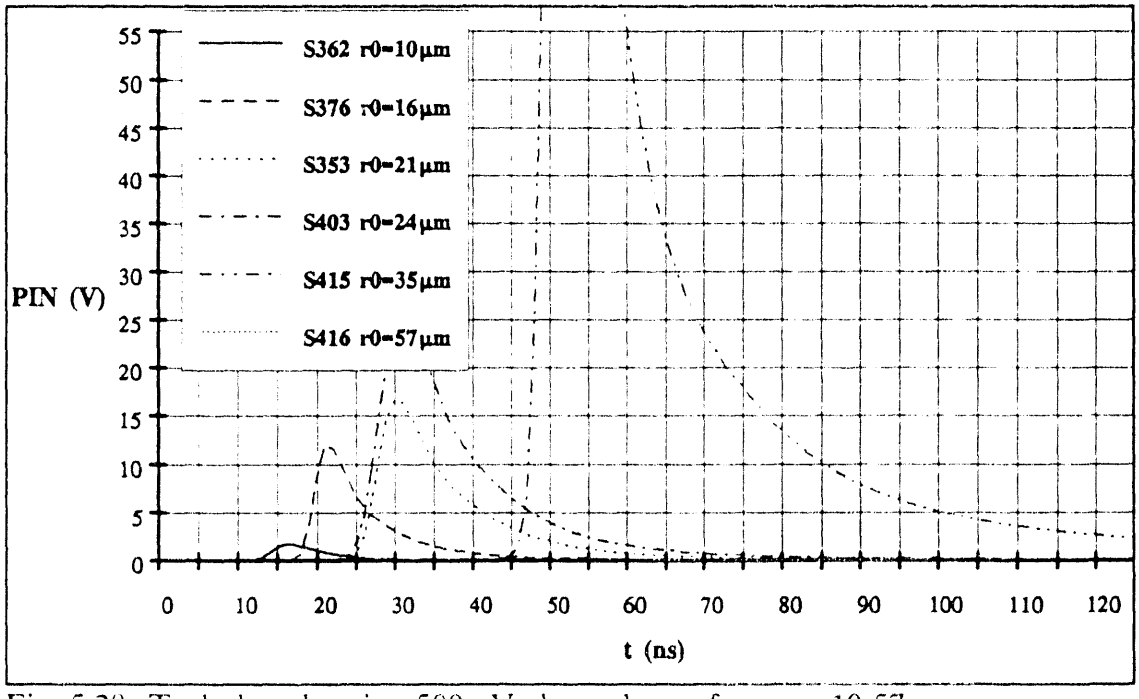

Fig. 5.28 Turbulent heating 500-eV channel vs. t for r_0 = 10-57 μm.

with the electron temperature. The peak voltage of the signals predicted by the turbulent heating model is within a factor of 3 of the data presented in the previous chapter with the exception of shot 415 with a solid-fiber radius of ~35 μm which is about 10 times as large as the data.

The simulated signal falls off as r^{-2} as the plasma expands while the plasma is still small enough to be within the field of view (FOV) of the detector. The signal climbs again as the carbon ions become fully stripped turning on the free-bound line that is brightest at 500 eV. The signal then falls off as r^{-3} because the plasma has expanded beyond the FOV of the spectrometer channel.

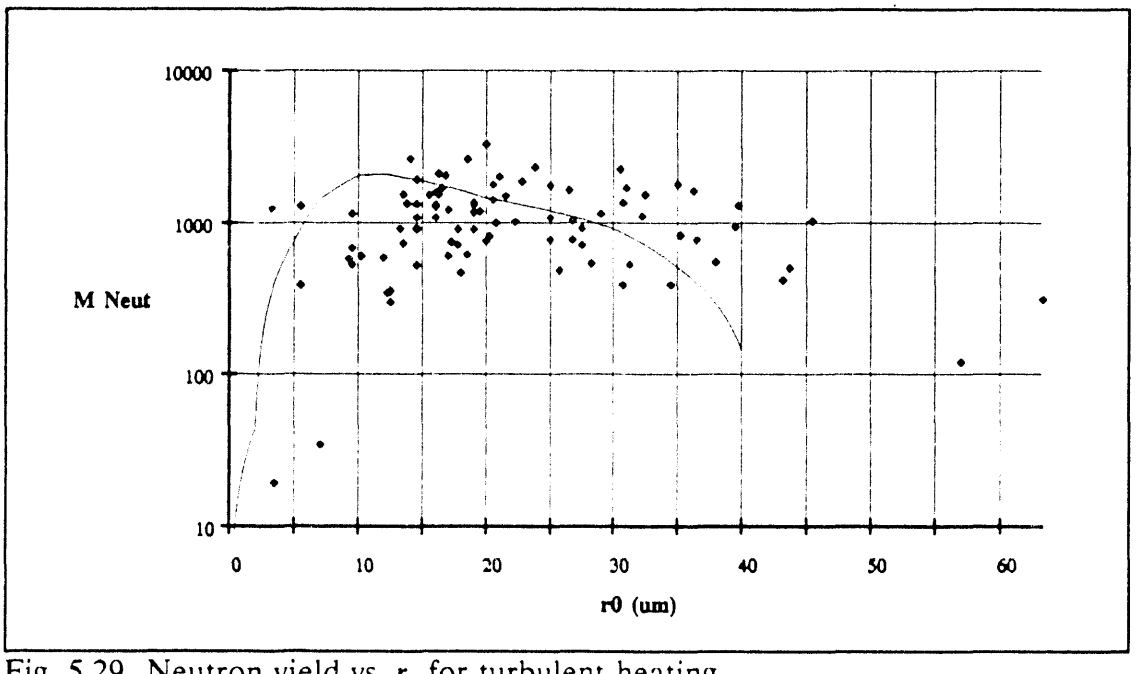

Fig. 5.29 Neutron yield vs. r_0 for turbulent heating.

5.3.5. Comparison of Turbulent Heated Model with Neutron Data

The plots in Fig. 5.29 show the neutron yield as a function of solid-fiber radius predicted by the turbulent heating model plotted over the measured

neutron yields. The simulation was run on the same current waveform from a shot which had no prepulse and which had a peak current of ~800 kA.

The simulated neutron yields are consistent with the data for solid-fiber radii less than 35 μm. The neutron yield data for larger radii may require a more sophisticated model.

VI CONCLUSIONS

The Los Alamos High Density Z Pinch-II facility was used to study the dynamics of z-pinch plasmas generated from solid fibers of deuterated polyethylene, CD_2. The ultimate goal of this research was to find a way to make a solid-fiber z-pinch an economical source of fusion energy despite the observed MHD instabilities. A brief summary of these results is given below. Further diagnostics needed to verify some of the conclusions are also discussed.

6.1. Summary of Main Results

6.1.1. Multiframe Circular Schlieren

Strong $m=0$ instabilities were observed from the start of current flowing through the pinch.

Only one circular-schlieren image (out of ~200) showed any evidence of an $m=1$ MHD instability mode. No higher order modes were observed.

The plasma was observed to expand with an average radial velocity of ~30 km/s during the main current. With few exceptions, the radial velocity was observed to be monotonically increasing during the main current. No radial compressions were observed, nor was there any evidence that the pinch re-collapsed at later times (>60 ns.)

6.1.2. Interferometry

A point-diffraction interferometer was used to show that the "radius" inferred from circular-schlieren images provided a reasonable measure of the average electron density of the pinch.

The electron density is strongly peaked on the axis of the pinch and falls off rapidly at larger radii.

There is a measurable axial flow of plasma even at early times (~6 ns.)

6.1.3. Three Channel X-Ray Spectrometer

The electron temperature is measured to be $\sim 95 \pm 15$ eV from ~20 ns into the main current until ~100 ns (near peak current.)

The magnitude of the signals dropped sharply at late times (>70 ns,) even though the measured electron temperature remains constant, leading to the conclusion that the plasma continues to expand rapidly at late times.

The lower bound on the ion temperature (based on Bennett equilibrium) peaked at 500-2500 eV (depending on the solid-fiber radius,) well above the measured electron temperatures.

6.1.4. Silver-Activation Neutron Counter

The maximum neutron yield measured at a given solid-fiber radius increased sharply as a function of solid-fiber radius, peaked at $\sim 3.3 \times 10^9$ for a solid-fiber radius of ~20 μm, and fell toward zero at a radius of ~55 μm. The minimum yield measured at a given solid-fiber radius were $\sim 5 \times 10^8$ over the majority of solid-fiber radii.

6.2. Main Conclusions

6.2.1. Pinch Expansion Not Due to Enhanced Spitzer

A 0-D simulation was used to compare the data to a stable model and to a model with Spitzer resistivity multiplied by 10. In both cases, the simulated pinch expanded too slowly at late times compared to the data collected by the circular schlieren and spectrometer. The enhanced Spitzer model (with multiplier

of 10) expanded too rapidly at early times. A larger Spitzer multiplier would improve the fit at late times at the expense of worsening the fit at early times.

6.2.2. Enhanced Spitzer Inconsistent with Temperature Data

The stable and enhanced Spitzer models predict electron temperatures higher than measured by the spectrometer and predict ion temperatures lower than the lower bound given by Bennett equilibrium.

6.2.3. Ion Heating Term Required

The lower bound on the ion temperature (assuming Bennett equilibrium) is increasing while the pinch is expanding and exceeds the measured electron temperature for all radii. The plasma is initially dense enough to assume that the particle temperatures are the same for ions and electrons. The expansion and cooler electrons would cause the ion temperature to decrease in the absence of an ion heating term.

6.2.4. Turbulent Heating Consistent with Data

A turbulent heating term was added to the stable model (Spitzer multiplier = 1) based on the assumption that $m=0$ MHD instabilities entrap magnetic field within the plasma and convert the field energy to ion thermal energy much faster than the current rise time. A simple 0-D simulation of this model was shown to be consistent with the radial expansion, time-resolved spatially-averaged electron temperature, x-ray emission, and neutron production of CD_2 fiber shots on HDZP-II over a range of fiber radii.

At larger solid-fiber radii (>38 μm), the radial expansion and neutron yields predicted by this model are less than measured. This may suggest an additional scaling of the turbulent heating term proportional to $[r_0 / (\sim 12\ \mu\text{m})]$.

6.2.5. Higher Currents and Rise Rates Will Not Confine Plasma

The Haines-Hammel curve (which ohmically heats a pinch, with bremsstrahlung radiative cooling, and while maintaining Bennett equilibrium) asymptotically approaches a constant value, the Pease current. Attempting to heat a plasma with the turbulent term described in this document (or any heating power that scales as I^3), with radiative cooling, and while maintaining Bennett equilibrium does not provide as simple a solution.

The assumption of bremsstrahlung radiative cooling gives the differential equation

$$\frac{dI}{dt} = \left(\frac{I^2}{\mathrm{I}^2} - 1\right) \frac{\mathrm{I}}{\tau} \quad (A/s) \,, \tag{6.1}$$

where τ and I are the characteristic time and current, which has the solution

$$t/\tau = \frac{1}{2} \ln\left(\frac{\mathrm{I} - I}{\mathrm{I} + I} \frac{\mathrm{I} + I_0}{\mathrm{I} - I_0}\right), \tag{6.2}$$

where $I(t=0) = I_0$. This solution is only physically meaningful for $I > I_0 >$ I. At late times, the current scales as $I \propto t$ and there is no peak current.

The assumption of blackbody radiative cooling gives the differential equation

$$\frac{dI}{dt} = \left(1 - \frac{I^5}{\mathrm{I}^5}\right) \frac{I^2}{\mathrm{I}^2} \frac{\mathrm{I}}{\tau} \quad (A/s) \,. \tag{6.3}$$

This derivative is zero for $I = 0$ and $I =$ I. At early times, solutions to this equation are proportional to $-t^{-1}$; there are no solutions equal zero at time zero. At late times, solutions to this equation will asymptotically approach this current as

$$I = \mathbf{I}(1+\epsilon) \approx \mathbf{I}(1-e^{-5t/\tau}) \tag{6.4}$$

in the limit as ϵ (< 0) goes to 0. The peak current for CD_2 has the form

$$\mathbf{I}_{CD2} \approx 3\times10^{10} r^{-2/5} r_0^{7/5} \ (A), \tag{6.5}$$

which is ~750 kA for $r = r_0 = 20$ μm. The associated time scale is

$$\tau_{CD2} = 4\times10^{-6} r_0^{-2/5} r^{7/5} , \tag{6.6}$$

which is ~800 ps for $r = r_0 = 20$ μm. This time scale is about two orders of magnitude shorter than can be satisfied by HDZP-II.

6.3. Further Diagnostic Work

The turbulent heating model predicts an ion temperature much higher than the other models which have no direct ion heating. The neutron yield can be explained for the turbulent heating model based on thermonuclear reactions alone. Since these neutrons were not shown to be isotropic, they may have been produced by other mechanisms. An ion temperature diagnostic would verify if there is an ion heating term and if it is consistent the turbulent heating model.

APPENDICES

A. Spitzer Resistivity for Multiple Ion Species

The change in momentum for an electron-ion collision

$$\Delta(m_e v_e) = |Ft| \approx \frac{Z e^2}{4\pi\epsilon_0 b^2}\left(\frac{b}{v_e}\right) \quad (kg\bullet m/s) \ , \tag{A.1}$$

giving the impact parameter as

$$b \approx \frac{Z e^2}{4\pi\epsilon_0 m_e v_e^2} \quad (m) \ . \tag{A.2}$$

Defining the resistivity by

$$E = \eta J = \eta\, e(Z n_i v_i - n_e v_e) \approx -\eta\, e n_e v_e \quad (V/m) \ , \tag{A.3}$$

for $v_e \gg v_i$, the collision frequency is then

$$\nu_{ei} = \frac{Ee}{m_e v_e} = \frac{\eta n_e e^2}{m_e} = v_e \Sigma(n_i \sigma_i) = v_e \Sigma(n_i \pi r_0^2) \quad (s^{-1}) \ , \tag{A.4}$$

where σ_i is the collision cross-section in m^2. The resistivity is then

$$\eta_L = \frac{\bar{Z} e^2}{16\pi\epsilon_0^2 m_e v_e^3} = \frac{\bar{Z} e^2}{16\pi\epsilon_0^2}\sqrt{\frac{m_e}{(2kT_e)^3}} \quad (\Omega\bullet m) \ , \tag{A.5}$$

where $Z = \Sigma Z_i^2 n_i / n_e$. Including small angle collisions, Debye shielding, and strong magnetic field

$$\eta_{Spitz} = \frac{Z\ln\Lambda}{6\epsilon_0^2}\sqrt{\frac{e^2 m_e}{2\pi^3 T_{eV}^3}} = 1.03\cdot 10^{-4}\, Z\ln\Lambda\, T_{eV}^{-3/2} \ (\Omega\bullet m) \ .$$

B. Current for Bennett Equilibrium with Blackbody Cooling

In the high density, high Z_{Λ}, low temperature limit the radiation will be blackbody from the surface, rather than bremsstrahlung from the volume. The internal energy of the plasma increases from joule heating with Spitzer resistivity less the blackbody loss as

$$\frac{3}{2} N_p e \frac{dT}{dt} = \frac{\overline{Z \ln\Lambda}\, I^2}{10^4\, \pi r^2\, T^{3/2}} - 2\pi r \sigma_{SB} T^4 \quad (W/m) , \tag{B.1}$$

where $\sigma_{SB} \approx 1.03\times10^{9}$ W-m^{-2}-eV^{-4} is the Stefan-Boltzmann constant. Assuming Bennett equilibrium, this reduces to

$$\frac{dI}{dt} = \frac{2\times10^{7}}{3I}\left[\frac{4\times10^{7}\overline{Z \ln\Lambda}}{\pi r^2 I}\sqrt{5\,(N_p e)^3} - \frac{\pi r \sigma_{SB} I^8}{8\times10^{28}\,(N_p e)^4}\right] \quad (A/s) . \tag{B.2}$$

This equation can be rewritten as

$$\frac{dI}{dt} = \left(1 - \frac{I^9}{I_{BB}^9}\right)\frac{I_{BB}^2}{I^2}\,\frac{I_{BB}}{\tau_{BB}} \quad (A/s) , \tag{B.3}$$

where the peak current for blackbody radiation is

$$I_{BB} = \left[\frac{32\times10^{34}\,\overline{Z \ln\Lambda}}{\pi^2 r^3 \sigma_{SB}}\sqrt{5\,(N_p e)^{11}}\right]^{1/9} \approx 2.4\times10^{-9}\,\overline{Z \ln\Lambda}^{1/9}\,\frac{N_p^{11/18}}{r^{1/3}} \quad (A) , \tag{B.4}$$

about 2.8 MA for a CD_2 fiber with an initial radius of 100 μm and the time scale

$$\tau_{BB} = \left(\frac{\pi N_p e}{\sigma_{SB}\,\overline{Z \ln\Lambda}^2}\right)^{1/3}\frac{3r}{200} \approx 1.2\times10^{-11}\, N_p^{1/3}\,\overline{Z \ln\Lambda}^{2/3}\, r \quad (s) . \tag{B.5}$$

about 3.4 ns for the same fiber. For a 100 μm radius D_2 fiber, the peak current is 1 MA and the time scale is 6 ns.

The integral in Eq. (B.3) has the solution

$$\frac{t}{\tau_{BB}} = \frac{1}{6}\ln\left[\frac{u^2+u+1}{(u-1)^2}\right] + \frac{1}{\sqrt{3}}\left[\arctan\left(\frac{2u+1}{\sqrt{3}}\right) - \frac{\pi}{6}\right] \qquad for\ u \equiv \left(\frac{I}{I_{BB}}\right)^3 \quad \text{(B.6)}$$

which is plotted in Fig. B.1.

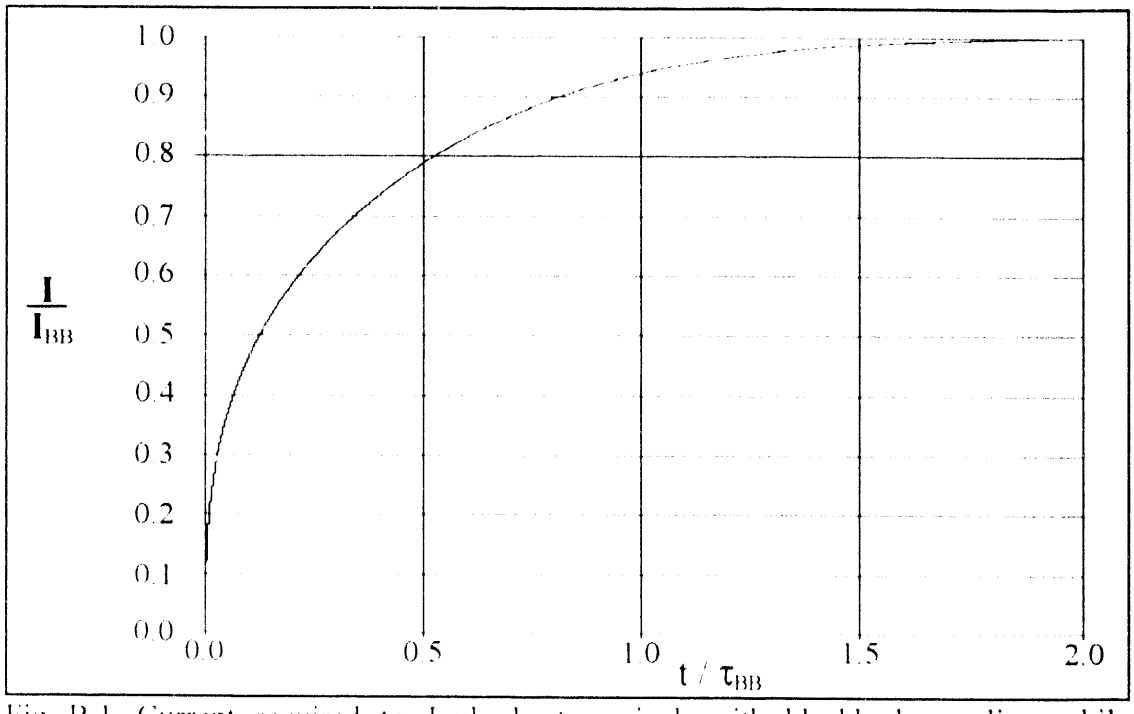

Fig. B.1 Current required to Joule heat a pinch with blackbody cooling while maintaining Bennett equilibrium.

C. Zero-Dimensional Simulation Code

```
#include <stdio.h>
#include <string.h>
#include <math.h>
/*============================================================
Define common numeric and physical constants in SI units.
============================================================*/
#define dPi     (double)  3.14159265358979323846264338327795
#define d2Pi    (double)  6.28318530717958647692528676655900
#define d4Pi    (double) 12.56637061435917294385057353311800
#define dPi415  (double)  6.4939394          /* π^4 / 15  */

#define dU0     (double) 12.56637061435917294385057353311e-7
#define dU04Pi  (double) 1e-7 /*FreeSpace Permiability/4π*/
#define dClit   (double) 2.99792458e+8  /*Speed of light.*/
#define dE0     (double) 8.85421878e-12 /*FS Permittivity*/
#define dHplk   (double) 6.626176e-34 /*Plank's constant.*/
#define dHbar   (double) 1.0545887e-34   /*h/2π.(J-s/rad)*/

#define dQe     (double) 1.6021892e-19 /*Electron charge.*/
#define dMe     (double) 9.109534e-31     /*Electron mass.*/

#define dAfin   (double) (1./137.035963) /* Fine Structure*/
#define dRecl   (double) 2.817938e-15   /*Classical e rad.*/
#define dRydb   (double) 13.605803      /*Rydberg constant.*/
#define dWplas  (double) 56.414579  /*wp scale/sqrt E0*Me)*/
#define dhwpe   (double) 1.7133053e-14      /* ħ * wpq scl*/
```

```
#define dSptz (double) 1.04e-5 /*sqrt(MeQe/2π^7)/(6E0^2)*/
#define dBrem (double) 1.537e-38
                       /* 4/3 a^3 h^2 sqrt(2e/(3(πm)^3))*/
#define dGBrem  (double) 1.4        /*Brems Gaunt factor.*/

#define dLambda (double) 0.532e-6 /*Laser wavelength (m)*/

#define dMd     (double) 3.3445e-27 /*Deuterium mass.(kg)*/
#define dMc     (double) 1.9945e-26     /*Carbon mass.(kg)*/

#define dn0D2   (double) 5e+28     /*Solid D2 part density*/
#define dn0CD2  (double) 3.75e+28   /*Solid CD2 C density*/
#define dp0CD2  (double) 1e+3     /*Solid CD2 mass density*/

#define dIPd    (double)  13.598    /*Deut ioniz potential*/
#define dIPc0   (double)  11.260  /*Carb ioniz potentials*/
#define dIPc1   (double)  24.384
#define dIPc2   (double)  47.888
#define dIPc3   (double)  64.494
#define dIPc4   (double) 392.09
#define dIPc5   (double) 490.
double dIPC[6]={dIPc0, dIPc1, dIPc2, dIPc3, dIPc4, dIPc5};

#define SigVddC (double) 2.33e-18 /*σv coeff(eV^2/3m^-3)*/
#define SigVddE (double) -187.6   /*σv exponent.(eV^1/3)*/
#define iMxSmp (unsigned) 200      /*Max # of I samples.*/
 *=============================================================
PROGRAM: ZebraSim.c  AUTHOR: Ronald A. Riley Jr.
PURPOSE:  This program simulates the HDZP plasma.
COMPILE:  cc zsim.c -dalign -cg89 -O4 -o zsim.exe
PARAMETERS: Name of input ACSII data file containing:   */
```

```
    double dR0, dR1;    /*Solid-fiber, initial radii (m).*/
    double dt0;         /*Starting time from first I samp*/
    double dv1;         /*Initial radial velocity (m/s). */
    double dDt;         /*Time between I sampels (s).    */
    int      iNISamp;   /*Number of current samples.     */
    double dIS[iMxSmp]; /*Current samples. (Amps)        */
/*=====================================================*/

double dsqMCD2; /*sqrt(p r0^2 π) p=1000kg/m^3 r0=fib rad*/
double dNcPi;       /*Carb particle line density / π (/m)*/
double dICS[4*iMxSmp],dI;  /*Cubic spline coeffs. for I.*/
double dTe=3.,dTd,dTc;  /* Temps of elects, deuts, and C*/
double dne;         /*(Z) # of free electrons / C nucleii*/
double dJHeat, dTHeat;      /*Joule, turb heating terms.*/
double dRadCol, dStrip; /*Radiation, ioniz cooling terms*/
double dndc[9];  /*Densities of c[0-6],d[7,8] ion states*/
double dhw,dhwT;  /*Photon energy for alpha*R=1, Te (eV)*/
double dConL[6];        /*Continuum lowering energy (eV)*/
double dCh1,dCh2,dCh3;  /*Sim signals of spectrom channs*/
int iFlag=0;

main (iArgC, ppArgV) int iArgC; char **ppArgV;  {
#define iNeq    (unsigned)  6 /*# of equations to integr.*/
#define dI0     (double) 5e+4         /* Initial current.*/
#define dIEps   (double) 1e-4   /*Integration error limit*/
#define dNeg    (double)-1e-30       /* Test for dY/dt<0.*/
#define dtstep  (double) 1e-9     /*Time between outputs.*/
static char sHF[]="\n\nt_ns I_KA r_μm vr_m/s Tc_eV \
Td_eV Te_eV Neutrons IonPot Radiat JouleH Turbul Z0 \
nC1    nC2    nC3    nC4    nC5    nC6    nC7    nD1    \
nD2    Ch1(mV) Ch2(mV) Ch3(mV)";
```

```
static char sOF[]="\n%5.1lf%4.0lf%5.0lf%7.0lf%6.0lf%6.0lf\
%6.0lf%9.2le%7.0le%7.0le%7.0le%7.0le%3.0lf %5.3lf";
static double dYscal[iNeq]={1e-5,1e3,1e28,2e28,8e28,1e2};
/* Y error scales.*/
    register int i,j;
    register double *pdReg1;
    double pdScrt[105]; /*bsstep work space 11+13*(Nv+1)*/
    char   sFilNam[80],*pc;          /*File name string.*/
    FILE   *pFile; /*File handle for data, results files*/
    double dY[iNeq];      /* Y0 = r      Radius.          */
    double *pdY1=dY+1;    /* Y1 = dr/dt, Radial velocity.*/
    double *pdY2=dY+2;    /* Y2 = Uc carb energy density.*/
    double *pdY3=dY+3;    /* Y3 = Ud deut energy density.*/
    double *pdY4=dY+4;    /* Y4 = Ue elec energy density.*/
    double *pdY5=dY+5;    /* Y5  = Neutron yield.        */
    double dDy[iNeq];     /* Time derivatives of vars.   */
    double *pdDy2=dDy+2,*pdDy3=dDy+3,*pdDy4=dDy+4;
    double dnc;           /*Carbon nucleii density(C/m^3)*/
    double dt,dtarg;      /*Current and target times. (s)*/
    double dHtry,dHdid,dHN;   /* dt to try, done, and dt*/
    double dSahaCD2Z();      /*Saha ionization state CD2.*/
    void   bsstep(),csakima(); /*Bulirsh-Stoer, Akima Sp*/
    int    der();             /*Computes derivs for bsstep*/

/*************************************************************
    Make sure user input data file name on command line.
*************************************************************/
    dStrip = 1e40;
    printf(" nHDZP-II 0-Dim sim with turb heating.");
    if (iArgC != 2)
        {printf(" nUsage: ZEBRASIM <file>");  exit(1);}
```

```
/*************************************************************
    Open the file to read in the current in text mode.
*************************************************************/
    pFile = fopen(strcpy(sFilNam, *(ppArgV+1)), "r");
    if (NULL == pFile)
     {printf("\n\n%s not found.", sFilNam);  exit(1);}

/*************************************************************
    Read and close data file and spline fit I samples.
*************************************************************/
    printf("\n\nReading data file: %s\n", sFilNam);
    fscanf(pFile,"%lf\n%lf\n%lf\n%lf\n%lf\n%d",
     &dR0,dY,&dt0,pdY1,&dDt,&iNISamp);
    if (iNISamp > iMxSmp)  iNISamp = iMxSmp;
    for (pdReg1=dIS, i=iNISamp; i--; )
        fscanf(pFile, "%lf\n", pdReg1++);
    fclose(pFile);
    printf("\nr0=%7.3fμm, r1=%7.3fμm, dt=%4.1fns",
        dR0*1e6, *dY*1e6, dDt*1e9);

/*************************************************************
    Open output results file an print input params.
*************************************************************/
    if (NULL != (pc = strchr(sFilNam, '.'))) *pc = '\0';
    if (NULL == (pFile=fopen(strcat(sFilNam,".sim"),"w")))
     {printf("\n\nFile %s open error.",sFilNam); exit(1);}
    printf("\n\nCreating results file: %s\n", sFilNam);
    fprintf(pFile, "File: %s, r0=%7.3fμm, dt=%4.1fns",
      sFilNam, dR0*1e6, dDt*1e9);

/*************************************************************
```

```
    Compute the current at the starting time.
*************************************************************/
    csakima(iNISamp, dIS, dICS);
    dt = dt0 / dDt - (i = (int)(dt0 / dDt));
    pdReg1 = dICS + 4*i;
    dI = *pdReg1 +
         dt*(*(pdReg1+1)+dt*(*(pdReg1+2)+dt**(pdReg1+3)));

/*************************************************************
    Compute initial electron thermal energy density Ue.
*************************************************************/
    dnc = (dNcPi = dn0CD2*dR0*dR0) / (*dY * *dY);
    dsqMCD2 = sqrt(dPi*(dMc+dMd+dMd)*dNcPi);
    *pdY4= .75/d2Pi/ *dY * dU04Pi*dI*dI/ *dY /dQe;

/*************************************************************
    Compute ioniz state and initial temp (Te=Tc=Td~3eV)
*************************************************************/
    dne  = dSahaCD2Z(1, *pdY4,*pdY4,*pdY4, *dY,dnc,dndc,
              &dTc,&dTd,&dTe, dDy, dDy+1, dDy+2, &dRadCol);
    *pdY2 = 1.5 * (dTc=dTe) * dnc * (1.-*dndc);
    *pdY3 = 1.5 * (dTd=dTe) * dnc * dndc[8];
    *pdY5 = 0.;

/*************************************************************
    Initialize derivs and print header, initial values.
*************************************************************/
    der ((dt=dt0), dY, dDy);
    printf(sHF);
    printf(sOF,dt*1e9,dI*1e-3,*dY*1e6,*pdY1,dTc,dTd,dTe,
        *pdY5,dStrip,dRadCol,dJHeat,dTHeat,dne*10.,*dndc);
```

```
    for(pdReg1=dndc+1,i=8; i--; )  printf(" %5.3lf",
                    *(pdReg1++)/((i>1) ?(8-i)*(8-i) :1));
    printf(" %7.0lf %7.0lf %7.0lf",
           dCh1*1e3,dCh2*1e3,dCh3*1e3);
    fprintf(pFile,sHF);
    fprintf(pFile,sOF,dt*1e9,dI*1e-3,*dY*1e6,*pdY1,
        dTc,dTd,dTe,*pdY5,dStrip,dRadCol,dJHeat,dTHeat,
        dne*10.,*dndc);
    for(pdReg1=dndc+1,i=8; i--; ) fprintf(pFile," %5.3lf",
                 *(pdReg1++) / ((i>1) ? (8-i)*(8-i) : 1));
    fprintf(pFile, " %7.0lf %7.0lf %7.0lf",
                   dCh1*1e3,dCh2*1e3,dCh3*1e3);
    fflush(pFile);

/*************************************************************
    Integrate the ODE's over the current samples.
*************************************************************/
    for(j=(int)((iNISamp*dDt-(dtarg=dtstep+dt0))/dtstep);
                                        j--;dtarg+=dtstep){
     dHtry=dtstep*0.01; /*Integrate to next output time.*/
     while  (dtarg > dt + dtstep*dIEps) {

    /*********************************************************
       Make dt small to avoid non-physical r and Uc,d,e.
    *********************************************************/
        if(*dDy  <dNeg)
            if(dHtry >(dHN=-0.5* *dY / *dDy))    dHtry=dHN;
        if(*pdDy2<dNeg)
            if(dHtry>(dHN=-0.5* *pdY2/ *pdDy2))  dHtry=dHN;
        if(*pdDy3<dNeg)
            if(dHtry>(dHN=-0.5* *pdY3/ *pdDy3))  dHtry=dHN;
```

```
    if(*pdDy4<dNeg)
        if(dHtry>(dHN=-0.5* *pdY4/ *pdDy4)) dHtry=dHN;
    iFlag=0;

/*******************************************************
    Integrate over time step,
    init next step to min of suggested and tot
*******************************************************/
    bsstep(&dt,iNeq,dY,dDy,dHtry,dIEps,dYscal,
           &dHdid,&dHN,der,pdScrt);
        dHtry = (dtarg - dt); /*Stop at target time.*/
        if (dHtry > dHN) dHtry = dHN;
        if (dHtry > 2e-10) dHtry = 2e-10;
    }
    printf(sOF,dt*1e9,dI*1e-3,*dY*1e6,*pdY1,
           dTc,dTd,dTe,*pdY5,dStrip,dRadCol,
           dJHeat,dTHeat,dne*10., *dndc);
    for (pdReg1=dndc+1, i=8; i--; )
        printf(" %5.3lf",
             *(pdReg1++) / ((i>1) ? (8-i)*(8-i) : 1));
    printf(" %7.0lf %7.0lf %7.0lf",
           dCh1*1e3,dCh2*1e3,dCh3*1e3);
    fprintf(pFile,sOF,dt*1e9,dI*1e-3,*dY*1e6,*pdY1,
            dTc,dTd,dTe,*pdY5,dStrip,dRadCol,dJHeat,
            dTHeat, dne*10., *dndc);
    for(pdReg1=dndc+1,i=8; i--; )
        fprintf(pFile, " %5.3lf",
             *(pdReg1++) / ((i>1) ? (8-i)*(8-i) : 1));
    fprintf(pFile, " %7.0lf %7.0lf %7.0lf",
            dCh1*1e3,dCh2*1e3,dCh3*1e3);
    fflush(pFile);
```

```
    }
    fclose(pFile);
}

int der (dt, pdY, pdDy)
    double dt;    /*Independent variable time. (sec)     */
    double *pdY;  /*Y0 = r      Radius of plasma. (m)
                    Y1 = dr/dt Radial velocity.(m/s)
                    Y2 = Uc     Carb energy density.
                    Y3 = Ud     Deut energy density.
                    Y4 = Ue     Elec energy density.
                    Y5 = Neutron yield.                  */
    double *pdDy; /*dY0/dt = Y1
                    dY1/dt = (Pint-Pext) 2pi r/m
                    dY2/dt = DUx*Y2+dDUec+dDUdc+dTHeat*3/4
                    dY3/dt = DUx*Y3+dDUed-dDUdc+dTHeat*1/4
                    dY4/dt = DUx*Y4-dDUed-dDUec+dJoul-dRad
                    dY5/dt = Vol *nd(ion)*nd(total)*sv */
{
/*============================================================
SUBROUTINE: der.c   (ZebraSim.c)
AUTHOR:     Ronald A. Riley Jr.      DATE: 1/23/93
PURPOSE:    Derivative function supplied to ODE integrator
            for the Zebra turbulent heating simulator.
            Plasma density is assumed constant over r
            (0-D self-simular).

Returns integer value 0 if failed, 1 if successful.
============================================================*/
#define dTurb   (double) 1.26e8     /*Turb heating coeff*/
#define dThr    (double) 2.6315e-28
```

```
#define dTol     (double) 1e-7       /*Tolerance for <0. */
#define dDEps    (double) 1e-9 /*Eps for ionization rates*/
#define dPLen    (double) 0.05        /*Pinch length. (m)*/
#define dn2Gamm (double) (-10./3.) /*-2 *gamma for 3 DOF*/
#define dVisDmp (double) 2e8    /*Viscous damping of vel*/
#define dPico    (double) 1e-12

    register int i;
    register double *pdReg1, *pdReg2, *pdReg3;
    double dUc,dUd,dUe,dDUe;  /*C, D, e energy densities*/
    double dR, dR2;  /*Local copy of radius (m), squared*/
    double dI2, dx;       /*I squared at t and interp var*/
    double dKPres;        /*Kinetic pres 2/3 Qe(Uc+Ud+Ue)*/
    double dMPres;         /*Mag pres U0 I^2 /(8Pi^2 r^2)*/
    double dDUexp;   /*Expans coeff for energy densities*/
    double dnc,dnc2;       /*C particle density (m-3), ^2*/
    double dTe3,dSqrtTe,dTe32; /*Te^3  Te^(1/2) Te^(3/2)*/
    double dMT;                 /* dMd * dTc + dMc * dTd */
    double dZTd;                /* (nd/nc) / Td          */
    double dTherm;            /* Thermal expansion coeff.*/
    double dRSptz;        /*Spitzer resistance (ohm/m)/π */
    double dTd3;                              /*  Td^1/3 */
    double dSigmaVdd;      /*σv for d-d reactions.(m^3/s)*/
    double dDUed,dDUec,dDUdc;    /*Thermal equil. terms.*/
    double dIE0,dDIE;     /*Ioniz energy density, change.*/
    double dErr,dEr0,dEr1;      /*Errors for ioniz rates.*/
    double dSt0,dSt1,dDS;  /*Min,max,diff stripping rate*/
    double dSahaCD2Z();       /*Saha ionization function.*/
    int j;

**********************************************************
```

```
    If non physical values (r,Uc,Ud, or Ue <= 0.),
    return error value (0).
*************************************************************/
    dUc=pdY[2];  dUd=pdY[3];  dUe=pdY[4];
    if(dUc<dTol || dUd<dTol || dUe<dTol || pdY[5]<0.)
        return(0);

/*************************************************************
    Compute spline fit for current at time t.
*************************************************************/
    if (iNISamp-2 < (i = (int)(dx=dt/dDt))  i = iNISamp-2;
    pdReg1 = dICS + 4 * i;
    dx -= i;
    dI = *pdReg1 +
       dx*(*(pdReg1+1) +dx*(*(pdReg1+2) +dx**(pdReg1+3)));
    dI2 = dI*dI;

/*************************************************************
    dvr/dt = (Pin - Pex) 2pi r/(m*2/3).
*************************************************************/
    if (*pdY < dTol)
        {*pdY=dTol;  if (pdY[1]<dTol) pdY[1] = dTol;}
    *pdDy = pdY[1];
    dR2 = dR * (dR = *pdY);
    dMPres = (dU04Pi/d2Pi) * dI2 / dR2;
    dKPres = (dQe/1.5) * (dUc + dUd + dUe);
    dx = dR - dTol;
    pdDy[1]=1.5*dR*(dKPres-dMPres)*d2Pi/(dsqMCD2*dsqMCD2)-
                    *pdDy*dVisDmp - 1e-5 / (dx*dx*dx*dx);
    dTHeat = dTurb * dI2*dI / (dR2*dR * dsqMCD2);
```

```
/*************************************************************
    Compute charged particle densities and temps in eV.
    Assume that the neutrals are cold.
*************************************************************/
    dnc2 = dnc * (dnc = dNcPi / dR2);
    dne  = dSahaCD2Z(0, dUc,dUd,dUe, dR,dnc,dndc,
           &dTc,&dTd,&dTe, &dDUed,&dDUec,&dDUdc,&dRadCol);

/*************************************************************
    Calculate the Spitzer resistivity.
*************************************************************/
    dTe3 = dTe * dTe * dTe;
    dTe32 = dTe * (dSqrtTe = sqrt(dTe));
    dRSptz = (dDUed+dDUec)/dne *dSptz/(dR2*dTe32); /*1/π*/
    dJHeat = dRSptz *dI2 /(dR2*dQe); /*1/Qe for eV/m^3-s*/

/*************************************************************
    Calculate the thermal equilibration terms.
*************************************************************/
    dTherm  = dThr * dnc2;
    dMT     = dMd * dTc + dMc * dTd;
    dDUdc*=dTherm*(dTd-dTc)*dndc[8]*sqrt(dMd*dMc/dMT)/dMT;
    dTherm *= sqrt(dMe) * dne / dTe32;
    dDUed  *= dTherm * (dTe - dTd) / dMd;
    dDUec  *= dTherm * (dTe - dTc) / dMc;

/*************************************************************
    Update the rates of change of energy densities.
    Adiabatic expans coeff of energy densities, Gamma=5/3.
*************************************************************/
    dDUexp  = dn2Gamm* *pdDy / dR;
```

```
    pdDy[2] = dDUexp * dUc +dDUec +dDUdc +dTHeat*0.75;
    pdDy[3] = dDUexp * dUd +dDUed -dDUdc +dTHeat*0.25;
    pdDy[4] = dDUexp * dUe -dDUed -dDUec +dJHeat -dRadCol;

/*************************************************************
    Calc σv for d-d fusion reactions. (All tritons burned)
*************************************************************/
    dTd3 = pow(dTd, 1./3.);
    dSigmaVdd = SigVddC / (dTd3*dTd3) * exp(SigVddE/dTd3);
    pdDy[5] =dSigmaVdd*(dPLen*dPi*dR2)*(4.*dnc2)*dndc[8];

/*************************************************************
    Only calc ion stripping term once per call to bsstep.
*************************************************************/
    if (iFlag)  {pdDy[4] -= dStrip; return(1);}
    iFlag = 1;

/*************************************************************
    Reduce the electron heating by the ioniztaion rate.
*************************************************************/
    dDUe =  pdDy[4];
    dUd +=  pdDy[3] * dPico;
    dUc +=  pdDy[2] * dPico;
    dR  += *pdDy    * dPico;
    if (dUc<dTol || dUd<dTol || dR<dTol ||dDUe+dUe/dPico<dTol)
        return iFlag=0;
    dIE3 = (*dConL < dIPd) ? dndc[8] * (dIPd-*dConL) : 0.;
    pdReg1=dndc+6;  pdReg2=dIPC+6;  pdReg3=dConL+6;
    for (i=7; i>1; i--)
        if (0. < (dDS = *(pdReg2--) - *(pdReg3--)))
            dIE3 += * pdReg1--) * i*i) * dDS;
```

```
    dnc  = dNcPi / dR / dR;

/*************************************************************
    Itterrate Ue and ionization rates until in balance.
*************************************************************/
    dSt0 = dEr0 = dEr1 = 0.;
    dSt1 = (0. < dDUe) ? dDUe : dStrip + dStrip + 1e29;
    if (dSt1 > dDUe+dUe/dPico) dSt1=0.99*(dDUe+dUe/dPico);
    if (dSt1 < dSt0) {dStrip = 0.;  return(iFlag=1);}
    if (dStrip > dSt1) dStrip = dSt1;
    for (dTe3=dTe, j=30; j--; ) {
        if (0. > (pdDy[4] = dDUe - dStrip)*dPico + dUe)
            return(iFlag=0);
        dne = dSahaCD2Z(1, dUc,dUd,dUe+dPico*pdDy[4],
                    dR,dnc,dndc, &dTe3,&dTe3,&dTe3,
                    &dDUed, &dDUec, &dDUdc, &dRadCol);
        dDIE = (*dConL <dIPd) ?dndc[8]*(dIPd-*dConL) : 0.;
        pdReg1=dndc+6;  pdReg2=dIPC+6;  pdReg3=dConL+6;
        for (i=7; --i; )
            if (0. < (dDS = *(pdReg2--) - *(pdReg3--)))
                dDIE += *(pdReg1--) /(i*i) * dDS;

/*************************************************************
        Update the guess for ionization rate. Regula Falsa
*************************************************************/
        dErr = (dDIE - dIE0) * dnc / dPico;
        dEr1 = (dErr-dStrip) / (dDEps +fabs(dErr+dStrip));
        if (1e-5 > fabs(dErr)) break;
        dDS = 0.5 * (dSt1 - dSt0);
        if (0. < dErr)              {dEr0=dErr; dSt0=dStrip;
            if (dDS*.1e-5*fabs(dSt0)>dSt1) break;
```

```
        } else                          {dEr1=dErr; dSt1=dStrip;
            if (dSt0+1e-5*fabs(dSt0)>dSt1)  break;
        }
        if(dSt0>(dDUe+dUe/dPico)*0.98) return(iFlag=0);
        if(dSt1>dDUe+dUe/dPico)dSt1=(dDUe+dUe/dPico)*0.99;
        dStrip = (dDS<dSt1-dSt0) ? (dSt1+dSt0) * 0.5 :
                 (dSt1*dEr0 - dSt0*dEr1) / (dEr0-dEr1);
    }
    if (dStrip < 0.) {dStrip = 0.;  pdDy[4] = dDUe;}
    return(1);
}

double dSahaCD2Z (iFl, dUc,dUd,dUe, dR,dnc,dndc,
            pdTc,pdTd,pdTe, pdZLed,pdZLec,pdZLdc,pdRadCol)
    int        iFl;              /*Flag for early return.*/
    double dUc,dUd,dUe;          /*Input energy densities*/
    double dR;                  /*Input plasma radius.(m)*/
    double dnc;                /*Input C particle density*/
    double dndc[9];  /*Output ioniz dens C[0-6],2*D[7-8]*/
    double *pdTc,*pdTd,*pdTe;          /*Updated temps(eV)*/
    double *pdZLed,*pdZLec,*pdZLdc;    /*Sum{Z^2 ln(L)}.*/
    double *pdRadCol;    /*Radiation cooling. (eV/s-m^3)*/
{
/*************************************************************
AUTHOR:  Ronald A. Riley Jr.  DATE: 1/22/1993
PURPOSE: This function computes Saha ionization for CD2.
RETURNS: Z    Number of free electrons per carbon (ne/nc).
*************************************************************/
#define dSEps (double)    1e-7 /*Rel error limit of Z*Te.*/
#define dSaha (double)    6.0371e27 /*2[2πme qe/ h^2]^1.5*/
#define iZm               6 /* Max ionization for carbon.*/
```

```
#define dlLA  (double)  29.272447 /*ln(16π^2(E0/Qe)^3)/2*/
#define dlLB  (double)  30.924269  /* ln(Me E0/Hbar^2)/2*/
#define dlLL  (double)  1e-5      /*Lower limit on ln(L)*/
#define dlLTc (double)  27.211606
                    /*exp(2*(B-A)) =Me Qe^3 /(2 h E0)^2 */
#define dDFB  (dIPd+dIPd)    /*Deuterium Free-Bound (eV)*/
#define dAlph (double) 4.853e-47
                  /*4/3 hb^5(af2pi/e)^3c^2sqrt(2/3pim^3e)*/
#define dBlkB (double)  1.97661e27
                    /* Balckbody 4pi(e/h)^3/c^2 (eV/m^2)*/
#define dCLSc (double)  5.8111e-13 /*Cont lowering scale*/
static double dGrc[iZc*3]= {9.,  5.,  1.,   6., 12., 10.,
                            1.,  9., 11.,   2.,  6., 18.,
                            1., 15., 18.,   2.,  8., 14.};
static double dECL[iZc*2]={1.2639,   2.6841,   5.3338,
                           9.2905,   6.4863,  12.7,
                           8.,      38.4,    300.,
                         354.,     367.,     435.};
static double dlni[iZc]={0., 0.6931472, 1.098612,
                             1.386294, 1.609438, 1.79176};
static double dFBhw[14] ={dRydb/9.,   dRydb/4.,dRydb/2.25,
                          dIPc0,       dIPd,   dRydb,
                          dRydb/0.5625,dIPc1,  dIPc2,
                          dIPc3,    dRydb*6.25,dRydb*9.,
                          dIPc4,     dIPc5};
static dcuble dFBScl[14]={dRydb/13.5,dRydb/4.,dRydb/3.375,
                          dIPc0*.625,dIPd*2., dRydb/1.5,
                        dRydb*32./27.,dIPc1*.75,dIPc2*.875,
                          dIPc3,   dRydb*6.25,dRydb*9.,
                          dIPc4,    dIPc5*2.};
static int    iFB[14] = {1,8,2, 1,8,3, 4,2,3, 4,5,6, 5,6};
```

```
register int i, *piReg;
register double *pdReg1,*pdReg2;
    double *pdReg3, *pdReg4;
    double dTemp, dSqT, dTe3; /*Local copy of Te,sqrt,^3*/
    double dT0, dT1, dDT; /*Lower and upper bounds on Te*/
    double dUenc32;              /*Ue/[1.5 nc] = Z Te (eV)*/
    double dErr,dErr0,dErr1;  /*Ue/nc error for Te,T0,T1*/
    double dZ;           /*# free elects /Carbon nuclei.*/
    double dSaSc;                  /*Saha scaling fcator.*/
    double dRd;   /*Deuterium ion state density. (/Carb)*/
    double dZP[7], dCLZ;  /*Part. functions for C states*/
    double dSum, dSumZ,dZ0,dZ1; /*Sum of state dens, *Z */
    double dLnLamb,dlnLA,dlnLB;    /*Coulomb logarithms.*/
    double dnT;       /* [(Md+Mc)/(Md*Td + Mc*Tc)]^2 *nc*/
    double dMT, dZTd;  /* dMd*dTc + dMc*dTd, (nd/nc)/Td */
    double dAlpR, dAlpr;    /*Absorption coeff * radius.*/
    double dBFBScl;       /*Scale for Brems and F-B rad.*/
    int    iMax, j;  /*Index of highest density C state.*/

/************************************************************
    Compute initial guess for electron temperature in eV.
    Ue / [1.5 nc] = Z Te ~ (2+i) IP[i]
************************************************************/
    dUenc32 = dUe / dnc / 1.5;
    dT1 =2. *(dTemp=(*pdTe<(dT0=dUenc32/8.)) ?dT0 :*pdTe);
    dZ0 = 5.75;
    if (0 > (iMax = ((int)(dZ=dUenc32/dT1)) -2)) iMax = 0;
    dZ1 = (!iMax) ? 2. : 1. + (2.+ (iMax*iMax*iMax+
              (dZ-2-iMax)*(iMax+1)*(iMax+1))/(dZ-2.))/dZ;
    if (0 > (iMax = (int)(dZ=dUenc32/dTemp)) -2)) iMax =0;
    dSumZ = (!iMax) ? 2. : 1. + (2.+(iMax*iMax*iMax+
```

```
                (dZ-2-iMax)*(iMax+1)*(iMax+1))/(dZ-2.))/dZ;

/*********************************************************
    Continue until the electron temperature converges.
*********************************************************/
    dZP[6] = 2.;
    dErr = dErr1 = dErr0 = 0.;
    for (j=50; j--; ) {

    /*******************************************************
        Compute the continuum lowering.
    *******************************************************/
        dTe3 = dTemp*dTemp*dTemp;
        dRd = dCLSc * sqrt(dZ*dnc*dSumZ*dSumZ*dSumZ/dTe3);
        for (pdReg1=dConL+(i=7)-1; --i; )
            *(--pdReg1) = (pow(((i*dRd)>1.) ?2. :i*dRd+1.,
                        2./3.) -1.) /(dSumZ+dSumZ) *dTemp;

    /*******************************************************
        Calculate ioniz based on current guesses for Te,Z.
    *******************************************************/
        dSaSc = dSaha *dTemp *(dSqT=sqrt(dTemp)) /dnc /dZ;
        dRd=(*dConL>dIPd) ?1e99 :dSaSc /(exp(dIPd/dTemp) +
            ((*dConL>dIPd/4.) ?0. :4.*exp(dIPd/dTemp/4.)));

    /*******************************************************
        Calculate part functions for carbon ioniz sates.
    *******************************************************/
        pdReg1=dZP; pdReg2=dECL; pdReg3=dGrc; pdReg4=dIPC;
        for (i=6; i--; pdReg4++){
            dCLZ = *(dConL + 5-i);
```

```
        *(pdReg1++)=(dCLZ>*pdReg4)      ?0. : *pdReg3 +
                    ((dCLZ>*pdReg4-*pdReg2) ?0. :
                       *(pdReg3+1)/exp(*pdReg2/dTemp) +
                    ((dCLZ>*pdReg4-*(pdReg2+1)) ?0. :
                   *(pdReg3+2)/exp(*(pdReg2+1)/dTemp)));
        pdReg3+=3;
        pdReg2+=2;
    }
    while(*(dZP+iMax) < dSEps) iMax++;

/*********************************************************
    Compute ratios of C ion state dens above largest.
*********************************************************/
    pdReg1 = (pdReg2 = dndc + iMax) + 1;
    pdReg3 = dZP  + iMax;
    pdReg4 = dIPC + iMax;
    dSum=*pdReg2=1.;  dSumZ=iMax;
    for (i=iZc-iMax; i--; pdReg3++) {
        dSum += (*(pdReg1++) = *pdReg2 *dSaSc *
            *(pdReg3+1) / *pdReg3 /
            exp((*(pdReg4++) - *(dConL+5-i)) /dTemp));
        dSumZ += *(++pdReg2) * (double)(iZc-i);
    }

/*********************************************************
    Compute ratios of C ion state dens below largest.
*********************************************************/
    pdReg3 = dZP  + iMax;
    pdReg4 = dIPC + iMax;
```

```
    for pdReg1=pdReg2=dndc+(i=iMax+1)-1;--i;pdReg3--){
        if (*(pdReg3-1) < dSEps)
            {while(i--) *(--pdReg1)=0.;  break;}
        dSum += (*(--pdReg1) =
                *pdReg2 / dSaSc * *(pdReg3-1) / *pdReg3
                *exp((*(--pdReg4)-*(dConL+i))/ dTemp));
        dSumZ += *(--pdReg2) * (double)(i-1);
    }
    if(0>(iMax=
         ((int)(dZ=(dRd+dRd)/(1.+dRd)+dSumZ/dSum))-2))
        iMax=0;

/*******************************************************
    Normalize ionization state densities
    (/Carbon nucleii), multiply by Z^2.
*******************************************************/
    dSumZ = dndc[8] = dRd * (dndc[7] = 2./(1.+dRd));
    for (pdReg1=dndc-1+(i=iZc+1); --i; )
        dSumZ+=(*(pdReg1--)*=i*i/dSum);
    *pdReg1 /= dSum;
    dSumZ = (dSEps < dZ) ? 1. + dSumZ / dZ : 0.;

/*******************************************************
    Update the guesses for the Te and Z. Regula Falsa
*******************************************************/
    if (dSEps > fabs(dErr=1.-dTemp * dZ / dUenc32))
        break;
    dDT = 0.8 * (dT1 - dT0);
    if (0. < dErr)  {dErr0=dErr; dZ0=dSumZ; dT0=dTemp;
        if (dT0+dSEps>dT1)
            {dErr1=0.; dZ1=dSumZ; dT1=dT0*(1.+dErr+dSEps);}
```

```
        } else          {dErr1=dErr; dZ1=dSumZ; dT1=dTemp;
            if (dT0+dSEps>dT1)
                {dErr0=0.; dZ0=dSumZ;
                 dT0=dT1/(1.-dErr+dSEps);}
        }
        if ((dSEps>dErr0-dErr1) || (dDT<dT1-dT0)) {
            dTemp = (dT1+dT0) * 0.5;
            dSumZ = (dZ1+dZ0) * 0.5;
        } else {
            dTemp=(dT1*dErr0 - dT0*dErr1) / (dErr0-dErr1);
            dSumZ=(dZ1*dErr0 - dZ0*dErr1) / (dErr0-dErr1);
        }
        if (8. < (dZ=dUenc32/dTemp))
           {dT0 =dTemp =dUenc32/(dZ=8.); dErr0=0.;}
    }
    *pdTe = dTemp;
    if (iFl) return(dZ);
    *pdTd = dUd / (dnc * 1.5 * (dRd=dndc[8]));
    *pdTc = dUc / (dnc * 1.5 * (1. - *dndc));

/*************************************************************
    Calculate sums of densities * Coulomb Logarithms
    for e-d, e-c[1-6], d-c[1-6]
*************************************************************/
  dlnLB=dlLB-0.5*log(dTemp)+(dlnLA=0.5*log(dTe3/dnc/dRd));
    dlnLA += dlLA;
    *pdZLed = dRd *
      ((dlLL<(dLnLamb=((dTemp<dlLTc)?dlnLA:dlnLB))) ?
                        dLnLamb:dlLL);
    dnT    *= dnc * (dnT =
                (dMd + dMc) / (dMd * *pdTc + dMc * *pdTd));
```

```
    dZTd    = dRd / *pdTd;
    for (*pdZLdc=*pdZLec=0.,pdReg1=dndc+(i=7)-1; --i;
                                                pdReg1--)
        if (*pdReg1 > 1e-12) {
            dLnLamb  = (dTemp < i*i*dlLTc) ?
                       dlnLA - dlni[i] : dlnLB;
            *pdZLec +=  *pdReg1 * ((dLnLamb > dlLL) ?
                                   dLnLamb : dlLL);
            dLnLamb = dnT * (dZTd + *pdReg1/ *pdTc);
            dLnLamb = (1e-35 > dLnLamb) ? 1. :
                                dlLA - 0.5 * log(dLnLamb);
            *pdZLdc += *pdReg1 * ((dLnLamb > dlLL) ?
                                  dLnLamb : dlLL);
        }

/*************************************************************
    Calculate photon energy for optical thickness of r =1.
    Calculate optical thickness over one radius, first
    bremsstrahlung, then Free-Bound in order of ascending
    lower photon cutoff energies.
*************************************************************/
    dAlpR = (dSumZ-1.) * dZ * dGBrem *
            (dAlpr = dAlph * dR *
                 (dBFBScl = dZ*dnc*dnc/sqrt(dTemp)));
    for (dhw=0., pdReg1=dFBhw, pdReg2=dFBScl, piReg=iFB,
                                          i=14; i; i--) {
        dhw = (dAlpR > dTe3 * 1.4) ? pow(dAlpR, 1./3.) :

dTemp*dAlpR/(dTe3-dAlpR/6.)*(sqrt((1./48.)+dTe3/dAlpR)
                                -0.25);
```

```
        if (dhw < (dCLZ=*(pdReg1++)-
                        dConL[(6<(j=*(piReg++))) ?0: j-1]))
            break;
        if (0.<dCLZ && 1e-20<dndc[j])
            dAlpR += dAlpr *dndc[j] * *(pdReg2++)
                                    *exp(dCLZ / dTemp);
    }

/*************************************************************
    Calculate the radiation cooling from bremsstrahlung
    and F-B above this hw.
*************************************************************/
    *pdRadCol = (dCh1 = (dSumZ-1.)*dZ*dGBrem*dTemp) /
                            exp(dhwT=dhw/dTemp);
    for (pdReg1=dFBhw, pdReg2=dFBScl, piReg=iFB,
           i=iMax=14-i; i--; piReg++, pdReg1++, pdReg2++)
        if (0. < (dCLZ = *pdReg1 - dConL[(6 < (j=*piReg))
                                    ?0: j-1])) {
            dCh1 += (dT0 = dndc[j] * *pdReg2 / *pdReg1 *
                                dCLZ * exp(dCLZ/dTemp));
            *pdRadCol += dT0 / exp(dhwT);
        }
    *pdRadCol *= (dBFBScl *= dBrem/dQe);

/*************************************************************
    Add rad cooling from blackbody up to this hw energy.
*************************************************************/
    *pdRadCol += dBlkB * dTe3* dTemp / dR *
              ( (dAlpR > dTe3 * 1.4)
                  ? (dPi415 - (6. +dhwT*(6. +dhwT*
                        (3. +dhwT))) / exp(dhwT))
```

```
                    : (8.*log(1.+dhwT/2.)
                       +dhwT*(dhwT-4.)));

/*************************************************************
    Clipp tops of remaining Free-Bound lines.
*************************************************************/
    for (i=14-iMax; i--; piReg++, pdReg1++, pdReg2++)
        if(0.<(dCLZ = *pdReg1 -dConL[(6 < (j=*piReg)) ?0:
                                          j-1])) {
            dAlpR += dAlpr * dndc[j] * *pdReg2
                                     *exp(dCLZ / dTemp);
            dhw = (dAlpR > dTe3 * 1.4) ?
                          pow(dAlpR, 1./3.) : dTemp *

dAlpR/(dTe3-dAlpR/6.)*(sqrt((1./48.)+dTe3/dAlpR)-0.25);
            dCh1 += exp(dCLZ/dTemp) *

(dT0=dndc[j]* *pdReg2 / *pdReg1*dCLZ);
            *pdRadCol += dBFBScl * dT0 * ((dhw>dCLZ) ?

exp((dCLZ-dhw)/dTemp)*(1.+(dhw-dCLZ)/dTemp) :
                                    (j < 6)    ? 1e2 : 1.);
        }

/*************************************************************
    Finish computing the x-ray monochromator signals.
*************************************************************/
    dCh1 *= 2e-7 * dR*dR / dTemp * dBFBScl*dQe;
    if (dR > 0.016) dCh1 *= 1. + 2./dPi *

(0.016/dR/dR*sqrt(dR*dR-2.5e-4) - acos(0.016/dR));
```

```
dCh3 = 2.100 / exp(1000/dTemp) * dCh1 * 0.5;
dCh2 = 0.400 / exp( 750/dTemp) * dCh1 * 0.3;
dCh1 = 0.025 / exp( 500/dTemp) * dCh1;
return (dZ);}
```

TABLE VII. Neutron yield (in 10^9) for five shots as measured by four detectors. Errors are based only on counting statistics.

Shot	Arsenic	Rhodium	Silver	Indium
1	0.3±0.02	0.15±0.12	0.57±0.02	X
2	1.6	2.30±0.2	4.0	8.5±0.4
3	2.8	2.8	5.0	10.6±0.4
4	1.8	2.4	4.0	6.2±0.4
5	2.2	2.6	5.4	7.5±0.8

D. Neutron Detectors

For five D_2 shots there was also a fourth measurement of the neutrons based on indium activation, which is the most accurate of the four but requires too much time to be done on every shot.* Taking the indium results as the standard, the data from these five shots show that the silver counter was the most accurate of the three counters used for the majority of shots, as shown in TABLE VI, TABLE VII. The silver and, more so, the rhodium counters probably underestimate the neutron yield because they are moderated detectors. The silver counter seems to fall short by almost a factor of two from the indium. The silver counter and the indium activation sample detectors are described below. The neutron counts presented in Section 4.5 are from the silver activation counter.

D.1. Silver Activation Counter

The silver activation counter is the standard type developed by Lanter and Bannerman,[59] which consists of four Geiger-Müller (G-M) tubes, each wrapped with 10-mil silver foil and inserted into holes in a 12" × 12" × 6" block of polyethylene.

---

* The neutron diagnostics were fielded and calibrated by Dr. Robert Chrien.

Fast neutrons are moderated to thermal energy by the polyethylene and cause activation of the silver. Silver consists of two isotopes in nature, ^{107}Ag (51.3%, 30b) and ^{109}Ag (48.7%, 110b). The activation products ^{108}Ag (138 s half life, 1.49 MeV β) and ^{110}Ag (24.2 s half-life, 40% 2.82 MeV and 60% 2.24 MeV β) decay by beta emission. The G-M pulses are capacitively coupled to a cable leading to the screen room. This signal is amplified by an Ortec 773 timer/counter that is gated by another Ortec 773 for 60 s starting 0.1 s after a shot. The background is about 159 cpm. The counter is installed on the diagnostic platform at a distance of 1.7 m from the plasma at an elevation of 30°.

D.2. Silver Activation Counter Calibration

The silver activation counter was calibrated *in situ* with a ^{252}Cf neutron source of strength $S = 3.6\times10^{6}$ neut/s placed inside the HDZP-II vacuum chamber at the position normally occupied by the plasma. After the counts reached steady state, a count was accumulated for 200 minutes. This produced 2044±4 cpm for the silver activation counter.

The silver activation counter is located close enough to the neutron source that rapidly removing the source reduces the neutron flux to a negligible level in a time short compared to the decay time of the detector. The silver activation counter was then calibrated based on the number of counts recorded after the source had been rapidly removed from the detector, when it had reached a steady-state activation. This eliminates all contribution from capture gamma rays. The calibration derived from this method is $(2.6\pm0.1)\times10^{5}$ neutrons per count, which is consistent with the original calibration.

D.3. Indium Activation Diagnostic

The indium activation technique is widely used for neutron calibration, as described by Zankl[61]. The neutrons from D-D reactions inelastically scatter from ^{115}In (95.7%, 326 mb), exciting a metastable state (0.336 MeV) which decays through gamma emission with a 1.6×10^4 s half-life. The sample was removed after one or two shots and the gamma rays were recorded with a germanium detector. A 0.65-cm-thick, 5-cm-diameter, 100-g disk of indium was used.

The neutron fluence Γ in neut/m^2 produces a specific activity

$$A_0 = \Gamma \lambda \sigma N_I \tag{D.1}$$

at time t_0 of the neutron pulse, where $\lambda \approx 4.29\times10^{-5}$ s^{-1} is the decay constant for the nuclide produced, σ is the activation cross section, and $N_1 \approx 5.0\times10^{23}$ is the number of ^{115}In nuclei. The specific activity was computed from the initial count rate R_0 as

$$A_0 = R_0 / \epsilon \alpha \beta \quad , \tag{D.2}$$

where $\epsilon = 0.069$ is the detector efficiency at 0.336 MeV for a 5 -cm disk, $\alpha = 0.459$ is the fraction of gamma photons per disintegration, and $\beta = 0.69$ is the self-absorption factor. The detector efficiency was measured through activation of a thin indium foil by a ^{252}Cf neutron source. The self-absorption factor was determined by comparison of the counts from the 100-g sample with a thin sample exposed to the same neutron flux. The initial count rate is related to the number of counts integrated from time t_1 to t_2 as

$$R_0 = \frac{C \lambda}{e^{-\lambda(t_1 - t_0)} \left[1 - e^{-\lambda(t_2 - t_1)}\right]} \quad . \tag{D.3}$$

The neutron fluence is then

$$\Gamma = \frac{C}{\sigma N_I \epsilon \alpha \beta} \frac{e^{\lambda(t_1 - t_0)}}{\left[1 - e^{-\lambda(t_2 - t_1)}\right]} \quad . \tag{D.4}$$

E. Free Expansion Model

Another way to make the plasma radius expand is to remove the magnetic confinement force in the simulation. This lack of confinement could result from the MHD instabilities growing as magneto-sonic waves causing the column to expand at nearly the ion thermal velocity. This model is identical to the stable model with the magnetic confinement force term in the radial acceleration set to zero. This model is included for comparison with the data as an appendix because it does not seem to have a realistic physical justification.

E.1. Comparison of Free Expansion Model with Circular-Schlieren Results

The plots in Fig. E.1, Fig. E.2, Fig. E.3, Fig. E.4, Fig. E.5, and Fig. E.6 compare the results of the 0-D simulation with free expansion with the measured rms radii. This fast radial expansion of the radii at later times was measured and predicted by this model; this is clearly different from the collapse predicted by the stable model and the leveling off of the enhanced Spitzer model. The simulated radii of this no-confinement model tends to over-shoot the measured radii a little at earlier times but fits the radius data well at later times.

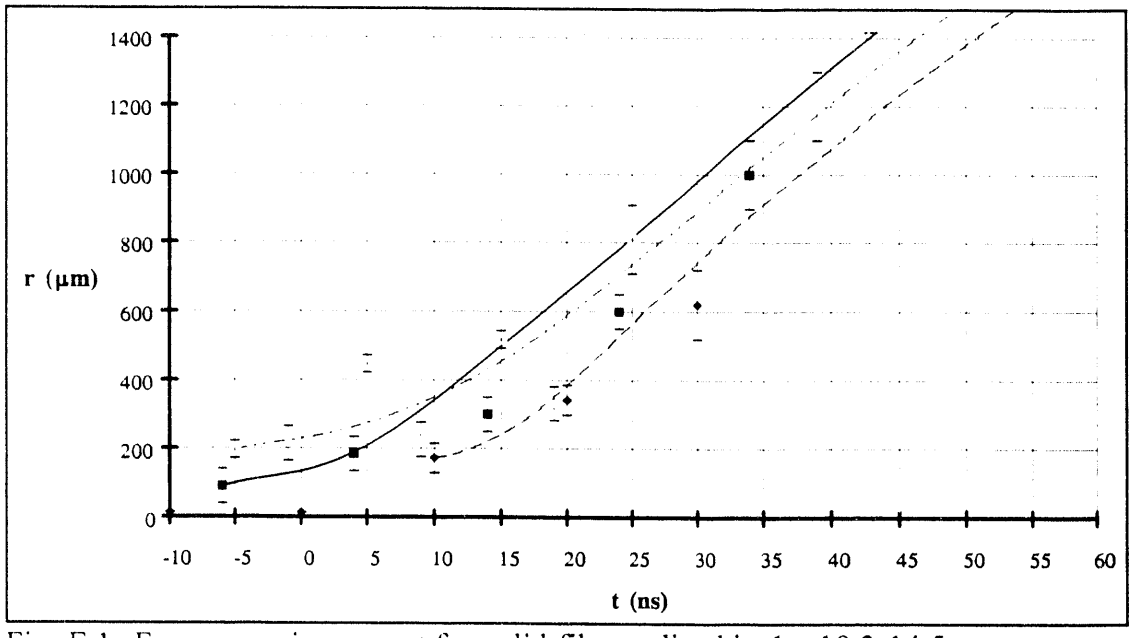

Fig. E.1 Free expansion r vs. t for solid-fiber-radius bin 1: 10.3-14.5 μm.

Legend: (■) shot 362, (✳) shot 379, (O) shot 373, and (✳) shot 377.

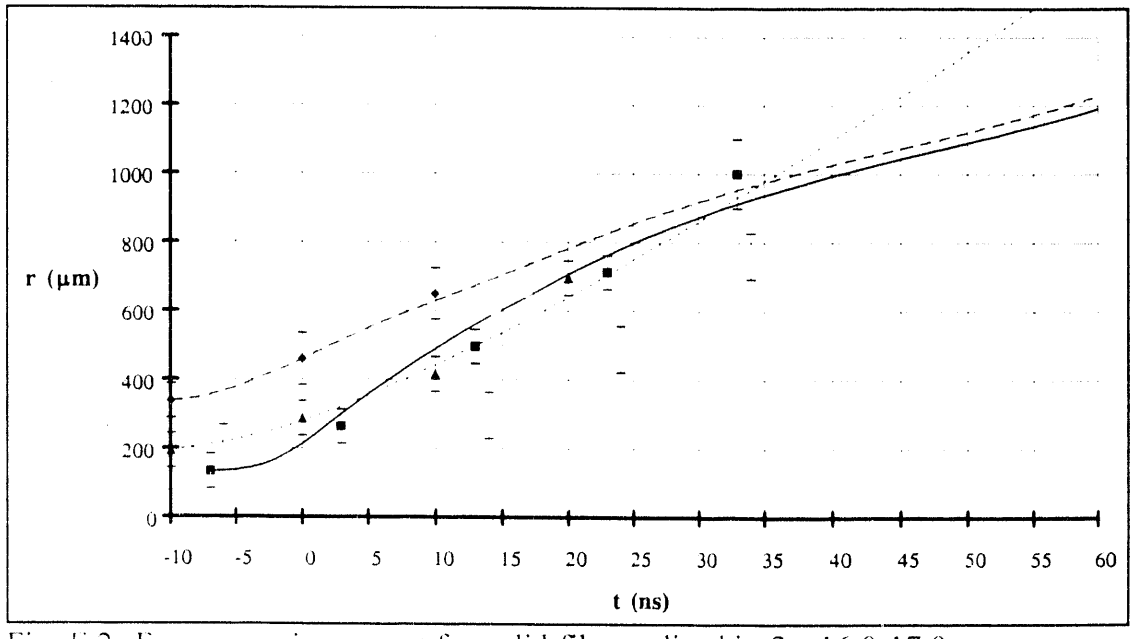

Fig. E.2 Free expansion r vs. t for solid-fiber-radius bin 2: 16.0-17.0 μm.

Legend: (■) shot 367, (✳) shot 370, (✳) shot 374, and (O) shot 376.

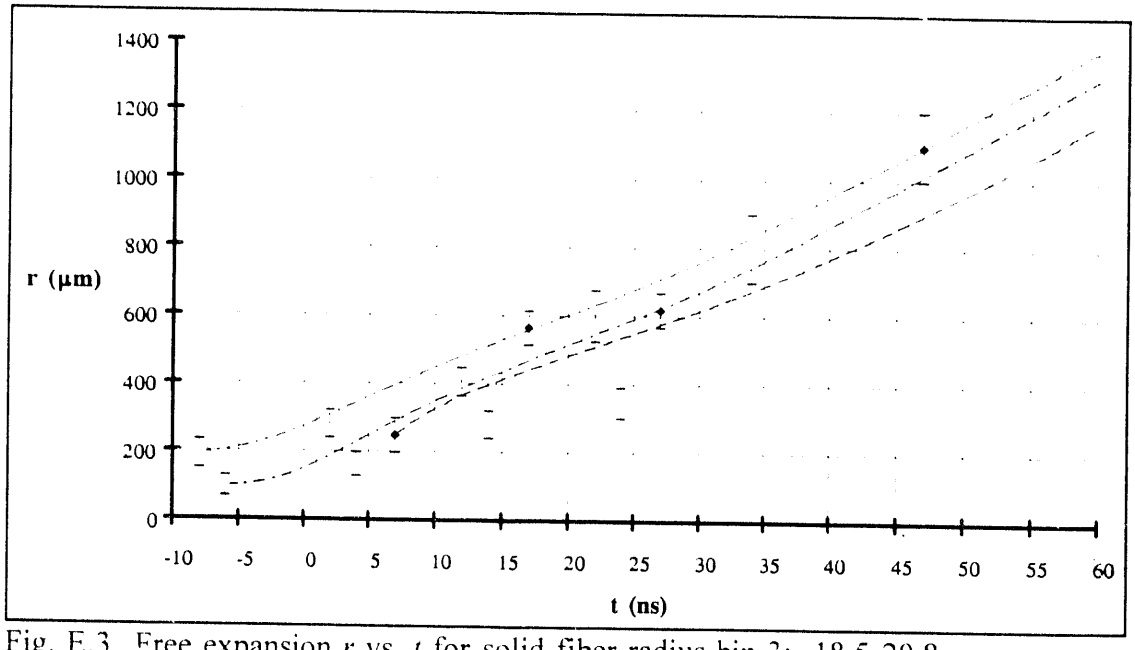

Fig. E.3 Free expansion r vs. t for solid-fiber-radius bin 3: 18.5-20.8 μm.

Legend: (◆) shot 408, (O) shot 353, and (×) shot 409.

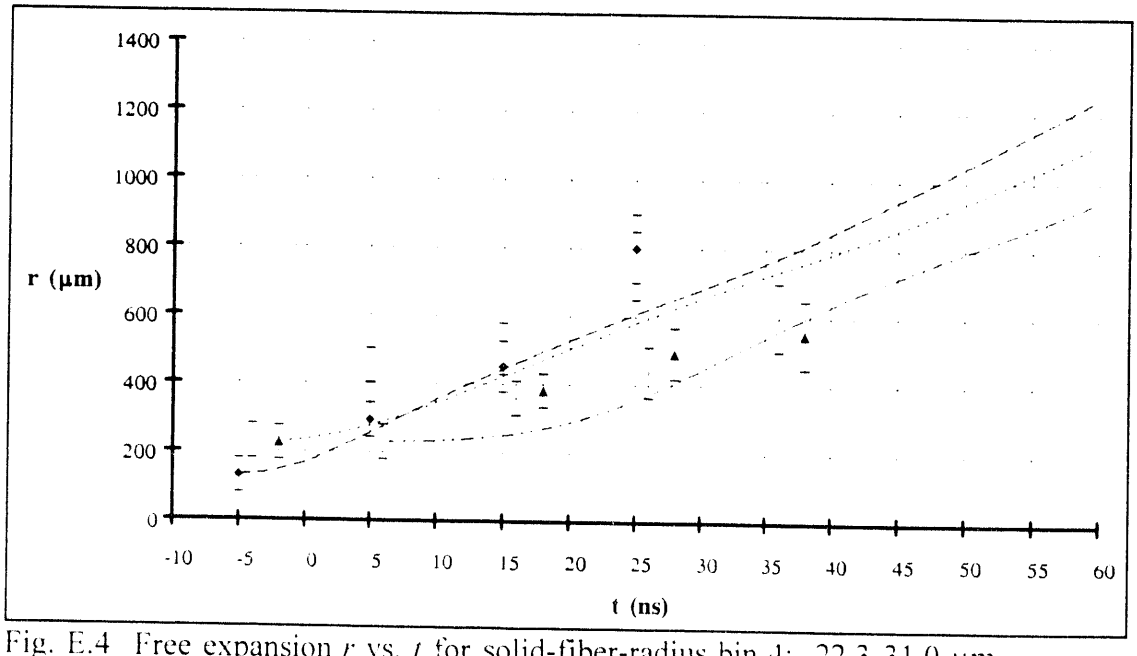

Fig. E.4 Free expansion r vs. t for solid-fiber-radius bin 4: 22.3-31.0 μm.

Legend: (◆) shot 403, (▲) shot 411, (O) shot 386, and (×) shot 385.

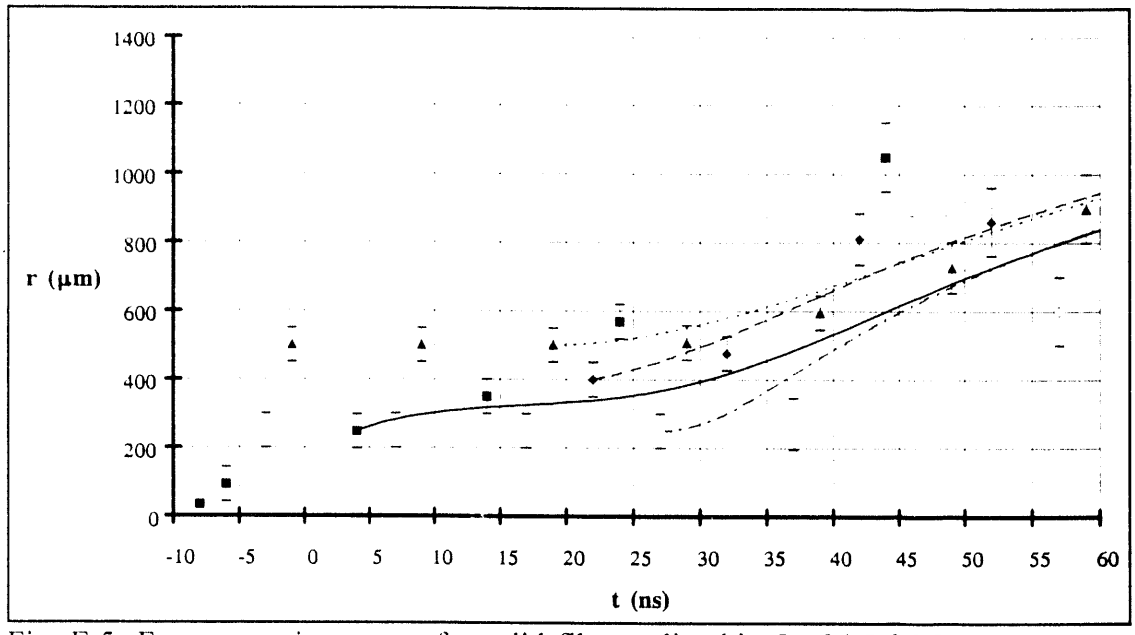

Fig. E.5 Free expansion r vs. t for solid-fiber-radius bin 5: 34.5-36.5 μm.

Legend: (■) shot 415, (◆) shot 372, (▲) shot 383, and (O) shot 405.

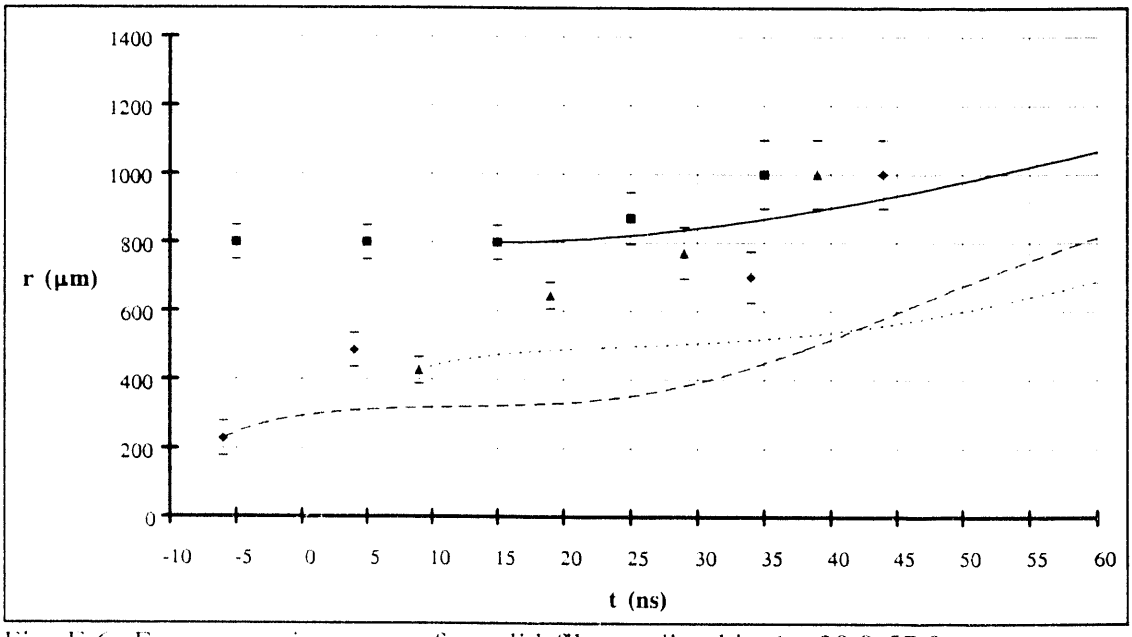

Fig. E.6 Free expansion r vs. t for solid-fiber-radius bin 6: 39.8-57.0 μm.

Legend: (■) shot 382, (◆) shot 423, and (▲) shot 416.

E.2. Comparison of Free Expansion Model with T_e Data

The plots in Fig. E.7 show the plasma electron temperature predicted by the free expansion model. The predicted temperatures remain in the range of measured electron temperature data over the full range of solid-fiber radii.

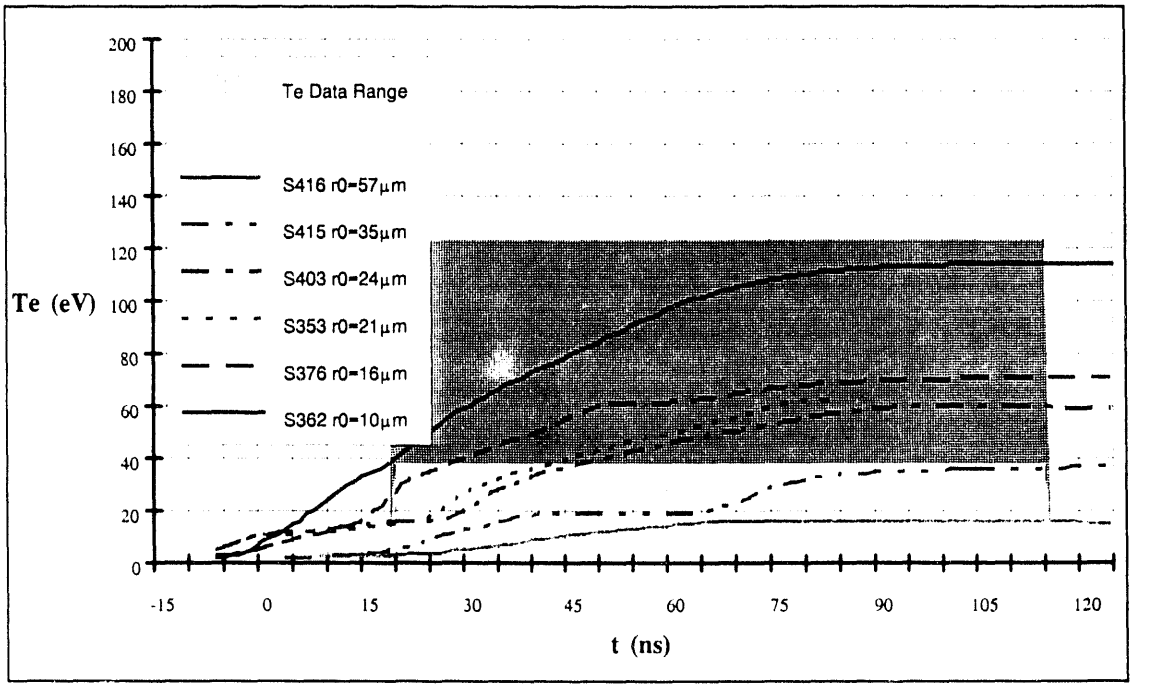

Fig. E.7 Free expansion T_e vs. t plots for r_0 = 10-57 μm.

The data range appears much larger in this plot due to the change in vertical scale relative to similar plots for the stable and enhanced Spitzer models.

E.3. Comparison of Free Expansion Model with T_i Data

The plots in Fig. E.8 show the ion temperatures predicted by the free expansion model. These temperatures are almost two orders of magnitude below that required for Bennett equilibrium, as shown in Fig. 4.22, but Bennett equilibrium has little meaning in the absence on magnetic confinement.

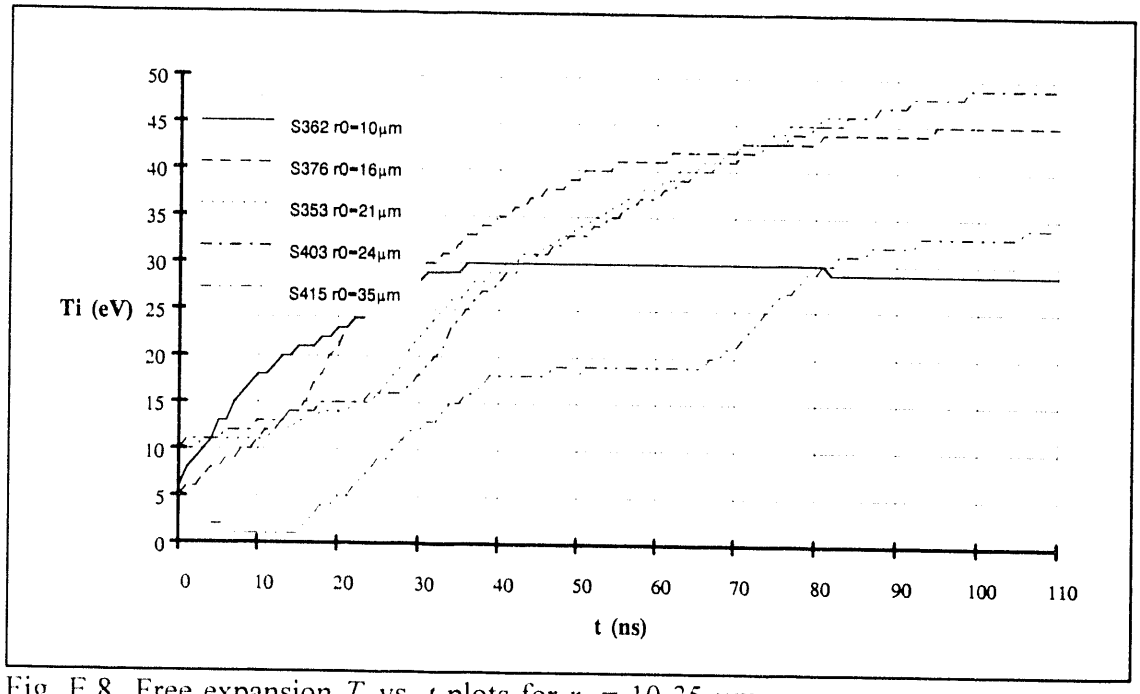

Fig. E.8 Free expansion T_i vs. t plots for r_0 = 10-35 μm.

E.4. Comparison of Free Expansion Model with X-Ray Data

The plots in Fig. E.9 show the 500 eV spectrometer signals predicted by the simulation. The predicted signals have magnitudes very similar to that of the data presented in Chapter 4. The slow fall off of the signal compaired to the data suggests that the radial expansion predicted by this model is slower than of the real plasma.

E.5. Comparison of Free Expansion Model with Neutron Data

The thermonuclear neutron yields predicted by the free expansion model were always much less than 1, on the order of 10^{-6} neutrons per shot. This is due primarily to the low ion temperatures predicted by this model. It may be argued that the neutrons could have been produced by some directed kinetic energy process that did not require a high ion temperature.

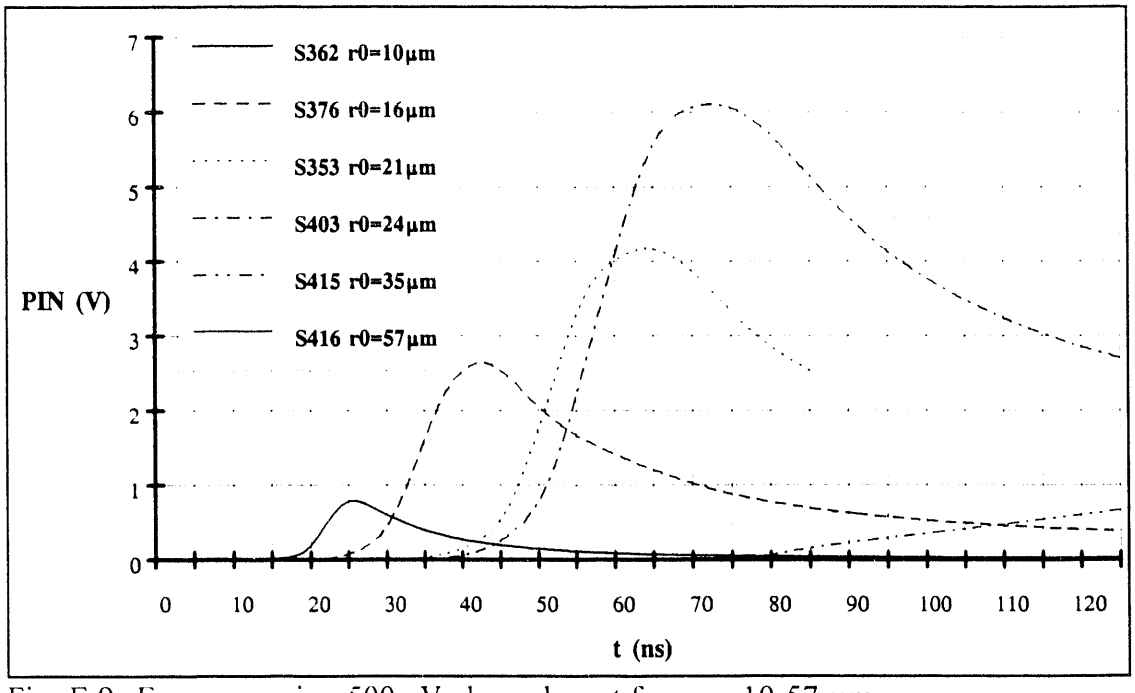

Fig. E.9 Free expansion 500-eV channel vs. t for r_0 = 10-57 μm.

REFERENCES

1. F. F. Chen, Introduction to Plasma Physics (Plenum Press, New York, 1974), p. 281.

2. J. A. Edminister, Schaum's Outline of Theory and Problems of Electromagnetics (McGraw-Hill Book Co., 1979), p. 140.

3. W. H. Bennett, "Magnetically Self-Focussing Streams," Phys. Rev. **45**, 890-897 (1934).

4. J. D. Jackson, Classical Electrodynamics, 2nd ed. (Wiley, New York, 1962), p. 171.

5. M. N. Rosenbluth, "Infinite Conductivity Theory of the Pinch," Los Alamos Scientific Laboratory Report LA-1850 (1954).

6. D. C. Hagerman and J. W. Mather, "Neutron Production in a High-Power Pinch Apparatus," Nature **181**, 226-228 (1958).

7. S. C. Curran, K. W. Allan, H. A. B. Bodin, R. A. Fitch, N. J. Peacock, and J. A. Reynolds, "Studies of High-Current Gas Discharges at High Rates of Build Up," in Proc. Second U. N. International Conf. on the Peaceful Uses of Atomic Energy, **31**, (1958), pp. 365-373.

8. J. N. DiMarco and L. C. Burkhardt, "Z-Pinch Driven by Magnetic Energy Storage," in Controlled Fusion and Plasma Physics (Proc. 4th Europ. Conf. Rome), (1970), p. 53.

9. O. A. Anderson, W. R. Baker, S. A. Colgate, H. P. Furth, J. Ise, Jr, R. V. Pyle, and R. E. Wright, "Neutron Production in Linear Deuterium," Phys. Rev. **109** (2), 612-13 (1958).

10. S. W. Cousins and A. A. Ware, "Pinch Effect Oscillations in a High Current Toroidal Ring Discharge," Proc. Phys. Soc. (London) **64**, 159-166 (1951).

11. S. A. Colgate, J. P. Ferguson, and H. P. Furth, "A Partly Stabilized Dynamic Pinch," in Proc. Second U. N. International Conf. on the Peaceful Uses of Atomic Energy (Controlled Fusion Devices), **32**, (1958), pp. 140-144.

12. L. C. Burkhardt and R. H. Lovberg, "Field Configurations and Stability in a Linear Discharge," in Proc. Second U. N. International Conf. on the Peaceful Uses of Atomic Energy (Controlled Fusion Devices), **32**, (1958), pp. 29-33.

13. H. Alfvén and E. Smars, Nature **188**, 801 (1960).

14. E. A. Smars, Arkiv För Fysik **Band 29**, 97 (1964).

15. J. S. Shlachter, The Behavior of a Plasma in a High Density Gas Embedded Z-Pinch Configuration, Ph. D. thesis, University of California, San Diego, (Los Alamos National Laboratory Report LA-9333-T) 1982.

16. R. S. Pease, "Equilibrium Characteristics of a Gas Discharge Cooled by Bremsstrahlung Radiation," Proc. Phys. Soc. (London) **70**, 11-23 (1957).

17. S. J. Braginskii, "The Behavior of a Completely Ionized Plasma in a Strong Magnetic Field," Sov. Phys. JETP **6** (3), 494-501 (1958).

18. S. Glasstone and R. H. Lovberg, Controlled Thermonuclear Reactions (Van Nostrand Publishing, 1960), p. 31.

19. L. Spitzer Jr., Physics of Fully Ionized Gases, 2nd ed. (Interscience Publishers Wiley, New York, 1967), p. 139.

20. L. Spitzer Jr., "Equations of Motion for an Ideal Plasma," Astrophys. J. **116**, 299-316 (1952).

21. T. W. Johnston and J. M. Dawson, "Correct Values for High-Frequency Power Absorption by Inverse Bremsstrahlung in Plasmas," Phys. Fluids **16** (5), 722 (1973).

22. M. G. Haines, "The Joule Heating of a Stable Pinched Plasma," Proc. Phys. Soc. (London), **76**, 250-260 (1960).

23. J. E. Hammel, "An Ohmically Heated High-Density Z Pinch," Los Alamos Scientific Laboratory Report LA-6203-MS (1976).

24. M. N. Rosenbluth, "Stability of the Pinch," Los Alamos Scientific Laboratory Report LA-2030 (1959).

25. R. J. Tayler, "The Stability of a Constricted Gas Discharge," in Proc. Second U. N. International Conf. on the Peaceful Uses of Atomic Energy, **31**, (1958), p. 160-170.

26. W. A. Newcomb, Ann. Phys. **10**, 232 (1960).

27. B. B. Kadomtsev, in Reviews of Plasma Physics, edited by M. A. Leontovich (Consultants Bureau, New York, 1966), **2**, pp. 153-199.

28. N. A. Krall and A. W. Trivelpiece, Principles of Plasma Physics (San Francisco Press, Inc., California, 1986), p.261.

29. K. Wark, Thermodynamics, 3rd ed. (McGraw-Hill, New York, 1977), pp. 84, 415.

30. K. Miyamoto, Plasma Physics for Nuclear Fusion, Revised ed., (MIT Press, Cambridge, MA, 1987), p. 150.

31. B. B. Kadomtsev, "Hydromagnetic Stability of a Plasma," Rev. of Plasma Physics, **II**, 153-199 (1966).

32. J. D. Jackson, Classical Electrodynamics, 2nd ed. (Wiley, New York, 1962), p. 298.

33. R. McWhirter, in Plasma Diagnostic Techniques, edited by Huddelstone and Leonard (Academic Press, New York, 1965).

34. R. L. Kelly, "Atomic and Ionic Spectrum Lines below 2000 Angstroms: Hydrogen through Krypton," Journal of Physical and Reference Data, **16**, 1987.

35. H. R. Griem, Plasma Spectroscopy (McGraw-Hill Book Co., New York, 1964), p. 137.

36. Y. B. Zel'dovich and Y. P. Raizer, Physics of Shock Waves and High-Temperature Hydrodynamic Phenomena, **1** (Academic Press, New York, 1966), p. 194.

37. J. C. Stewart and K. D. Pyatt, Jr. Astrophys. J. **144**, 1203 (1966).

38. A. Sommerfeld, Atomic Structure and Spectral Lines (Methuen & co. ltd., London, 1934)

39. W. J. Karzas and R. Latter, "Electron Radiative Transitions in a Coulomb Field," Astrophys. J. Suppl. Ser. **6** (55), 167-212 (1961).

40. H. Kramers, Philos. Mag. **46**, 836, (1923).

41. I. H. Hutchinson, Principals of Plasma Diagnostics (Cambridge University Press, Cambridge, 1987), p. 173.

42. S. von Goeler, "Diagnostics for Fusion Experiments," in Proceedings of the 1982 Int. School of Plasma Physics at Varenna, edited by P. Stott et al. (Brussels: Commission of E.E.C.).

43. G. Bekefi, Radiation Processes in Plasmas (Wiley, New York, 1966), p. 584.

44. H. R. Griem, Plasma Spectroscopy (McGraw-Hill Book Co., New York, 1964), p. 197.

45. R. W. Lee, "Plasma Line Shapes for Selected Transitions in Hydrogen-, Helium-, and Lithium-Like Ions," J. Quant. Spectrosc. Radiat. Transfer, **40** (5), 561-568, (1988).

46. W. H. Press, S. A. Teukolsky, W. T. Vetterling, B. P. Flannery, Numerical Recipes in C, 2nd ed. (Cambridge Press, New York, 1992), pp. 724-732.

47. H. Akima, "A New Method of Interpolation and Smooth Curve Fitting Based on Local Procedures," Journal of the A.C.M. **17** (4), 589-602 (1970).

48. R. H. Lovberg, R. A. Riley, Jr., and J. S. Shlachter, "Instability heating of the HDZP," in Proceedings of the Third International Conference on Dense Z-Pinches (London, United Kingdom, April, 1993).

49. M. N. Rosenbluth (private conversation).

50. F. F. Chen, Introduction to Plasma Physics (Plenum Press, New York, 1974), p. 322.

51. W. D. Bachalo and M.C. Houser, "Evaluation and Application of a New Interferometry Technique for Compressible Flow Research," NASA Contractor Report 1777467 (October, 1988).

52. H. R. Griem, Plasma Spectroscopy (McGraw-Hill, New York, 1964), p. 12.

53. H. R. Griem, Plasma Spectroscopy (McGraw-Hill, New York, 1964), pp. 176-178.

54. F. C. Jahoda and G. A. Sawyer, in Methods of Experiment Physics, edited by R. H. Lovberg and H. R. Griem (Academic Press, New York, 1971), Vol 9, Part B, pp. 20-27.

55. I. H. Hutchinson, Principals of Plasma Diagnostics (Cambridge University Press, Cambridge, 1987), pp. 112-115.

56. L. D. Landau, E. M. Lifshitz, and L. P. Pitaevskii, Electrodynamics of Continuous Media, 2nd ed. (Pergamon Press, New York, 1984), Vol. 8, p. 291.

57. B. L. Henke, J. Y. Uejio, H. T. Yamada, and R. E. Tackaberry, "Characterization of Multilayer X-Ray Analyzers: Models and Measurements," Optical Engineering **25**, No. 8, 937 (August, 1986).

58. B. L. Henke, P. Lee, T. J. Tanka, R. L. Shimabukuro, and B. K. Fujikawa, "Low-Energy X-Ray Interaction Coefficients: Photoabsorption, Scattering, and Reflection," Atomic Data and Nuclear Data Tables **27**, No. 1 (January, 1982).

59. R. J. Lanter and D. E. Banner, "The Silver Counter: A Detector for Bursts of Neutrons," LA-3498-MS and R.S.I. **39**, 1588 (1968).

60. W. Kies, G. Decker, M. Mäzig, C. van Calker, J. Westheide, G. Ziethen, H. Bachmann, K. Baumung, H. Bluhm, D. Rusch, W. Ratajczak, O. Stoltz, and J. M. Bayley, "Terawatt Fiber-Pinch Experiments," in J. Appl. Phys. **70** (12), (December, 1991) 7261-72

61. G. Zankl, J. D. Strachan, R. Lewis, W. Pettus, and J. Schmotzer, "Neutron Flux Measurements Around the Princeton Large Tokamak," Nuclear Instruments and Methods **185**, 321-329 (1981).

•U.S. GOVERNMENT PRINTING OFFICE 1994-0-573-024/87064

END

DATE
FILMED
3/14/94